How do rocks move in rivers?

The grain-scale mechanisms that control the onset of motion

A Dissertation

Presented in Partial Fulfillment of the Requirements for the

Degree of Doctor of Philosophy

with a

Major in Water Resources, Engineering and Sciences

in the

College of Graduate Studies

University of Idaho

by

Heidi Elizabeth Joyce Smith

Major Professor: Elowyn M. Yager, Ph. D.

Committee Members: Ralph Budwig, Ph.D., Alex Fremier, Ph.D. and Jens Turowski, Ph.D.

Department Administrator: Matthew J. Morra, Ph.D.

May 2019

Authorization to Submit Dissertation

This dissertation of Heidi Elizabeth Joyce Smith, submitted for the degree of Doctor of Philosophy with a Major in Water Resources and titled "How do rocks move in rivers? The grain-scale mechanisms that control the onset of motion" has been reviewed in final form. Permission, as indicated by the signatures and dates below, is now granted to submit final copies to the College of Graduate Studies for approval.

Major Professor: _____ Date: _____
Elowyn M. Yager Ph.D.

Committee Members: _____ Date: _____
Ralph Budwig, Ph.D.

_____ Date: _____
Alex Fremier Ph.D.

_____ Date: _____
Jens Turowski, Ph.D.

Department
Administrator: _____ Date: _____
Matthew J. Morra, Ph.D.

Abstract

The onset of sediment motion in rivers is important for predictions of river stability, and for the design of hydraulic structures and river restoration projects. Considerable uncertainties in calculations and measurements of the onset of motion exist. Most calculations of the onset of sediment motion do not explicitly include turbulence effects but recent studies have suggested that impulse, the product of the duration and magnitude of drag forces that are greater than a critical value, is likely to cause grain movement. We explore if sediment motion can be systematically explained with instantaneous drag forces and impulses. In a series of 26 flume experiments, we measured instantaneous pressures and velocities on a mobile test grain for which the precise timing of motion was known. We used these measurements to calculate drag forces and impulses in a range of possible ways. Impulse and drag forces were concluded to cause particle motion in a given experiment if their highest measured values occurred during grain motion rather than during any time when the test grain was stable. Use of the measured upstream velocity profile instead of a single point velocity provided calculated drag forces and impulses that better corresponded to the onset of particle motion. The correlations of drag forces and impulses with particle motion were also greatly dependent on the selected drag coefficient, implying that field applications of impulse may need to consider the effects of grain shape and orientation instead of simply assuming spherical particles. Out of all the various drag force and impulse parameters we tested, an impulse that incorporated a decreasing resisting force during particle rotation out of its pocket explained the greatest percentage (88%) of observed grain motions. The start of grain rotation could not be explained by impulse for 12% and 17% of particle motions when we used velocity and pressure data, respectively, to calculate impulse. This suggests that either the onset of particle motion may be sometimes driven by another flow parameter, or that typically measured velocity and pressure data used to calculate impulse may not adequately capture the spatial variation in flow structure around a grain. A temporally variable drag coefficient could in theory indirectly account for some of these spatial and temporal variations in grain-scale flow. Use of a temporally variable drag coefficient did not improve the performance of impulse in explaining particle motion, implying that a more complex flow parameter that accounts for spatial flow patterns may sometimes be needed. Understanding how sediment fluxes in rivers are related to applied shear stresses is imperative for improving restoration efforts or minimizing loss of property though urbanized reaches. Bedload equations often predict inaccurate sediment fluxes partly because of uncertainty in the shear stresses that cause the start of sediment motion (critical Shields stresses). Although often assumed to be a constant value, the critical Shields stress can increase with greater channel slope, which has been potentially explained by a wide variety of processes. To fully understand this phenomenon, we conducted a series of flume experiments through a range of slopes

in which we measured the critical Shields stress and near-bed flow velocity at the onset of motion of a mobile test grain with a fixed pocket geometry. We used two bed configurations, one with and one without large immobile grains, to explore the effects of large boulders on critical Shields stresses. Contrary to previous studies that have shown a general increase in critical Shields stress with greater channel slope or relative roughness, the critical Shields stress in our experiments only increased when (1) boulders were added, and (2) the boulder tops began to emerge from the flow. Otherwise, critical Shield stresses remained roughly constant with greater slope or relative roughness. We tested many of the previously hypothesized reasons for critical Shields stress increases with slope and found that none could fully explain our experimental observations. We hypothesize that in our data and in natural rives, many of the observed changes in critical Shields stress are caused by decreases in boulder submergence and increases in boulder concentration with higher slope. These changes in boulder properties drive previously unaccounted for complex variations in the flow structure that affect the onset of motion of finer, more mobile particles. The critical Shields stress can also vary between grain sizes, and can be predicted with hiding functions, which describe how grain mobility is affected by the underlying grain size distribution, such that the ratio of the grain size (D_i) to the median bed grain size (D_{50}) determines the critical Shields stress for the ith grain size. A patch is defined as an area of the bed that is occupied by grains of distinct size distribution, where its boundary is defined by a clear change in grain size distribution indicating the neighboring patch. The relative mobility of grains throughout a reach have been studied, but the effect of local variation of grain sizes between patches on grain relative mobility is largely unknown. We explore the effects of patch-scale grain size variability on the degree of sediment mobility by developing hiding functions for different patch types within the Erlenbach torrent (Brunni, Switzerland). To determine hiding functions for each patch type, we used: (i) the D_{84} of the mobile tracer grain size distribution from each patch type for 10 storm events (discharges of 0.17 to 2.1 cms), by monitoring the movement of painted and RFID tagged tracer grains from the most prevalent patch types, and (ii) the median local shear stress on each patch type for each discharge modeled using the quasi-3D FaSTMECH model. We also measured in-situ protrusions (vertical distance a grain extends relative to near-by grains upstream) and calculated friction angles (the angle a grain must rotate through for mobilization) for all grain sizes present on each patch type, which are local grain-scale parameters that can lead to the size-selective entrainment that hiding functions often describe. We observed protrusion to be greater for larger grains, but for the same grain size (D_i) protrusion was higher on finer patches. However, all patches have about the same relation between relative grain size (D_i/D_{50}) and dimensionless values of protrusion (protrusion/grain height) and friction angle.

Acknowledgements

I have been fortunate to work with many wonderful people during my graduate work. I would like to first thank my major professor Elowyn Yager, who was endlessly supportive through my time as a doctoral student. She encouraged my abilities as a scientist, and guided me to critique, write and present science, while allowing me to have the flexibility to also be a mother of two children. I am appreciative of the guidance from my committee members: Ralph Budwig, Alex Fremier and Jens Turowski. My field seasons in Switzerland were made productive and very enjoyable by the researchers at the WSL in Zurich. Also, I thank the graduate students, faculty and staff at the Center for Eco-hydraulics for being a joy to explore science with.

Dedication

I have been supported and encouraged by many wonderful people in my life, who made it possible to continue working on my research when life logistics made completing my degree unlikely. I would like to say a grateful thank you to everyone. Jaya. Nitai, Tulsi, Onyx. Mama, Papa. Kelly, Aaron, Grace, Solomon and James. Peter and Carlotta. Gail, Claudia. Maha, Henry, Darshy, Asha, Priya and Takeshi. Maya, Jack. Lalita and Chris. Kelly, Lauren, John. Erin, Yuri. Sasha. Carrie, Rapha, Lea, Ian. Manu, Grit, Rosa, Rio. Susie. Nan, Mark. Dave and Lee. Josie. Rafi. Jules. Shane. Jay and Eilen. Fabienne, Ben. Mike, Jen. Jon, Gitte. Brian. Adam, Nicky. Mari. Adam. Dusty and Emily. Sean. Steve. Matthew, Miranda. Cecily. Laura. Mark and Luisa. Andree. Elisa. Lauren, Austin. Sonya, Luke. Faith. Vicken, Sarah. Frau Job. Tom and Vreni. Grandma Joyce, Grandpa Fred, Oma Luise and Opa Thomas. Silvia. Ross. Onkel Hans. Tante Aunie. The Schott's in Kitzbuhel. Shanti, Brhas.

Table of Contents

List of Tables

List of Figures

Chapter 1: Inspecting impulse as the parameter responsible for grain motion

Abstract

Most calculations of the onset of sediment motion in rivers do not explicitly include the effects of turbulence but recent studies have suggested that impulse, the product of the duration and magnitude of drag forces, is likely to cause grain movement. We explore if sediment motion can be systematically explained with instantaneous drag forces and impulses. In a series of 26 flume experiments, we measured instantaneous pressures and velocities on a mobile test grain for which the precise timing of its full rotation from its pocket was known. We used these measurements to calculate drag forces and impulses in a range of possible ways. Impulse and drag forces were concluded to cause particle motion in a given experiment if their highest measured values occurred during full grain motion rather than during any time when the test grain was stable. Use of the measured upstream velocity profile instead of a single point velocity provided calculated drag forces and impulses that better corresponded to the onset of particle motion. The correlations of drag forces and impulses with particle motion were also greatly dependent on the selected drag coefficient, implying that field applications of impulse may need to consider the effects of grain shape and orientation instead of simply assuming spherical particles. Out of all the various drag force and impulse parameters we tested, an impulse that incorporated a decreasing resisting force during particle rotation out of its pocket explained the greatest percentage (88%) of observed grain motions. The start of grain rotation could not be explained by impulse for 12% and 17% of particle motions when we used velocity and pressure data, respectively, to calculate impulse. This suggests that either the onset of particle motion may be sometimes driven by another flow parameter, or that typical velocity and pressure data that are used to calculate impulse may not adequately capture the spatial variation in flow structure around a grain. A temporally variable drag coefficient could in theory indirectly account for some of these spatial and temporal variations in grain-scale flow. Use of a temporally variable drag coefficient did not improve the performance of impulse in explaining particle motion, implying that a more complex flow parameter that accounts for spatial flow patterns may sometimes be needed.

Introduction

Accurate sediment flux predictions are important for management efforts such as river restoration, riverbank stabilization within urbanized floodplains, and reservoir design. Sediment transport can also influence the channel bed morphology and grain sizes that are the basis for habitat analyses for macroinvertebrate communities (Robinson et al., 2004) and salmonid species (Groot and Margolis, 2000, Kondolf, 2000). Additionally, knowledge of sediment transport processes informs flow reconstructions within paleochannels on earth (Church, 1978) and explorations of channel formation on other planets (e.g. Perron et al., 2006). Many sediment transport equations predict sediment fluxes as a nonlinear function of the difference between the reach-averaged applied and critical (at the onset of grain motion) shear stresses. Thus, small inaccuracies in the critical shear stress can result in orders of magnitude errors in calculated sediment transport rates (e.g. Gomez and Church, 1989).

The critical shear stress is often calculated or measured at the scale of a reach, but this simplifies the balance between driving and resisting forces acting on individual particles (Fenton and Abbot, 1977, Kirchner et al., 1990, Buffington et al., 1992, Schmeeckle et al., 2007, Dwivedi et al., 2010, Celik et al., 2010). Turbulence affects the temporal sequence of driving forces acting on a grain and may need to be incorporated into bedload equations to improve predictions (McEwan et al., 2004, Vollmer and Kleinhans, 2007). The occurrence of various turbulence events (sweeps, bursts, and both outward and inward interactions) have been correlated with sediment transport and the onset of particle motion (Clifford et al., 1991), with sweeps and outward interactions possibly causing the greatest sediment fluxes (Nelson et al., 1995, Dwivedi et al., 2010, Dey et al., 2011). For example, Dwivedi et al. (2010) found that during sediment entrainment, sweeps occurred simultaneously with high lift and drag forces, making a link between turbulent events and the hydrodynamic forces acting on a grain. However, large magnitude force fluctuations do not always correlate with the onset of particle motion (Diplas et al., 2008; Celik et al., 2010; Valyrakis et al., 2010b, 2013) possibly because a long duration of high magnitude forces is needed to completely move a grain out of its pocket. Impulse, which uses the product of drag force (above a critical value needed to exceed grain resistance forces) and its duration, may correlate better with sediment entrainment (Diplas et al., 2008; Celik et al., 2010; Valyrakis et al., 2010b, 2013).

Impulses that exceed a certain threshold value are often assumed to be responsible for grain movement. However, for a given particle configuration, impulses that do not cause grain motion often have the same magnitudes as those that occur during entrainment (Diplas et al., 2008; Celik et al., 2010), which suggests that a threshold impulse may not always predict sediment movement

accurately. In addition, impulses that occur just at the start of grain rotation have often been tested instead of those that occur during the entire duration of grain rotation out of its pocket (Diplas et al., 2008, Celik et al., 2010, Valyrakis et al., 2010). The inaccuracy in the impulse threshold could be partly caused by using a temporally constant drag coefficient to calculate the drag force in impulse calculations that use measured flow velocities (Diplas et al., 2008). Drag coefficients can fluctuate because of spatial variations in the pressure distribution around a grain and movement of the flow separation point in the streamwise direction (Schmeeckle et al., 2007). In theory, instantaneous drag coefficients could be systematically large during sediment motion because of the occurrence of pressure distributions around a particle that enable grain movement. These high drag coefficients would cause calculated impulses during grain motion to be higher than those that occurred while the particle was stable and had lower instantaneous drag coefficients (Celik et al., 2010). The use of such instantaneous drag coefficients in impulse calculations has not been tested and a mechanistic reason for high drag coefficients during motion has not been explored. Conversely, the instantaneous pressure distribution around a grain can be used to calculate impulses without needing a drag coefficient. Pressure measurements have only been employed to calculate drag force and impulse around an immobile grain (Hofland et al., 2005; Dwivedi et al., 2010), and therefore it is unknown if pressure data would provide more accurate calculated threshold impulses than velocity data.

In this study we calculate drag force and impulses using velocities and pressures measured around a mobile test grain before and during its full rotation out of its pocket. We use these data to explore the turbulence parameter that best corresponds to particle motion. We also test how various calculation methods of drag forces and impulses affect the correlation of these flow parameters with grain movement. Our results can be used to identify which parameterization of impulse is best used in sediment entrainment models that include the effects of turbulence. We also test whether selected drag coefficients influence the correspondence of high magnitude impulses to particle motion in our controlled flume experiments.

Methods

Flume design

All experiments were conducted in the University of Idaho's tilting flume (20 m long, 2 m wide and 1.5 m deep) (Budwig and Goodwin, 2012). Our test section was 12 m long, centered in the flume length, and lined with sediment with a median grain size of 62 mm. The bed grain size distribution was selected such that it was mostly immobile in the flow conditions that caused the

motion of a finer test grain (Figure 1.1). We used a flow straightener to decrease the upstream boundary effects, and an adjustable gate at the downstream end of the flume to establish nearly uniform flow. A test grain was positioned at the midpoint between the flume sidewalls and halfway between the upstream and downstream boundaries of the test section. We measured test grain motion at five bed slopes between 0.63% and 2.6%. For each slope, we slowly and incrementally (pausing for at least 5 minutes) increased the discharge until our test grain moved and therefore measured grain motion that was caused by turbulence rather than by a stream-wise acceleration in the mean flow. Discharge was automatically measured (at a sampling rate of 12 hz) in the flume inlet pipe using an UltraMag electromagnetic flow meter (error of 0.5%). For each slope, we captured 4-7 grain motions for a total of 26 runs.

Instrumented mobile test grain

The test grain (Figure 1.2) was constructed using a rigid, hollow, plastic sphere that was 50 mm in diameter and was evenly weighted inside with lead pellets so that its density was similar to that of granite (2.68 g/cm^3). We glued a sand layer on the test grain surface to mimic natural rock roughness. Four micro differential pressure sensors (24PCEFD6G, 12.7 x 8 mm) (at a sampling rate of 500 hz) were installed in the test grain (Figure 1.2b). We sealed one port on each pressure sensor with silicone at approximately the same moment to achieve the same referenced internal pressure, while the other port was positioned within the test grain to be exposed to fluid flow on the sphere surface. Each pressure sensor output was converted from voltages to pressures using a calibration between voltage and the product of depth, gravitational acceleration (g), and water density (ρ) that was developed by submerging the test grain at various depths in a still column of water. The pressure ports were exhumed of air using a syringe before each experimental run. A stream-wise Stereo Particle Imaging velocimetry (SPIV) (DaVis (LaVision), at a sampling rate of 10 hz) transect over the grain centerline measured the instantaneous flow velocity field during and before grain motion. Our SPIV configuration used two cameras that were focused on the test grain from one side of the flume, such that one camera was upstream, and one was downstream of the grain (Figure 1.2e). The SPIV images were calibrated for the test grain location, which was held constant throughout all experiments. A thin (<1mm) laser light sheet, generated by a dual pulsed Nd:YAG illuminated neutrally buoyant particles in the flow that were recorded by the cameras. A cross-correlation analysis of particles created a velocity vector for each interrogation region (2.2 x 2.2 mm) over the streamwise (220 mm) and the vertical directions (110 mm) of the field of view (FOV) (Figure 1.2e). From this vector field, we extracted the following three zones (Figure 1.2d): 1) a near grain profile located immediately adjacent to and upstream of the test grain, 2) one point located one grain

diameter upstream of the test grain and at a vertical position halfway up the grain, and 3) a profile one grain diameter upstream of the test grain. We used one point and a profile one diameter upstream of the grain because they represent free-stream flow conditions (Celik et al., 2010; Valyrakis et al., 2010).

We placed the test grain on three load cells (sampling rate of 500 hz) (Figure 1.2c) that were arranged in a tripod configuration and were fixed to a heavy metal plate upon which we also glued cobbles to ensure the same local roughness as that of the surrounding bed material (Figure 1.2a). We selected the simplest configuration for the load cells; their contact points with the test grain were equidistant (3 cm) and at an equal angle (46º) from horizontal (Figure 1.2c). One load cell was positioned upstream of the test grain whereas the other two were downstream on the left and right of the test grain. We measured the friction angle of the test grain (pivot angle, average of 35.5º) by repeatedly tilting the metal plate until the grain rolled from its pocket and recording the tilt angle (Kirchner et al., 1990). The test grain protrusion, or the vertical distance that it extended into the flow beyond the immediate grain upstream, was 30 mm and remained constant throughout our experiments.

When the test grain moved, it did not travel far because it was tethered to the bed with the wires of the pressure sensors that exited the bottom and downstream end of the test grain at a 45º angle toward the bed. These wires were narrow and highly flexible so that the test grain could move naturally. We observed both partial motions (or wobbles) in which the test grain never fully left its pocket and complete rotation of the test grain from its pocket. Thus, the time that represents full grain rotation was quantitatively and objectively defined by two measurements: 1) the initial disconnection of the test grain from the upstream load cell (first onset of motion), and 2) the complete test grain rotation from its pocket and disconnection from the two downstream load cells (end of grain rotation). For the pressure dataset, the time period of test grain rotation was determined using these synchronized load cell measurements. The SPIV dataset did not have the same measurement frequency as that of the load cells and was not synchronized in time, and therefore needed an independent check on the assumed timing of motion. For these data, the onset of motion was defined using the SPIV video frames, during which the start of the test grain rotation and disconnection with the upstream load cell was visible. The end of test grain motion was determined by knowing the duration of test grain motion from the load cells to determine the last SPIV video frame. For each particle motion, we used this range of video frames to determine the near grain profile (Figure 1.2d) during test grain motion. However, the simultaneous flow velocities measured one diameter upstream of the particle (Figure 1.2d) were not actually felt by the test grain during these same video frames

because of the time needed for the fluid to travel this distance to the particle. We therefore used: 1) the time-averaged streamwise velocity at the freestream point in each run and 2) the 50 cm travel distance between the free-stream point location to the test grain to calculate the fluid travel time. We offset the video frames during particle motion by this fluid travel time to determine the video frames that coincided with grain motion for the two velocity measurement zones one diameter upstream of the test grain.

Drag force and Impulse calculations

With the pressure dataset, instantaneous drag ($F_{D,p}$) and lift ($F_{L,p}$) forces were calculated with:

$$F_{D,p} = p_{U-D}A_p, \tag{1}$$

$$F_{L,p} = p_{T-B}A_p, \tag{2}$$

respectively, where p_{U-D} and p_{T-B} are the pressure differentials between the upstream and the downstream pressure sensors, and the top and bottom pressure sensors on the grain, respectively, and A_p is the particle cross-sectional area exposed to the flow based on its protrusion (following equations in Yager et al., 2007). We used the differential pressure between pressure sensor pairs to calculate drag (Hofland et al., 2005; Dwivedi et al., 2010) and lift (Dwivedi et al., 2010) forces following previous studies. The exact locations of these sensors within the test grain were restricted by the small space available. Therefore, the upstream-middle and downstream-upper sensors (Figure 1.2b) were used to calculate drag forces. A downstream middle sensor would have been better than the downstream-upper location for drag force calculations, but we could not fit a sensor in this position. The flow separation point on the test grain was above the downstream-upper pressure port (verified using SPIV images), so that the pressures collected here were good representations of the wake zone on the downstream side of the grain.

Instantaneous drag forces using the velocity dataset were calculated differently depending on the three velocity zones. For the point measurement, we assumed that the entire grain area was subjected to the same velocity, such that the drag force ($F_{D,vpt}$) was calculated using:

$$F_{D,vpt} = \frac{1}{2}C_d\rho_w u_i{}^2 A_p, \tag{3}$$

where C_d is the drag coefficient ($C_d = 0.91$ (Schmeeckle et al., 2007)), ρ_w is the density of water, and u_i is the streamwise component of velocity at the SPIV grid cell of interest (i.e. the point location here). For the two velocity profiles we first conceptually divided the grain into 22 horizontal slices located at the SPIV grid cell elevations. The lower six slices were in a SPIV shadow zone caused by rocks impeding the video view of the flow and did not have a corresponding velocity measurement. To define this portion of the velocity profiles, we assumed a logarithmic-shaped profile (Smart, 1999) between the lowest measured velocity and a zero velocity at the grain base, although many different possible velocity profiles exist, especially within the roughness layer, (Nowell and Church, 1979; Wiberg and Smith, 1987; Lawless and Robert 2000; Nikora et al., 2004). We performed this calculation for each time step in the velocity measurements. The difference in our overall results was negligible between assuming a logarithmically-shaped profile and assuming zero velocities for these six data points. The drag force for the two profiles was given by:

$$F_{D,vpr} = \frac{1}{2} C_d \rho_w \sum_{i=1}^{22} u_i{}^2 A_{p_i} \tag{4}$$

where the velocity at each grid cell (u_i) is applied to each respective cross-sectional area slice A_{p_i} (see Yager, 2007). High magnitude lift forces calculated using pressure data did not correlate with test grain motion (see results) thus, we decided not to calculate lift forces using the velocity data. The streamwise component of the immersed grain weight ($F'_g \sin(\beta)$) was added to each drag (Equations 1, 3 and 4) and lift (Equation 2) force to adjust for a downstream-directed force caused by the bed slope:

$$F'_g \sin(\beta) = (\rho_g - \rho_w)V_g g \sin(\beta)) \tag{5}$$

using the difference between the grain and water densities ($\rho_g - \rho_w$), grain volume (V_g), gravitational acceleration (g), and the downstream component of slope $\sin(\beta)$.

Three different impulses were calculated for each of the above drag forces. First, we calculated a Fixed Critical Drag (FCD) impulse, which was based on the approach of Diplas et al.

(2008). Each impulse initiated at time t_I, when the threshold of the bed perpendicular component of the grain's weight F_{Dcrit},

$$F_{Dcrit} = F'_g \cos(\beta) \tan(\alpha), \tag{6}$$

was surpassed by the instantaneous drag force, and where α is the friction angle (Wiberg and Smith, 1987). An FCD impulse (I) continued until the drag force fell below the same critical threshold at time t_f,

$$I = \int_{t_I}^{t_f} F_D \, dt$$

$$for \; F_D \, (t_i) > F_{Dcrit} \tag{7}$$

where F_D is the drag force from equations (1, 3 and 4).

For the second approach, we calculated impulses using the Decreasing Critical Drag (DCD) method (Valyrakis et al., 2013), which was based on the assumptions that 1) the critical threshold decreased as the grain rotated from its pocket because of a change in instantaneous friction angle (α), and, 2) the rate of change in α between each timestep was constant. With these assumptions, we calculated an instantaneous α to be used in equation (6) through the grain entire rotation. We assumed that α started at the measured value (35.5º) and linearly decreased to zero when the test grain was directly on top of the two downstream load cells. When α decreased through test grain rotation, the critical drag force threshold also declined, which incorporated lower magnitude instantaneous drag forces in impulse than those in the FCD method. Each DCD impulse started when the instantaneous drag force exceeded the initial F_{Dcrit} and stopped if 1) the instantaneous drag force was smaller than the instantaneous critical threshold drag (Valyrakis et al., 2013), or 2), the calculated impulse duration equaled the measured duration of grain rotation for a given run to make peak impulses at motion equivalent to those before motion. In the latter case, a new impulse was started immediately afterward and used the initial F_{Dcrit}.

Third, we calculated impulses following the Power-based Drag (PD) method, which is a modification of a turbulence parameter outlined by Valyrakis et al. (2013) and uses a proxy for the instantaneous flow power through u_i^3 instead of u_i^2 within each impulse. We computed this parameter using the DCD impulse methods outlined above, but once the duration of an impulse was determined, we replaced u_i^2 with u_i^3 in equations 3 and 4, and the final impulse calculation was completed using equations 5-7. All three impulse parameters were calculated using the three different velocity zone-based drag forces, however the pressure-based drag forces (Equation 2) could not be used with the PD impulse.

An impulse or drag force was considered to occur at motion if it overlapped at all with the known motion timeframe being tested. We used two different timeframes of motion: 1) just at the onset of motion (moment test grain comes off upstream load cell) or 2) during the full rotation of the grain. For each run, a parameter succeeded in explaining test grain motion if its magnitude was greater at the start of motion or during full grain rotation than at any time before grain movement. We then calculated the percent of grain motions that a parameter explained by summing the successful number of runs (grain motions) and dividing by the total number of experiments.

Results

We will discuss the percentage of test grain motions that were explained by our calculated parameters using four sub-categories. First, we discuss the influence of velocity measurement location. Then, for a given calculation dataset (velocity measurement location, pressure), we investigate 1) the influence of the timeframe of test grain motion (start of motion vs. full rotation), and 2) the relative performance of drag force and various impulse parameters. Finally, we discuss the impact of using velocity versus pressure measurements in the parameter calculations. Lift forces explained only 4% of test grain motions using the pressure data, and thus was disregarded because it was insignificant for the motion for our test grain. Grains with high protrusions like our test grain, are entrained largely by drag and not lift forces (Schmeeckle et al., 2007).

Influence of velocity measurement location

For the velocity-based parameters, the velocity measurement location largely affected the success of both drag force and impulse in explaining test grain motion. For a given timeframe of motion, the freestream profile-based drag force and impulse parameters generally explained more grain motions than did the equivalent parameters based on the freestream point. Exceptions to this were the PD impulse calculated for the start of grain motion and during full grain rotation, and the drag force during the full grain rotation timeframe (Figure 1.3). For the near grain profile, impulses could often not be calculated because flow velocities slowed when approaching the grain, which resulted in very low instantaneous drag forces and therefore zero impulses.

Drag force vs. impulse

Within each of the pressure-based and velocity-based parameters, we generally found the same results when comparing drag forces and impulses (Figure 1.3). For a given method and time period of calculation, impulse parameters generally explained more instances of grain motion than did instantaneous drag forces, except for the near-grain velocity profile-based parameters for reasons

discussed above. Another exception was for the pressure-based drag force and FCD, which at the start of rotation explained an equal number of grain motions. Of the three impulse parameters tested, the DCD impulse generally explained the largest percentage of test grain motions regardless of the motion timeframe considered, or dataset (velocity location or pressure) used in the calculation. However, the PD and FCD impulses both explained more grain motions than did the drag force.

Time period of grain motion

For a given dataset (velocity location or pressure) used in the calculation, the percent of grain motions explained for each drag force and impulse parameter was larger when using the full rotation time instead of just the onset of test grain motion (Figure 1.3). The percent of grain motions explained was higher with the full rotation time than with the first start of motion because peak values of a given parameter often occurred after the start of rotation. In addition, for one run, the DCD impulse that used the full rotation timeframe did not explain test grain motion, but this motion was explained with drag force using the full rotation timeframe. Thus, using the upstream velocity profile, 92% of all grain movements could be explained for the full rotation time period through a combination of DCD impulse and drag force. The only exception to the general increase in grain motions explained between the start of motion and the full rotation timeframes was with PD impulse using the freestream velocity point; the percent of grain motions explained did not change between these two timeframes.

Velocity vs. pressure-based results and the effect of measurement duration

Velocity-based drag force and impulses using any velocity location generally corresponded better to test grain motion than did pressure-based drag force and impulses (Figure 1.3). For each run, the pressure data was recoded over a longer time period than the velocity data; pressures were recorded for approximately one minute, while velocities were measured for less than 17 seconds because of the SPIV system limitations. Thus, to test the effect of dataset duration an overall parameter success, we artificially shortened the pressure measurement time period to equal the time period measured using SPIV for each run. This effectively deleted many large magnitude pressure fluctuations that occurred before test grain motion in each run. Shortened pressure-based drag forces and impulses 1) explained a higher percentage of grain motions for the full rotation time period than did the same parameters based on velocity except for the DCD impulse, and 2) explained more grain motions compared to the same parameters that used the full pressure record for both the start of motion and full rotation timeframes (Figure 1.3). These results imply that the high percentage of grain motions explained by impulse when using the velocity data may be partially caused by the

limited duration of velocity measurements prior to test grain motion. Therefore, even though DCD impulse can explain 88% of grain motions, if we had a longer velocity dataset, this percentage of motions explained could be lower. The following sections explore why impulse does not always explain grain motion.

How does C_d magnitude affect impulse success?

The average C_d is not well known for rough particles that only partially protrude into the flow and C_d values other than the one that we used may allow calculated impulses to better explain observed test grain motions. Given our results above that the DCD impulse could only explain a maximum of 88% of particle motions (Figure 1.3), we varied the C_d used to calculate the DCD, FCD, and PD impulses. For each impulse we used the upstream velocity profile and both grain motion timeframes (first onset of motion, full rotation) to test the influence of C_d variation. To vary C_d, we employed a range of widely used values for a sphere (0.47-0.91) (Roberson and Chen, 1970; Schlichting, 1960; Schmeeckle et al., 2007) and a range above (0.91-1.25) these commonly used C_d values to determine if potentially higher values could affect our results. For both timeframes of motion, the percent of grain motions explained by a given impulse parameter systematically increased with higher C_d until C_d approached 0.9. For C_d greater than about 0.9, the percent of test grain motions explained fluctuated around a relatively constant value (Figure 1.4). Our results suggest that the optimal C_d is about 0.9 for our experiments and use of a different C_d would not improve the performance of impulse.

To illustrate why impulse explains more test particle motions with higher values of C_d, we show how C_d changes the average drag force magnitude and duration, the product of which determines impulse (Figure 1.5). For one run and for each C_d, we determined the peak DCD impulse (calculated using the upstream velocity profile) that occurred in two time periods, before and during test grain motion for the full rotation time period. For each peak impulse, we extracted the average drag force magnitude and duration that were used to calculate this impulse. The average drag force gradually increased with greater C_d but also decreased in steps at certain values of C_d. This occurs because the average drag force incorporates lower instantaneous drag force magnitudes that can now exceed the critical drag force (resisting force) with higher C_d. The duration is constant with increasing C_d until a lower drag force exceeds the critical drag threshold, and then the duration increases in a step (Figure 1.5). During this run, the maximum impulse at motion exceeded the maximum impulse prior to motion when C_d was greater than or equal to 0.77. This occurred because impulse could not be calculated during test grain motion for any lower C_d, which produced instantaneous drag forces that were less than the critical drag force. Impulse is larger for values of C_d

greater than 0.77 during grain motion than before motion largely because of longer durations during motion rather than larger average drag forces. Therefore, the variation in percent of motions explained by the DCD impulse with C_d was likely caused by a balance between changing durations and magnitudes of drag forces with higher C_d. Therefore, if the C_d is incorrect, then the distribution of impulses during a run will be inaccurate, which will potentially result in peak impulses that do not correspond to test grain motion. This may explain why for C_d values less than about 0.9 in Figure 1.4, the drag force magnitude and duration combinations calculated for peak impulse may often be incorrect, which could result in greater impulses before grain motion than during grain motion.

The percent of test grain motions explained by the DCD impulse remained roughly constant when C_d values were approximately greater than 0.9 (Figure 1.4) because for all runs, the grain rotation time set the maximum duration for all impulses (see methods). Thus, when this maximum duration was met at a lower C_d, an increase in C_d did not further change the impulse duration or number of instantaneous drag forces included in each impulse (e.g. see Figure 1.5 for $C_d > 0.95$). Increasing the C_d value above about 0.9 resulted in a gradual increase in the instantaneous drag force magnitude (Figure 1.5). Therefore, because the impulse duration remained constant, any fluctuations in the percent of test grain motions explained at C_d larger than 0.91 were largely driven by the differences in drag force magnitudes before and during test grain motion.

Does instantaneous C_d improve impulse results?

Another potential explanation for impulse not explaining 100% of test grain motions is that the velocities and pressures that we used to calculate impulse are incomplete representations of the actual flow field around our test grain. The drag force is controlled by the entire pressure distribution around a grain rather than just the difference in upstream and downstream pressures that we have used. Similarly, use of the velocity profile upstream of a grain to calculate drag forces is predicated on the assumption of a temporally constant C_d, which indirectly accounts for an assumed pressure distribution around a particle at a given Reynolds number. However, recent studies (Schmeeckle et al., 2007) have demonstrated that C_d is temporally variable, likely because of changes in the full pressure distribution around a particle and flow separation location over time. We used instantaneous drag coefficients in the DCD impulse to determine if temporally variable values of C_d could better explain the particle motions than a constant C_d. We used a dimensionless version of Schmeeckle et al.'s (2007) relationship between the instantaneous C_d and the instantaneous streamwise velocity (u), which was collected at a point at one grain diameter upstream of a sphere. To nondimensionalize these data, we divided each instantaneous velocity and drag coefficient by Schmeeckle et al.'s average velocity (0.3 m/s) and average instantaneous C_d (0.76), and then fit a power function to these

dimensionless values (Figure 1.6). To use this relation to calculate instantaneous C_d in our experiments, we assumed an average C_d of 0.9, and used the average velocity at the freestream point for each run. For each timestep, the measured instantaneous stream-wise velocity at the point location was used to determine the instantaneous C_d, from which DCD impulses were then calculated.

The use of an instantaneous C_d decreased the percent of motions explained by the DCD impulse (calculated using the point velocity data) from 76% (Figure 1.2) to 50%. This occurred because high instantaneous velocities were paired with lower instantaneous drag coefficients, which effectually compressed the drag force signal (Figure 1.7) and preferentially decreased the largest impulses, which are thought to be responsible for grain motion. However, large amounts of scatter in instantaneous C_d values exist for a given instantaneous velocity in Schmeeckle et al.'s (2007) data (Figure 1.6), implying that we may not have used the correct instantaneous C_d for each instantaneous velocity measurement in our experiments.

Discussion

Implications for calculations of grain impulse

Our results demonstrate that impulse corresponded to test grain motion more often than did the instantaneous drag force, which corresponds to previous results in the literature (Diplas et al., 2008). After testing multiple methods to calculate impulse, we found an impulse that incorporated the effects of a decline in grain resistance to motion during rotation (DCD impulse) corresponded most often to the onset of particle motion, which is corroborated by others (Valyrakis et al., 2010). Therefore, for accurate predictions of the onset of particle motion using impulse, temporal changes in friction angle for a given grain size must be estimated as well as instantaneous streamwise velocities. In addition, we provided evidence that C_d selection determines the how often the peak impulse in a given run occurs at grain motion (Figure 1.5). Although changing C_d did not result in an impulse parameter explaining 100% of particle motions, selecting the correct C_d is very important for impulse to accurately predict motion.

Use of a full upstream flow velocity profile, instead of a single upstream velocity measurement, in calculations of impulse and drag force better explained our observed test grain motion. Our results suggest that spatial variability within the instantaneous velocity profile is important for grain motion. Whenever possible, a full velocity profile should be used to calculate the spatially-averaged velocity acting on a grain and to predict particle motion. Errors in predicting

instantaneous drag forces, impulses, and the onset of motion may result from using a single velocity measurement.

Observed in a few runs for both the pressure and velocity-based impulses, multiple impulses occurred during grain motion, but none were peak impulses. This suggests that in some cases, a series of low magnitude impulses may cause motion rather than a single large impulse and could explain why peak impulses do not always correspond to grain motion. Low magnitude impulses may start the test grain motion and subsequent low impulses could maintain grain movement from its pocket. A grain may not stop rotating just because an impulse event stops, given that it may still have significant momentum. We also found that impulses that occur during the full rotation of the grain correspond better to grain motion than impulses that just overlapped with the start of motion. This could imply that the impulses that occur during the rotation of a grain are essential to its motion and a peak impulse at the start of motion may not always explain the start of grain rotation. Therefore, the duration of grain rotation may be essential for predictions of grain motion using impulse because decisions would need to be made as to whether a sequence of impulses could move a particle. However, the influences of sediment sizes, shape and flow magnitudes on grain rotation time are currently unknown. Our results indicate that this information could be beneficial to use impulse to predict the onset of motion of various grain sizes.

Predictions of the spatial and temporal variations of velocities or some assumed instantaneous velocity distribution would be necessary to apply impulse calculations to the onset of sediment motion in rivers. If a simple velocity distribution is assumed, the sequencing of instantaneous velocities or drag forces would also need to be assumed or calculated to determine impulse. The instantaneous drag forces are not entirely random, but rather can have some degree of serial correlation because of the passage of coherent flow structures. This implies that better understanding of temporal variation of drag forces in different environments could be important to predict impulses accurately.

Impulse threshold and performance in explaining grain motion

We show, (Figure 1.3) as have others (Diplas et al., 2008; Celik et al., 2010), that peak values of impulse do not always correspond to the onset of grain motion. For example, three of our runs had no DCD impulse at the exact start of grain rotation or during grain rotation. Impulse can obscure high peaks in drag forces by averaging these forces over time, and in one experimental run, the instantaneous drag force correlated better with the onset of motion than did any calculated impulse parameter. For some calculation methods (e.g. single velocity point measurement), impulse also did

not explain a significantly larger number of grain motions than did the drag force. Therefore, although impulse could improve predictions of the onset of motion, this could largely depend on what data are used to calculate impulse. Additionally, in some runs, the start of grain motion could not be explained by any of the drag force or impulse parameters that we tested.

Although impulse explained more observed test grain motions than did the instantaneous drag force, we may be over-estimating the performance of impulse in our experiments because of two different factors. First, we observed that flow parameters calculated using the flow velocity explained more grain motions than those calculated using pressure. The record of velocities before test grain motion was of a significantly shorter duration than that of the pressure data. By shortening the pressure record, we verified that more test grain motions would be explained and therefore that a longer record of flow velocities before grain motion would likely result in fewer runs that were explained by impulse. Other explanations for the relatively poor performance of pressure also exist (see next section) but these do not explain why pressure-based parameters better correlated to grain motion for a shorter time record before test grain motion.

Second, we essentially used a variable impulse threshold between experimental runs to define impulse success. For example, impulse magnitudes at the onset of grain motion have been compared to impulse magnitudes before motion (Diplas et al., 2008; Celik et al., 2010) for many experiments combined. Both of these studies observed that grain motion corresponded with impulses of a certain minimum magnitude, such that a constant impulse magnitude threshold indicates grain motion. We did not use a uniform impulse threshold between all experiments to determine the percent of test grain motions explained by impulse; the impulse threshold was essentially the peak impulse that occurred prior to particle movement for each run. For both our pressure and velocity (using a velocity profile) based impulses, all peak DCD impulses that occurred before motion almost completely overlapped the range of peak DCD impulses that occurred during motion (Figure 1.8). The discrepancy between Diplas et al. (2008), Celik et al., (2010) and our results on impulse threshold could be related to differences in experimental setups that changed turbulence characteristics; our bed material was natural sediment, and our test grain was roughened. Diplas et al.'s method of applying electromagnetic forces to a smooth steel sphere resulted in direct measurements of forces being applied to the grain. Celik et al. also used smooth grains and observed a larger zone of overlap than observed in Diplas et al. between pre-motion and motion impulse magnitudes, which could be explained by their use of calculating impulses with flow velocities.

Why does impulse not always explain grain motion?

We now examine why impulse may not always explain the onset of grain motion in our experiments. We first explore the possible ways in which the collected velocity and pressure data may have affected our calculated impulses. First, our velocity dataset may have been collected too infrequently, which could have resulted in missing important high velocity magnitudes during the onset of motion. We explored the effect of using a lower frequency sampling rate by resampling the pressure-based drag forces at 10 hz to recalculate the DCD impulse at the same frequency as that used for the velocity data. The percent of grain motions explained by the pressure-based DCD impulse was not affected by this lower frequency sampling. This suggests that our frequency of PIV data collection did not affect the number of runs explained by impulse.

Second, although pressure and velocity-based calculations had similar amounts of success for the shortened pressure time record, the calculated drag forces using each data source were not always of similar magnitudes (Figure 1.2). This suggests that the calculated drag forces from both our velocity and pressure measurements each may have separate error sources. For the pressure data, using only two pressure ports on the upstream and downstream sides of the grain may not be sufficient because the pressure distribution around the entire particle determines the drag force. A more complete distribution of pressure along the surface of the grain may better represent the drag force fluctuations. Another challenge is that when the grain was in motion, the pressure ports also moved, thus we were no longer using the correct locations to calculate drag force, which resulted in lower drag forces through rotation and decreased impulse magnitudes. However, when we calculated impulses with drag forces just at the start of motion, the pressure ports had not yet moved and thus impulses were accurately calculated.

For the velocity data, measurements were in a single vertical profile along the centerline of the grain. A 3D depiction of the flow on the upstream and downstream sides of the grain may improve impulse calculations and its correspondence to test grain motion. Instantaneous drag coefficients may also be needed to indirectly account for the temporal variations in the pressure distribution around a particle and the possible shifting location of the flow separation point on a grain. Currently, it is unrealistic to estimate instantaneous drag coefficients because the exact relation between C_d with instantaneous velocity is not well established. However, when we calculated impulses using roughly estimated instantaneous C_d values, this resulted in fewer particle motions explained by the DCD impulse than when we used a constant C_d. This could imply that for many timesteps, the value of instantaneous C_d that we used was erroneous and other values within the wide C_d distribution for a given instantaneous velocity may have been more representative of the actual drag coefficient (Figure 1.6). Instantaneous C_d values may be systematically higher during grain

motion because of changes in flow structure around a grain that promote particle motion by shifting the flow separation point and causing higher drag forces. However, it is beyond the scope of this study to assign accurate instantaneous C_d estimates to calculate impulses. Finally, impulse may not always correspond to motion simply because it does not link how a grain rotates from its pocket due to each applied drag force at each timestep. Possible next steps to connect turbulent flow to the mechanics of grain rotation could include calculations of the instantaneous grain momentum (personal conversations with Furbish).

Conclusion

We measured instantaneous flow velocities and pressures around a mobile test grain to determine the turbulence parameter(s) responsible for the onset of sediment motion. The exact start of test grain motion was precisely known within each dataset, which allowed us to compare magnitudes of calculated drag force and impulse parameters prior to and during grain rotation. A given parameter explained grain motion in an experiment if its magnitude was higher during grain motion than any time before movement. Impulse corresponded more often to grain motion than did the instantaneous drag force. Of all impulse parameters tested, one that used a decreasing resisting force during grain rotation explained the largest percentage of particle motions. Use of an upstream velocity profile instead of single velocity measurement point in impulse calculations also increased the number of explained test grain motions. When using velocity to calculate impulse more test grain motions were explained when using an optimal average drag coefficient, thus drag coefficient selection is important for peak impulses to correspond well with grain motion. However, the drag coefficient for rough, naturally shaped particles is not well known. Surprisingly, we found that the start of grain rotation often occurred without an impulse (or peaks in all other parameters tested) and peak impulses did not always even occur during the full rotation of the test grain. We also did not find that any threshold value of impulse could differentiate between impulse magnitudes that occurred during and prior to grain motion. This implies either that impulse is not always the flow parameter that can explain and predict particle motion or that the velocity and pressure measurements used to determine drag forces, and therefore impulse, were not adequate. Changes in the complete pressure field around a particle actually control the instantaneous drag force and these variations may not be properly characterized by measurements of pressures at two locations on a grain, or by the use of a velocity profile upstream of a grain combined with a constant drag coefficient. However, incorporation of simple calculations of temporally variable drag coefficients did not increase the number of grain motions that were explained by impulse. To use impulse to predict the onset of

motion, further research should understand how instantaneous velocities are related to instantaneous drag coefficients. Future research should also investigate whether the movement of the flow separation point could systematically occur during grain motion and explain why a threshold impulse does not always exist.

Literature Cited

Budwig, R. and Goodwin, P. (2012). The Center for Ecohydraulics Research Mountain StreamLab – a facility for collaborative research and education. In W. Aung, V. Ilic, O. Mertanen, J. Moscinski, & J. Uhomoibhi (Eds.), Innovations 2012: world innovations in engineering education and research (pp. 17 – 28). Potomac, Maryland, USA: iNEER.

Buffington, J. M., Dietrich, W. E., and J. W. Kirchner (1992). Friction angle measurements on a naturally formed gravel streambed: Implications for critical boundary shear stress. Water Resour. Res. 28, 411–425.

Celik, A. O., Diplas, P., Dancey, C. L., & Valyrakis, M. (2010). Impulse and particle dislodgement under turbulent flow conditions. Physics of Fluids (1994-present), 22(4), 046601.

Church, M. (1978). Palaeohydrological reconstructions from a Holocene valley. Fluvial Sedimentology, Can. Soc. Petrol. Geol. Mem., vol. 5, edited by A. D. Miall, pp. 743–772, Can. Soc. of Petrol. Geol., Calgary, Alberta, Canada.

Clifford, N. J., McClatchey J., & French J. R. (1991). Measurements of turbulence in the benthic boundary layer over a gravel bed and comparison between acoustic measurements and predictions of the bedload transport of marine gravels. Sedimentology, 38, 161–171.

Dey, S., Sarkar, S., & Solari, L. (2011). Near-bed turbulence characteristics at the entrainment threshold of sediment beds. Journal of Hydraulic Engineering,137(9), 945-958.

Diplas, P., Dancey C. L., Celik A. O., Valyrakis M., Greer K., & Akar T. (2008). The role of impulse on the initiation of particle movement under turbulent flow conditions. Science. 322, 717-720.

Dwivedi, A., Melville, B., & Shamseldin, A. Y. (2010). Hydrodynamic forces generated on a spherical sediment particle during entrainment. Journal of Hydraulic Engineering, 136(10), 756-769.

Fenton, J., & Abbott J. E. (1977). Initial movement of grains on a stream bed: The effect of relative protrusion, Proc. R. Soc. London, Ser. A, 352, 523-537.

Gomez, B., & Church M. (1989). An assessment of bed load sediment transport formulae for gravel bed rivers. Water Resources Research, 25(6), 1161-1186.

Groot, C., & L. Margolis. 1991. Pacific salmon life histories. University of British Columbia Press, Vancouver.

Hofland, B., Battjes J. A, & Booij R. (2005). Measurement of fluctuating pressures on coarse bed material. J. Hydraul. Eng. 131, 770– 781.

Kirchner, J. W., Dietrich W.E., Iseya F., & Ikeda H. (1990). The variability of critical shear stress, friction angle, and grain proftrusion in water worked sediments, Sedimentology, 37, 647-672, doi:10.1111/j.1365-3091.1990.tb00627.x.

Lawless, M., & Robert, A. (2001). Three-dimensional flow structure around small-scale bedforms in a simulated gravel-bed environment. *Earth Surface Processes and Landforms: The Journal of the British Geomorphological Research Group*, *26*(5), 507-522.

Kondolf, G.M. (2000). Assessing Salmonid Spawning Gravel Quality, Transactions of the American Fisheries Society, 129:1, 262-281, DOI: 10.1577/1548659 (2000) 129 < 0262: ASSGQ > 2.0.CO; 2.

McEwan, I., Sørensen, M., Heald, J., Tait, S., Cunningham, G., Goring, D., & Willets, B. (2004). Probabilistic modeling of bed-load composition. J. Hydraul. Eng. 130 (2), 129-139.

Nowell, A. R., & Church, M. (1979). Turbulent flow in a depth-limited boundary layer. *Journal of Geophysical Research: Oceans*, *84*(C8), 4816-4824.

Nelson, J. M., Shreve R. L., McLean S. R., & Drake T. G. (1995). Role of near-bed turbulence structure in bed-load transport and bed form mechanics. Water Resources Res. 31(8), 2071- 2086.

Nikora, V., Koll, K., McEwan, I., McLean, S., & Dittrich, A. (2004). Velocity distribution in the roughness layer of rough-bed flows. *Journal of Hydraulic Engineering*, *130*(10), 1036-1042.

Perron, J. T., Lamb, M. P., Koven, C. D., Fung, I. Y., Yager, E., & Ádámkovics M. (2006). Valley formation and methane precipitation rates on Titan. Journal of Geophysical Research: Planets, 111(E11).

Robinson, C. T., Aebischer, S., & Uehlinger, U. (2004). Immediate and habitat-specific responses of macroinvertebrates to sequential, experimental floods. *Journal of the North American Benthological Society*, *23*(4), 853-867.

Roberson, J.A. & Chen, C.K. (1970). Flow in conduits with low roughness concentration. J. Hydraul. Eng., 96,941–957.

Schlichting, H. (1960). *Boundary layer theory* (Vol. 960). New York: McGraw-Hill.

Schmeeckle, M. W., J. M. Nelson, & R. L. Shreve (2007). Forces on stationary particles in near-bed turbulent flows, J. Geophys. Res., 112, F02003, doi:10.1029/2006JF000536.

Shields, A. (1936). Application of similarity principles and turbulence research to bed-load movement.

Smart, G. (1999). Turbulent velocity profiles and boundary shear in gravel bed rivers, J. Hydraul. Eng., 125(2), 106 – 116, doi:10.1061/(ASCE)0733-9429(1999)125:2(106).

Valyrakis, M., Diplas P., Dancey C. L., Greer K., & Celik, A. O. (2010). Role of instantaneous force magnitude and duration on particle entrainment, J. Geophys. Res., 115, F02006, doi:10.1029/2008JF001247.

Valyrakis M., Diplas P., Dancey C. L., & Celik A. O. (2010b). Incipient rolling of coarse particles in water flows: a dynamical perspective. In River Flow 2010: Proceedings of the International Conference on Fluvial Hydraulics Braunchweig, Germany, 08–10 September, Dittrich, Koll, Aberle, Geisenhainer (eds), Taylor and Francis: 769–776.

Valyrakis, M., Diplas P., & Dancey C. L. (2013). Entrainment of coarse particles in turbulent flows: An energy approach. Journal of Geophysical Research: Earth Surface, 118(1), 42-53.

Vollmer, S. & Kleinhans M. G. (2007). "Predicting incipient motion, including the effect of turbulent pressure fluctuations in the bed." Water Resources Research 43.5.

Wiberg, P. L., &. Smith J. D. (1987). Calculations of the critical shear stress for motion of uniform and heterogeneous sediments, Water Resour. Res., 23, 1471–1480.

Yager, E. M., Kirchner, J. W., & Dietrich, W. E. (2007). Calculating bed load transport in steep boulder bed channels, Water Resour. Res., 43, W07418, doi:10.1029/2006WR005432.
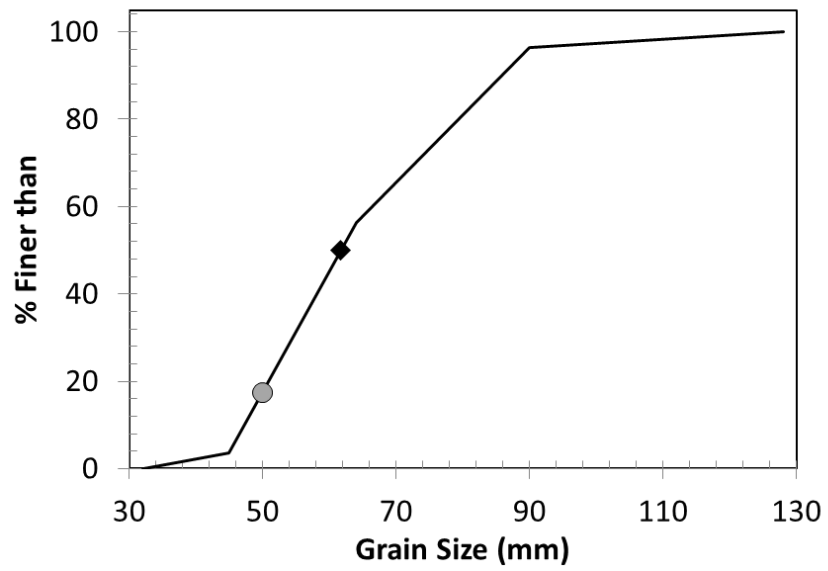
Figure 1.1 Bed grain size distribution with the mobile test grain size (grey circle) and the median grain size for the bed material (black diamond) indicated.
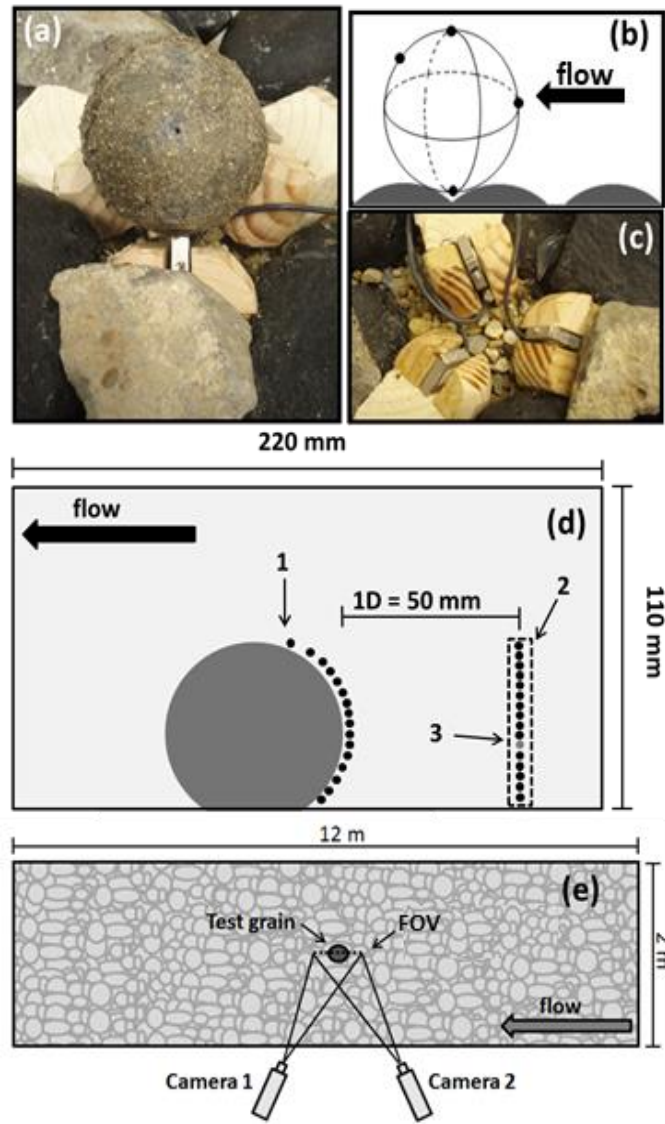
Figure 1.2 (a) The instrumented mobile test grain. (b) Pressure was measured with pressure transducers embedded in the grain with locations used for drag and lift force calculations indicated with black dots. (c) Load cells were used to indicate the timing of grain motion. (d) Velocities were measured with Stereo Particle Imaging Velocimetry with data analysis at three indicated locations 1) profile located on the upstream side of the grain, 2) vertical profile 1 grain diameter upstream of the test grain, and 3) a point located one diameter upstream of the test grain, and at half of the grain height. (e) The test grain (grey dot) was positioned in the flume test section and the SPIV field of view (FOV) passed through (dotted line) the center of the grain.
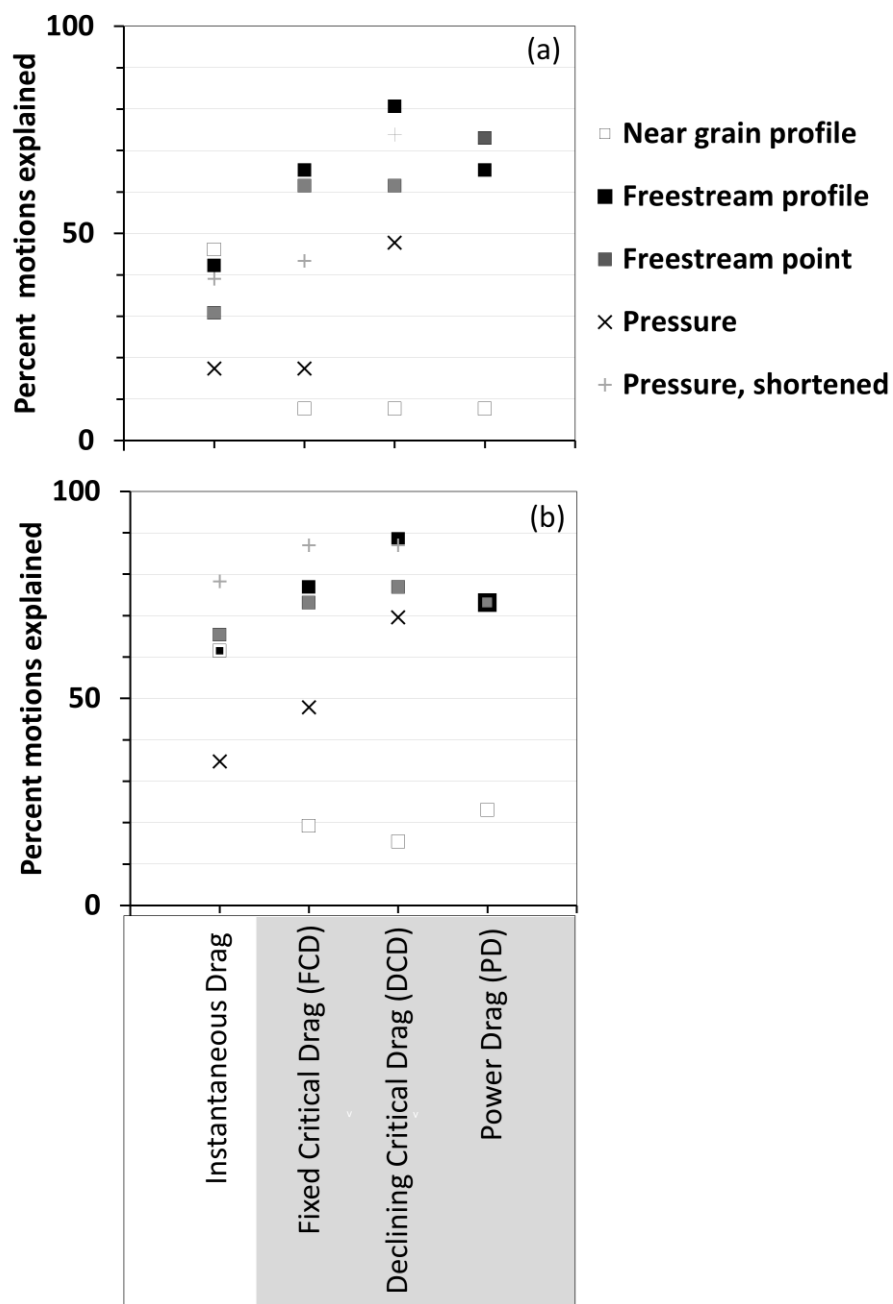
Figure 1.3 Percent of the total number of test grain motions that were explained by various methods of calculating drag force and impulse (label shaded in grey). Parameters calculated using velocity (squares) and pressure (x and +) are shown for timeframes of motion: (a) at the start of rotation and (b) throughout full rotation.
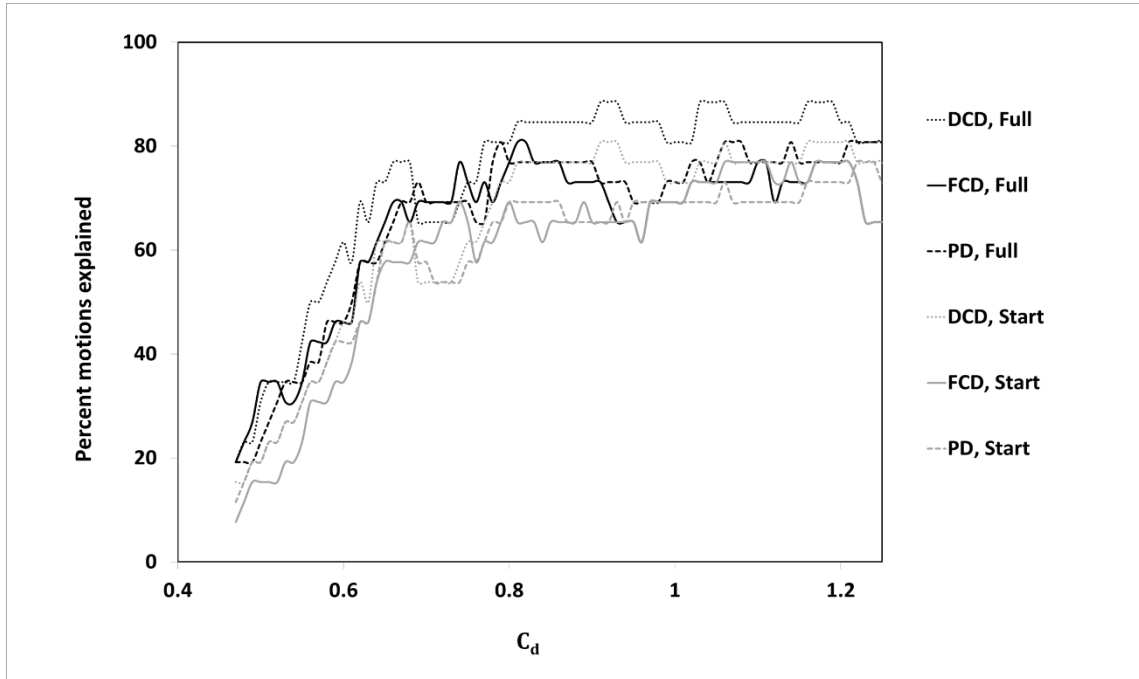
Figure 1.4 The effect of drag coefficient on the percentage of motions explained when using each impulse parameter (Decreasing critical Drag (DCD), Fixed Critical Drag (FCD), and Power Drag (PD)) for the start of rotation (start) and for the full rotation time period (full).
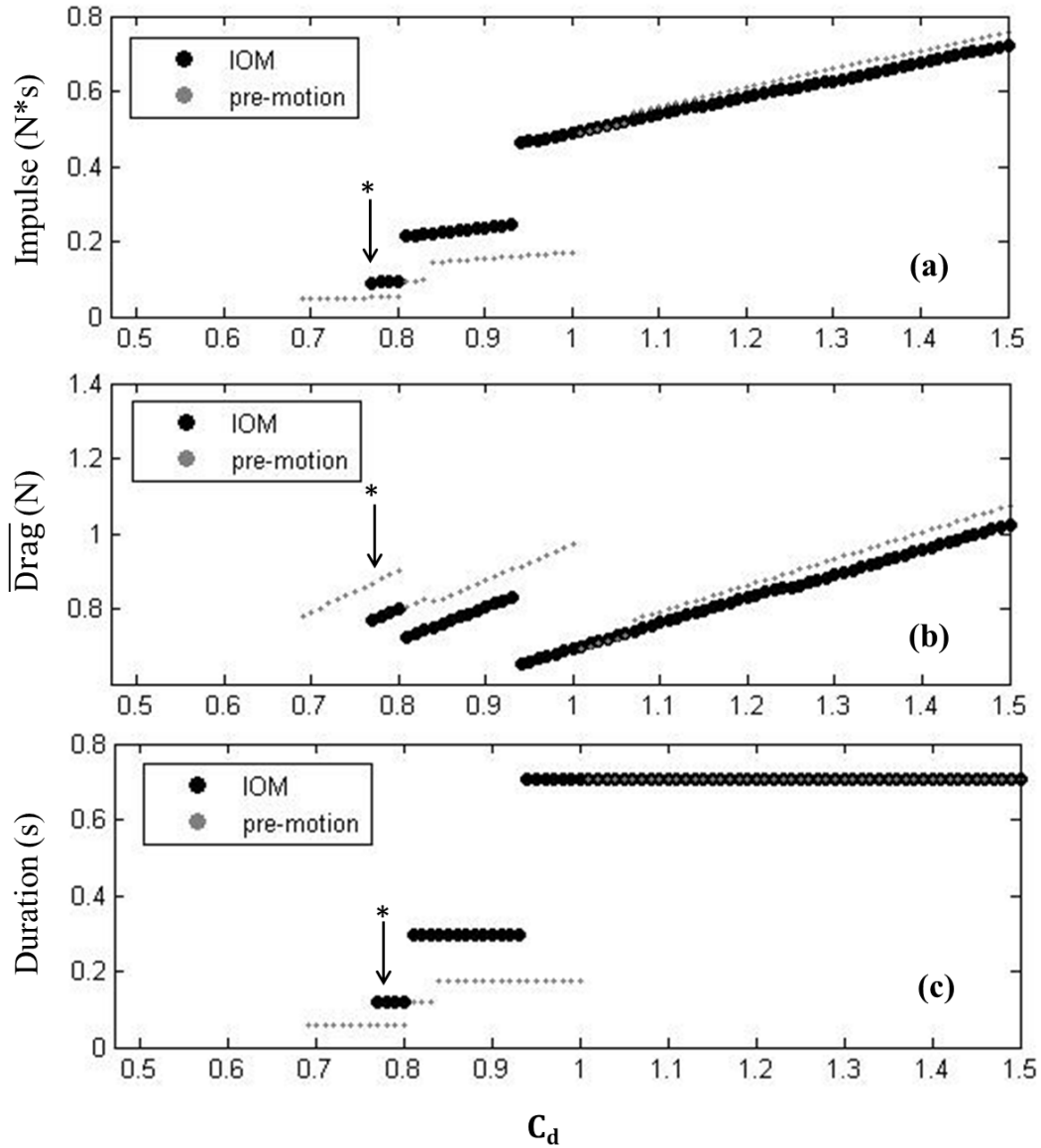
Figure 1.5 (a) Peak DCD impulses before motion (grey dots) and during the full rotation time (black circles) calculated using different drag coefficients during one run. (b) The average drag force and (c) impulse duration used to calculate these peak impulses also are shown as a function of C_d. For this run, the peak impulse at motion first exceeded the peak impulse prior to motion at $C_d = 0.77$, which is indicated with an asterisk (*).
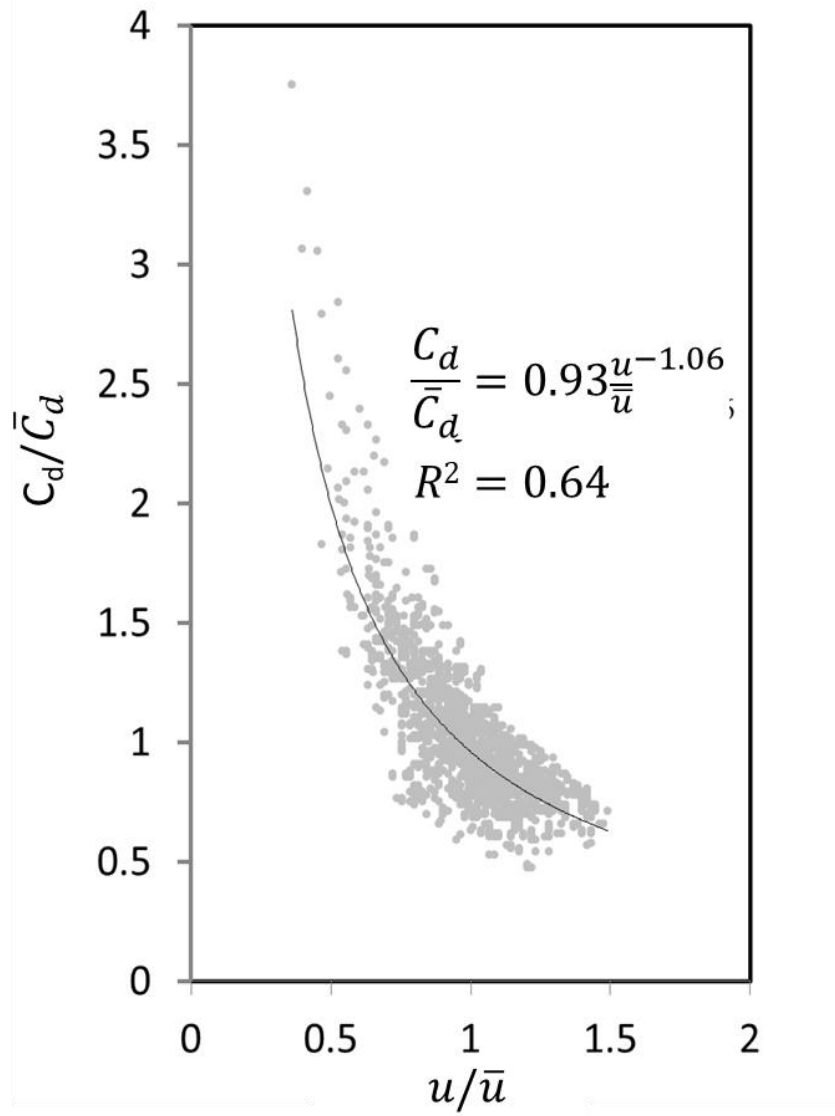
Figure 1.6 Relation between the dimensionless instantaneous streamwise velocity and dimensionless instantaneous drag coefficient for a sphere, developed using data (grey circles) from Schmeeckle et al. (2007).
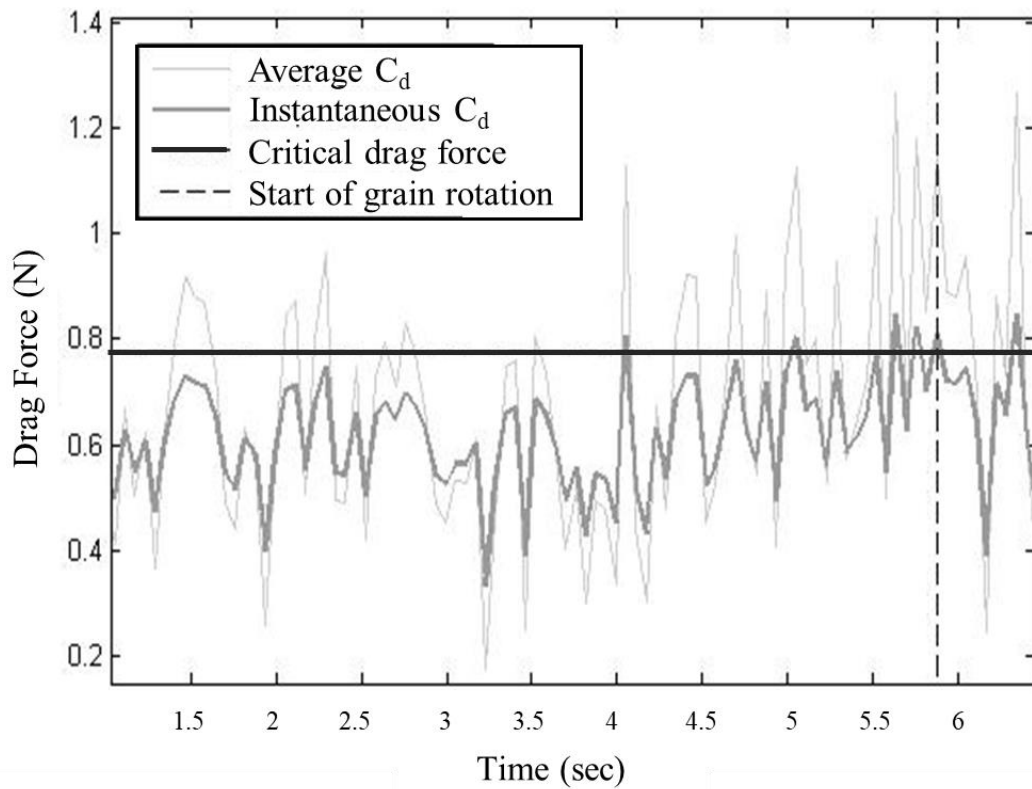
Figure 1.7 Drag forces calculated for one run using the (i) average Cd = 0.91 (light grey line) and or (ii) instantaneous C_d (dark grey line; equation from Figure 1.6). When drag forces exceed the critical drag force (black line) an impulse is initiated for all impulse types. For DCD impulses the critical drag decreases once an impulse is initiated but this is not shown in the figure.
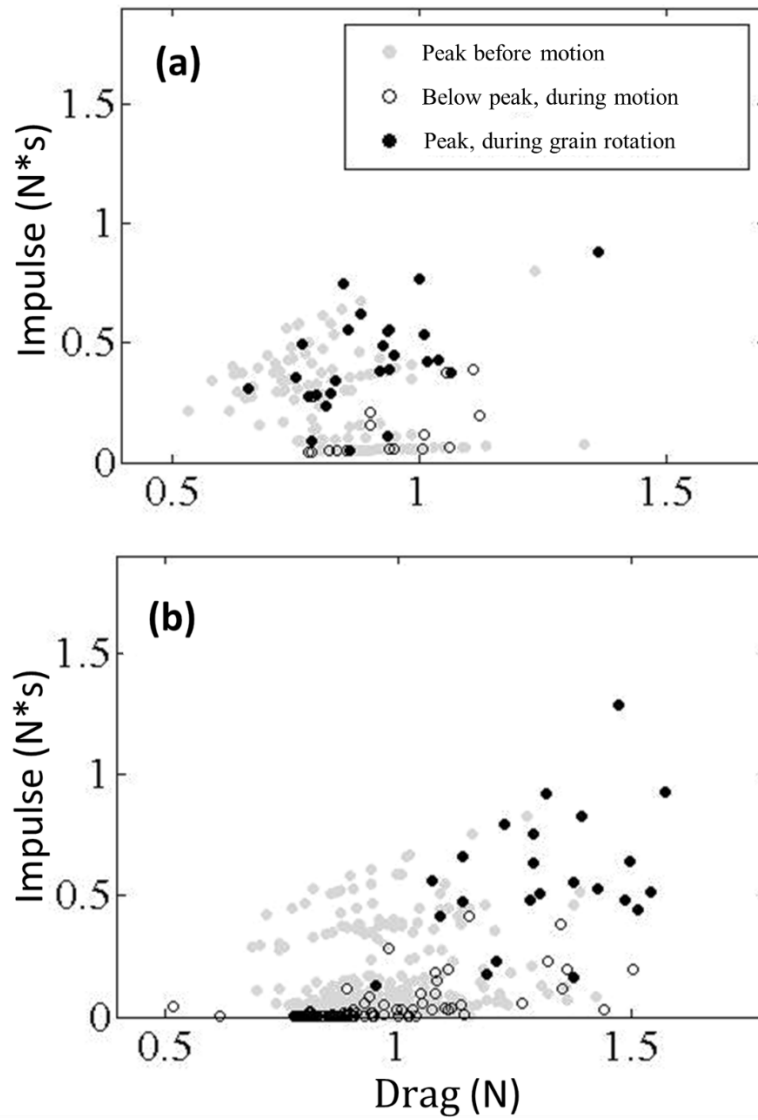
Figure 1.8 DCD impulse magnitudes for all runs calculated using (a) pressure and (b) velocity data. The overlap in the peak impulses during test grain rotation (black), and the impulses that occurred before motion (grey) indicate there is not an impulse threshold.

Chapter 2: Large grain submergence and the increase in critical Shields stress with slope

Abstract

Understanding and predicting the onset of grain motion in rivers is imperative for improving restoration efforts or minimizing loss of property though urbanized reaches. Bedload equations are often inaccurate partly because of uncertainty in the shear stresses that cause the start of sediment motion (critical Shields stresses). Although often assumed to be a constant value for the median bed grain size, the critical Shields stress can increase with greater channel slope, which has been potentially explained by a wide variety of processes. To fully understand this phenomenon, we conducted a series of flume experiments through a range of channel slopes in which we measured the critical Shields stress and near-bed flow velocities at the onset of motion of a mobile test grain with a fixed pocket geometry. We used two bed configurations, one with and one without large immobile grains, to explore the effects of large boulders on critical Shields stresses. Contrary to previous studies that have shown a general increase in critical Shields stress with greater channel slope or relative roughness, the critical Shields stress in our experiments only increased when (1) boulders were added, and (2) the boulder tops began to emerge from the flow. Otherwise, critical Shield stresses remained roughly constant with greater slope or relative roughness. We tested many of the previously hypothesized reasons for critical Shields stress increases with channel slope and found that none could fully explain our experimental observations. We hypothesize that in our data and in natural rivers, many of the observed changes in critical Shields stress are caused by decreases in boulder submergence and increases in boulder concentration with higher slopes. These changes in boulder properties drive previously unaccounted for complex variations in the flow structure that affect the onset of motion of finer, more mobile particles.

Introduction

The onset of sediment motion in rivers occurs when forces resisting the movement of grains are overcome by near-bed fluid forces. For close to a century, studies have explored variables that affect grain motion beyond its size, such as the angle the grain must rotate to leave its resting pocket (Buffington et al., 1992), the height the grain extends into the flow column (Kirchner et al. 1990), the time-averaged velocity of near-bed flow (Wohl and Thompson, 2000), and the effects of turbulence fluctuations (Nelson et al., 1995; Diplas et al., 2008; Celik et al.; 2010), all of which demonstrate

sediment motion to be highly complex because of its multi-scale and dynamic nature. The spatially and temporally averaged shear stress responsible for the onset of motion of the median bed grain size (D_{50}) is often represented by a critical shear stress (Shields, 1936)

$$\tau_c = \rho_w ghS. \tag{1}$$

where ρ_w is the density of water, g is the gravitational acceleration, h is the reach-averaged flow depth when particle motion occurs, and S is the channel slope. Critical shear stresses for the median grain size are made dimensionless using the critical Shields stress (τ_c^*) which is:

$$\tau_c^* = \frac{\tau_c}{(\rho_s - \rho_w)gD_{50}}, \tag{2}$$

where ρ_s is the sediment density. The critical Shields stress has a wide range of values (e.g. Kramer, 1935; Neill and Yalin, 1969; Graf and Pazis, 1977; Wilcock, 1988) and is usually between about 0.03-0.086 (Buffington and Montgomery, 1997) for lower gradient channels without large roughness elements. Many studies have also shown that τ_c^* increases with greater channel slope and relative roughness (ratio of the characteristic roughness length, such as grain size, and the flow depth) (e.g. Neill 1967; Bathurst et al., 1985; Shvidchenko et al., 2001; Mao et al., 2008). Many explanations for these observed increases in τ_c^* have been previously proposed.

One hypothesized cause for the increase in critical Shields stress with higher channel slopes is that at higher slopes, there is more morphological flow resistance from large immobile boulders and steps comprised of boulders and/or wood. Thus, a significant portion of the reach-averaged shear stress is borne by these roughness elements, decreasing the shear stress on mobile sediment for which critical Shields stresses are measured (Ferguson, 2012; Schneider et al., 2015, Yager et al., 2007, Nitsche et al., 2011, Buffington and Montgomery, 1999, Wilcox et al., 2006). Although accounting for morphologic roughness can cause critical Shields stresses to be within the range of values reported for lower gradient channels, it does not incorporate the grain-scale flow mechanisms that actually cause sediment motion. Another hypothesized reason for these τ_c^* changes include increases in particle jamming (Zimmerman and Church 2001) and greater bed structure with higher channel slopes but Prancevic et al., (2015) did not find a systematic increase in grain friction angle (controlled by bed structure) with channel slope.

Increases in relative roughness have also been used to explain why critical Shields stresses increase with steeper channel slopes. A decrease in turbulence intensity with greater relative roughness (occurs at steeper slopes) could be caused by a decrease in eddy size with relatively shallower flows (Lamb et al., 2008). A change in velocity profile shape could also result from high

relative roughness, which may result in a lower near-bed, time-averaged velocity acting on particles (Lamb et al., 2008). A related explanation is that for steep channel slopes, relatively mobile grains emerge from the flow depth near the onset of motion, causing increased resistance from the mobile fraction rather than resistance being caused by large, relatively immobile boulders or morphologic roughness (Lamb et al., 2008; Lamb et al., 2017). Lift forces on such emergent grains are also low or negative, thus requiring higher drag forces and higher critical Shields stresses for motion to occur (Lamb et al., 2017). These hypotheses are largely based on laboratory flume studies in which there were no boulders, but boulders are common in natural steep channels and could affect the flow structure and possibly the onset of finer sediment motion. All of these many interacting processes make it difficult to disentangle how each contribute to the observed increase in critical Shields stress with slope and relative roughness.

Here, we investigate many of these explanations by measuring τ^*_c and near-bed flow conditions for a mobile test grain for a range of channel slopes in a laboratory flume. By using a single grain and holding the test grain pocket geometry constant, we eliminated uncertainties in identifying the onset of motion, and removed grain arrangement as a potential cause for changes in critical Shields stresses in our experiments. We used two bed arrangements, one with a fixed cobble bed, and one with fixed cobbles and evenly spaced boulders, which were used to isolate the effects of relative roughness from the effects of boulders.

Methods

Flume, test grain and bed configurations

We conducted experiments at the University of Idaho tilting (up to 10% gradient) laboratory flume which is 20 m long, 2 m wide, and 1.5 m deep (Budwig and Goodwin, 2012). Boundary effects were decreased by (1) considering a test section in the middle 12 m of the flume, (2) using a flow straightener at the upstream end of the flume, (3) using an adjustable tailgate at the downstream end of the flume to achieve uniform flow over the test section, and (4) using smooth glass walls to lower wall friction.

We measured local and flume-averaged flow conditions that occurred during the motion of a mobile test grain. This test grain was a 50 mm diameter sphere that was roughened by gluing a single layer of sand on its surface and had a density of 2.65 g/cm^3 by being evenly weighted inside with lead pellets. Motion was defined as when the test grain rotated downstream and completely out of its pocket. Between each run, the test grain was manually positioned in the same exact orientation on a

stand with three points of contact that were 3 cm from one another (fixed test grain pivot angle of 35.5°). This stand was fixed to a heavy metal plate (18 x 23 cm) upon which cobbles were glued such that the bed configuration immediately adjacent to the grain did not vary between runs. Protrusion of the test grain, or the height that it extended into the flow above the height of the immediate upstream grain, was 3 cm (defined in Kirchner et al., 1990).

While maintaining the same test grain position on the fixed metal plate, we conducted two sets of experiments that used different underlying bed arrangements. The first set of experiments used a bed of natural mixed-sized cobbles and the test grain was placed in the center of the test section both longitudinally and cross-sectionally (Figure 2.1c). Test grain motion occurred before any of the cobbles because of its smaller size, lower friction angle, and greater protrusion. The second set of experiments used the same cobbles, but also included 0.25 m diameter concrete boulders that were evenly-spaced (0.75 m between boulder centers) in staggered rows (Figure 2.1d). For this bed arrangement, we used two test grain locations such that the test grain was placed (1) midway between boulders with its distance from the boulder centers being 0.35 m and 0.65 m in the cross stream and longitudinal directions, respectively, and (2) 0.33 m downstream of a boulder (Figure 2.1d). The average and standard deviation of boulder heights within the test section were 0.21 m, and 0.02 m, respectively.

The maximum possible channel slope for runs with and without boulders was determined by observing the flow depth necessary to move the test grain for a given slope; only flows deep enough to conduct Stereo Particle Imaging Velocimetry (SPIV) were included. Thus, maximum bed slopes or runs with and without boulders were 10% and 2.6%, respectively. The minimum slope for the experiments without boulders, was the lowest flume slope (0.63%), whereas for the runs with boulders, the minimum slope was that at which the test grain could still be moved (1.0%). For the experiments without boulders, we used bed slopes of 0.63%, 1.0%, 1.4%, 2%, and 2.6%, and for runs with boulders we used bed slopes of 1.0%, 2.5%, 5%, 7%, and 10%.

We first identified the motion-causing flow conditions for each bed configuration, grain position, and bed slope by slowly and incrementally (pausing for at least 5 minutes) increased the flow discharge until the test grain moved from its pocket. At this flow discharge, we measured 20 flow depths along the flume wall at randomly selected locations within the test section and averaged all measured values for a given test grain motion. Discharge was automatically measured (at a sampling rate of 12 hz) in the flume inlet pipe using an UltraMag electromagnetic flow meter (error of 0.5%). For each bed slope, we measured 3-7 test grain motions and recorded the flow discharge, flow depth

and near-bed velocities for each motion. This resulted in 26 and 23 experiments for the no boulder and boulder runs, respectively.

To measure near-bed velocities upstream of the test grain, we used Stereo Particle Imaging Velocimetry in a thin, streamwise transect that bisected the test grain longitudinally (DaVis (LaVision), sampling rate of 10 hz). Our SPIV configuration used two cameras that were focused on the test grain from one side of the flume, such that one camera was upstream, and one was downstream of the grain (Figure 2.1, c and d). The SPIV data were calibrated for each test grain location. A thin (<1mm) laser light sheet, generated by a dual-pulsed Nd:YAG illuminated neutrally buoyant particles in the flow that were recorded by the cameras. We used a glass-bottomed boat, positioned just on the water surface, that allowed laser sheet illumination to be unobstructed by the water surface as they entered the water column from above the flume. A cross-correlation analysis calculated the instantaneous velocity vector for each interrogation region (2.2 x 2.2 mm) over the streamwise (220 mm) and the vertical directions (110 mm) within SPIV field of view. We extracted one velocity profile from this vector field that was located one grain diameter upstream from the test grain. The profile started at the first interrogation region that was unobstructed by the cobble bed and extended to the height of the test grain. We used the SPIV data for all runs, 19 runs without boulders and 4 runs with boulders. In the experiments with boulders, SPIV data for any runs were excluded when excessive bubbles caused (1) laser starbursts to overexpose video images, which resulted in no velocity vectors, and (2) erroneous velocity vectors because the SPIV software tracked many bubbles that did not follow the flow direction.

Relative roughness calculations

Many different roughness lengths have been used to estimate flow resistance (Rickenmann et al., 2001; Smart et al., 2002) and no uniformly accepted definition of relative roughness (ratio of roughness length to flow depth) exists. We measured the bed grain size distributions (following Wolman, 1954) to compute D_{84}, which is the 84th percentile of the measured grain size distribution. Relative roughness was then defined as the commonly used D_{84}/h_{avg}, where h_{avg} is the reach-averaged flow depth. This definition of relative roughness does not accurately depict the amount of boulder submergence in our experiments; it shows that boulders were emergent when they were really submerged. Given the large spatial variability in the flow depth, the only way to show true boulder submergence was by using the flow depth upstream of boulders instead. Therefore, we used a protrusion relative roughness (PRR) to capture the flow around a representatively large grain on the bed. To calculate roughness lengths for PRR, we used the bed elevation distribution (e.g. Ferguson 2007, Johnson 2017) using a Keyence LK-G402 laser displacement sensor (sub-millimeter accuracy;

measurement every 1 mm laterally and 1 cm longitudinally). The elevations of the boulder tops were measured manually because their elevations were outside of the laser range. From the combined manual and laser-scan elevation data, we calculated a $k_{sm} = E_{90}-E_{50}$ which is defined as the difference between the 90th and 50th percentiles of bed elevations in a given experiment. The 90th percentile approximates the elevation of the grains with the highest protrusion whereas the 50th percentile is the median bed elevation. Thus, the difference between these two percentiles in bed elevation is an approximation for the protrusion of a representatively large grain on the bed. We then define PRR as $E_{90}-E_{50}/h_{Lg}$ where h_{Lg} was determined in boulder runs as the average of flow depths immediately upstream of the 90th percentile bed height, which represents the flow depth upstream of the representatively large grain (i.e. the boulders). Others have observed that using depths upstream of boulders improve relative roughness calculations (e.g. Monsalve et al. 2017). For the runs without boulders, we computed h_{Lg} by using the average flow depth because the flow depth was generally uniform in these experiments.

Explaining critical Shield stress increases with slope

To test various theories for the increase of critical Shield stress with greater slopes, we used an equation to predict the critical Shield stress (Lamb et al., 2008) that uses grain-scale physical parameters from our experiments

$$\tau^*_c = \left\{\left(\frac{u_*^2}{\langle \bar{u}^2 \rangle}\right)\left(\frac{\tau_T}{\tau_T - \tau_B}\right)\right\} * \left\{\left(\frac{2}{C_D}\right)\left(\frac{\tan\phi_0 - \tan\beta}{1 + (F_L/F_D)\tan\phi_0}\right)\left[\frac{V_s}{A_{xs}D}\frac{1}{r}\left(\frac{\rho_s}{\rho_w} - \frac{V_{ss}}{V_s}\right)\right]\right\}, \tag{3}$$

and is based on the assumption that a grain will move when driving forces of lift (F_L) and drag (F_D) just exceed resisting forces. In this equation, $\langle \bar{u}^2 \rangle$ denotes a vertical averaging of all streamwise velocities computed or measured at each ith elevation above the bed, β is the bed-slope angle, ϕ_0 is the friction angle, C_D is the drag coefficient, A_{xs} is the bed-perpendicular test grain area exposed to the flow, V_s is the volume of the test grain, and V_{ss} is the portion of the grain that is submerged. In our experiments, the mobile test grain is always submerged, so the V_{ss}/V_s ratio always equaled 1. Equation (3) indirectly accounts for the shear stress borne by morphologic features such as boulders and steps using a shear stress ratio, where τ_T is the total shear stress (calculated using equation 1), and τ_B is the shear stress partitioned to morphologic elements, which here are boulders. In equation (3), $\frac{\bar{u}}{u_*}$ is the dimensionless velocity defined as the ratio of the double averaged velocity over the exposed grain height ($\bar{u}$) and the shear velocity (u_*). The dimensionless velocity can be calculated using a number of velocity profile equations averaged over the grain height such as the logarithmic

profile or the quadratic equation. We test both of these velocity profile equations here to see if they accurately predict the near-grain dimensionless velocity and could explain observed critical Shields stresses. The quadratic velocity profile (Lamb et al., 2008) is

$$\left(\frac{\bar{u}}{u_*}\right)_i = \frac{z_i}{\alpha_1 k_{sm}}\left(1 - \left(\frac{z_i}{2k_{sm}}\frac{k_{sm}}{h_m}\right)\right), \tag{4}$$

where velocities are computed at each ith elevation (z) and then averaged over the grain height, and h_m and k_{sm} are the average depth and roughness lengths used to predict flow velocities. Another explanation for an increase in critical Shields stress with slope is that the magnitude of turbulence fluctuations is reduced at higher relative roughness. The dimensionless streamwise turbulence intensities can be predicted as a function of relative roughness using

$$\frac{\sigma_{u,max}}{u_*} = \alpha_2\left[5.62\log\left(\frac{h_m}{k_{sm}}\right) + 4\right], \tag{5}$$

where $\alpha_1 = 0.12$ and $\alpha_2 = 0.2$ and are empirically derived constants, $\sigma_{u,max}$ is the maximum turbulence intensity in the streamwise direction, (see Lamb et al., (2008) for details). In equation 5, a single value of the turbulence intensity was assumed for all i^{th} elevations. Following Lamb et al. (2008), equation 5 and the vertical average of equation 4 were summed such that the total dimensionless velocity used in equation 3 was

$$\frac{u_*^2}{\langle \bar{u}^2 \rangle} = 1\Big/\left(\left(\frac{\bar{u}}{u_*}\right)_{avg} + \frac{\sigma_{u,max}}{u_*}\right)^2. \tag{6}$$

We also used the vertical average of all calculated velocities at each ith elevation from the logarithmic velocity profile equation to calculate an average $\left(\frac{\bar{u}}{u_*}\right)_{avg}$, which was then combined with equation (5) to determine the total dimensionless velocity.

Selecting roughness lengths for equations (4) and (5)

We investigated if a single roughness length (k_{sm}) could be used to accurately predict dimensionless average velocities, turbulence intensities and critical Shields stresses for all experiments (both with and without boulders). To test this, we varied the assumed roughness lengths between predictions. We used a k_{sm} equal to the D_{50} and D_{84} of the bed grain size distribution as well

as a roughness length from the bed elevation distribution to calculate the large roughness protrusion (see discussion above about roughness length definitions) (Table 2.1). To predict critical Shields stresses for each experiment, we used the different predictions of the total dimensionless velocity for each roughness length, a τ_B of zero, and our measured bed slope in equation 3 and iterated on depth (h_m) until we obtained a solution.

Boulder shear-stress partitioning in equation (3)

Equations 4 and 5 already include the effects of relative roughness, which in theory can include boulders as roughness elements, on near-bed velocities. Thus, the shear stress partitioning in equation 3 is an additional measure to account for the fact that only a portion of the total shear stress acts on the relatively mobile bed sediment. We used the measured reach-averaged streamwise velocity (U) for each run to calculate the shear stress borne by the mobile grain fraction (τ_m) following the approach of Yager et al., (2007)

$$\tau_T - \tau_B = \tau_m = \frac{\rho C_m U^2}{2},$$
<div align="right">(7)</div>

where C_m is the drag coefficient of the mobile grain fraction (0.047). For one set of calculations, we used this shear stress in the denominator of the shear stress ratio in equation (3) to test whether accounting for shear-stress partitioning would improve critical Shields stress predictions. For most critical Shields stress predictions discussed below, we simply assumed that this shear stress ratio was one.

Comparison with measured values

We compared the predicted $\left(\frac{\bar{u}}{u_*}\right)_{avg}$ and dimensionless turbulence intensities to the equivalent parameters measured using SPIV. For the measured dimensionless velocities, we estimated the shear velocity with $u_* = \sqrt{\tau/\rho}$, combined with equation 1 using the reach-averaged estimates of depth and bed slope for each run. We used the vertical and temporal average of the measured velocity profile to calculate $\bar{u}$ for each run. To calculate the measured dimensionless turbulence intensities, we calculated the turbulent fluctuation for each location in the profile and each measurement time as the difference between the instantaneous streamwise velocity and the time-averaged velocity at that location. We then calculated the root mean square (RMS) of these turbulent fluctuations at each location in the profile. The maximum turbulence intensity was the largest value of this RMS within the velocity profile for a given run. We also input the measured total

dimensionless velocity into Equation 3 to test if this equation predicted the measured critical Shields stresses accurately when provided with the known velocity conditions in each run.

Results and Discussion

Measured critical Shields stresses

Contrary to most previously published studies, we did not observe a continuous increase in the critical Shields stress with slope (Figure 2.2a). For our experiments without boulders, the critical Shields stress was constant with steeper slopes, and for a given slope adding boulders resulted in a constant increase in critical Shields stress. In addition, for some slope ranges within the boulder experiments, the critical Shields stresses were also somewhat constant. Bed slope does not provide a physical explanation for the increase in critical Shields stress, so we tested if the critical Shields stress also increased with greater relative roughness, which was defined in two different ways here (D_{84}/h_{avg} and PRR). Previous studies have demonstrated a systematic increase in τ^*_c with higher values of D_{84}/h_{avg}, but we did not observe a regular increase in critical Shield stresses with relative roughness (Figure 2.2b). Instead we observed 1) that the critical Shields stress is constant with D_{84}/h_{avg} for runs without boulders, 2) an irregular increase in critical Shield stress with D_{84}/h_{avg} for no boulder runs, and 3) for the same D_{84}/h_{avg} very different critical Shields stresses for runs with and without boulders. Additionally, D_{84}/h_{avg} did not accurately characterize the actual k_{sm} to flow depth ratio for experiments with or without boulders. For example, in our experiments without boulders, all grains were always fully submerged in every experiment, but a value of $D_{84}/h_{avg}=0.9$ suggests near emergence from the flow depth. Also, in the experiments with boulders, we observed that the boulders tops started to emerge at a D_{84}/h_{avg} value of only 0.8, but this value would technically depict submergence. We note that use of D_{50} instead of D_{84} in the relative roughness definition would also result in similar problems for the boulder runs. This suggests that the common definition of relative roughness that employs grain size is not accurately depicting the observed submergence conditions in our experiments.

We therefore now discuss the variation of critical Shields stresses with PRR, which accurately depicts the actual relative roughness conditions in our experiments (Figure 2.2c). In the experiments without boulders (called Group 1 here), the cobbles were always fully submerged, thus PRR values were well below unity. In the experiments with boulders, there were three distinct groups of experimental conditions: (1) both cobbles and boulders were characterized by being fully submerged, resulting in PRR values much less than unity (Group 2), (2) cobbles were completely submerged, but

the boulders were nearly emergent and PRR was near one in Group 3, and (3) cobbles were fully submerged but PRR was greater than one and boulders completely emerged from the flow surface (Group 4).

The critical Shields stresses were constant within each group except for Group 3 (Figure 2.3c). Although we observed an increase in the critical Shields stress with greater PRR, it was not a systematic change but rather occurred discretely in two steps: (1) with the addition of boulders (critical Shields stresses increase between Groups 1 and 2) and (2) when the boulder tops emerge from the flow (Group 3).

What explains observed variations in critical Shields stress with PRR?

We step through previously hypothesized explanations for why the critical Shields stress increases with slope and whether such theories are supported by our more complex results as well as by expected conditions in natural rivers. We distinguish between roughness caused by large, relatively immobile grains (e.g. boulders) that typically emerge from the flow and that driven by finer, more mobile sediment for which critical Shields stresses are typically determined.

Increase in grain friction with relative roughness

The increase in critical Shields stress with slope has been attributed to a drastic increase in the bed friction coefficient when a bed of cobbles emerged from the flow (Lamb et al., 2017). Lamb et al. (2017) deduced that because there were no relatively large grains on the bed, that measured increases in flow resistance at high relative roughness values were from grain friction rather than from morphologic drag from large obstacles. This greater grain friction decreases the flow velocity and could make sediment more difficult to move. Considering that the cobbles in their experiments were immobile (glued to the flume bed) and emergent from the flow, these experiments may be more analogous to a field of emergent immobile boulders rather than the flow conditions experienced by finer, more mobile sediment at the onset of motion. Although finer, more mobile sediment can move when unsubmerged, critical Shields stresses for most grain sizes, except boulders, are usually experienced in natural steep rivers when grains are fully submerged. We therefore conclude that the increase in flow resistance with higher relative roughness that is observed by Lamb et al. (2017) is likely similar to higher flow resistance caused by boulder emergence from the flow. This situation is analogous to the increase in flow resistance with boulder emergence from the flow and therefore greater τ^*_c, in Group 3 of our experiments. The increase in flow resistance and τ^*_c in Group 3 could be caused by changes in large-scale flow patterns around large immobile grains when they emerge from the flow (see below). However, this cannot explain the increase in τ^*_c between Groups 1 and 2

(boulder addition) in which all sediment sizes (boulders, cobbles, and test grain) were fully submerged. We conclude that higher mobile grain resistance does not explain our observed changes in τ^*_c with PRR.

No lift on finer, more mobile grains

At higher slopes and PRR, the emergence of grains from the flow could also make them less mobile (Lamb et al., 2017) because of a decrease in lift forces. However, this cannot explain the increase in critical Shields stress in our Group 3 (boulders emerge from flow) or between Groups 1 and 2 (boulder addition) for our experiments because the test grain and all other cobbles were completely submerged in all runs. Furthermore, as we stated above, in natural rivers, most grains are submerged at the onset of motion in steep streams, portrayed by $h_{avg}/D_{50} > 1$ in previously published studies (e.g. Parker and Klingeman 1982; Ashworth et al., 1992). A decrease in lift forces could explain the high critical Shields stresses for boulders in steep streams because these large grains could protrude through the flow at their onset of motion.

Changes in grain arrangement with steeper slopes

A systematic increase in critical Shields stress with greater channel slope is often observed in flume experiments without simulated boulders (Shvidchenko et al., 2001, Prancevic et al., 2015). In some of these studies, high critical Shields stresses are associated with mobile grain emergence from the flow, which we discussed in the previous section. However, even for submerged grain conditions, more regular increases in τ^*_c with slope occur (Shvidchenko et al., 2001, Prancevic et al., 2015) than what we observed. In these studies, the critical Shields stress is usually determined for the entire bed using the reference transport rate method; onset of sediment motion is assumed to occur at a very low measured bedload flux. We hypothesize that in these studies, the observed increase in critical Shields stress with slope could be caused by having more stable grain configurations, and therefore greater resistance to motion, with higher slopes. This is similar to the jammed state hypothesis of Zimmerman and Church (2001) in which grains become more interlocked and possibly angular at steeper slopes. Here, we propose that in these previous experiments, grains could have lower protrusion and higher friction angles with steeper slopes. Our experiments controlled for these particle scale factors by using a fixed grain pocket and monitoring the motion of a single test grain. This could explain why we observe a roughly constant critical Shields stress for Group 1 (no boulders) even with increases in slope. One study has demonstrated that friction angles do not increase with steeper slopes in natural channels, but they largely focused on boulder-sized sediment that was arranged into steps (Prancevic et al, 2015). Therefore, an open question remains as to

whether the arrangement of finer, more mobile grains can explain observed increases in τ^*_c with slope in natural rivers.

Turbulence intensities and the average velocity near the bed decrease with slope

Decreases in the time-averaged near-bed velocity and near-bed turbulence intensities with higher relative roughness (and slope) could explain the increase in critical Shields stress with slope (Bayazit, 1975; Wang and Dong, 1996; Nikora and Goring, 2000; Lamb et al., 2008). To explore this hypothesis, we employed a force balance that predicts critical Shields stresses (equation 3) using various equations that calculate the mean near-bed velocity and turbulence intensities (see methods) as functions of relative roughness (Lamb et al., 2008). Here, we explore predicted critical Shields stresses as functions of slope because the flow depth upstream of boulders (and PRR) is not calculated by these equations. If these equations correctly predict our measured velocities, turbulence intensities, and critical Shields stresses, then a decrease in dimensionless turbulence intensities and average velocities with greater relative roughness could possibly explain the measured changes in critical Shields stress.

We first verified that if we used our measured dimensionless near-bed velocities and turbulence intensities in equation 3, the predicted critical Shields stresses would be close to our measured values. To do this, we replaced equations 4-5 with our measured dimensionless velocities and turbulence intensities, which allowed us to ignore the effects of boulder partitioning ($\tau_B = 0$) given that these velocity measurements occurred immediately upstream of our mobile test grain. We obtained predicted critical Shields stresses that generally matched our measured values (Figure 2.3), which suggested that equation 3 would predict relatively accurate critical Shield stresses with correct near-bed velocities and turbulence intensities. However, critical Shields stresses were underpredicted for slopes less than 6% and over predicted for slopes greater than 6%, which could suggest that the average flow velocity and turbulence intensity may not be the exact measures of velocity that should be used to predict particle motion. Impulse, or the integral of the applied fluid force over the duration that this force that exceeds a resisting force, may be better correlated to grain motion than drag and lift forces alone (Diplas et al., 2008; Celik et al., 2010; Smith et al., in progress). However, this is outside the scope of our current study and we proceed with the assumption that equation (3) is roughly accurate when provided the right information.

Although changes in measured mean velocities and turbulence intensities can partly explain our observed changes in τ^*_c, this does not explicitly demonstrate 1) whether both of these flow parameters systematically decrease with greater slope and 2) whether such hypothesized decreases in

flow velocity and turbulence intensity accurately predict, and therefore explain, our measured τ^*_c variations with slope. To explore if decreased turbulence intensities occur at steeper slopes and explain our observed critical Shields stresses (Lamb et al., 2008), we first only included the measured average velocities in equation 3 and disregarded the measured turbulence intensities in critical Shields stress calculations (Figure 2.4). For low slopes (S < 4%) removing turbulence intensities only made a small difference in the predicted critical Shields stresses, but for higher slopes when the boulders were emergent, removing the turbulence intensities resulted in greater errors in critical Shields stresses. This result implies changes in turbulence intensities with relative roughness do not primarily explain our observed critical Shields stress variations except possibly at high slopes, which are characterized with emergent roughness elements. In all of subsequent predictions, we assume that τ_B is zero for beds with and without boulders and use the dimensionless mean velocities and turbulence intensities calculated from equations 4 and 5, respectively. The measured turbulence intensities were predicted reasonably well using equation 5 regardless of the k_{sm} definition used (Figure 2.5c). We conclude that although turbulence intensities may not always be needed to explain observed critical Shields stress variations (see above), the hypothesis that they decrease with greater slope and relative roughness is further confirmed in our experiments.

No single k_{sm} definition allowed equations 3 and 4 to accurately predict the measured τ^*_c (Figure 2.5a) or measured dimensionless average flow velocity (Figure 2.5b), respectively. For the runs without boulders, using a very low roughness length definition ($k_{sm}=E_{90}-E_{50}$) resulted in predicted dimensionless average velocities and critical Shields stresses that were closest to their measured equivalents. Other studies have shown that predicted reach-averaged velocity profiles are more accurate when using roughness length scales smaller than D_{50} (Monsalve et al., 2016). However, for this k_{sm} definition, the predicted dimensionless average velocities for the cobble-only bed decreased with steeper slopes whereas the measured velocities increased with slope; the velocity predictions matched our measured velocities more closely at the lowest slope and progressively became less accurate with increasing slope and relative roughness. We conclude that the hypothesis of decreasing dimensionless mean near-bed flow velocities with greater slope and relative roughness is not supported for our runs without large roughness elements. However, it is surprising that that the critical Shields stress magnitudes were predicted fairly accurately from these incorrectly predicted dimensionless mean velocities when $k_{sm}=E_{90}-E_{50}$. We note though that the measured τ^*_c are constant for the cobble bed whereas the predicted τ^*_c slightly increase with slope.

For the experiments with boulders, no single definition of k_{sm} accurately predicted the dimensionless mean velocities or critical Shields stresses for the entire range of bed slopes. At

shallow slopes (<4%), the boulders were submerged and no k_{sm} definition (measured D_{50}, D_{84}, or E_{90}-E_{50} for the mixed boulder-cobble bed) provided accurate dimensionless mean velocity or critical Shields stress predictions. For steeper slopes (with emergent boulders), both critical Shields stresses and mean velocities were predicted accurately when k_{sm} was defined using the boulder-cobble bed D_{50}. We note that the roughness definition of E_{90}-E_{50} that provided relatively accurate predictions of dimensionless mean velocity and τ^*_c for the cobble-only bed significantly over-estimated τ^*_c for the boulder-cobble runs when the measured value of E_{90}-E_{50} was used for these runs. We conclude that for beds with boulders, the hypothesis that the dimensionless mean near-bed flow velocity systematically declines with higher slope and relative roughness is also not fully supported by our data (Figure 2.5b). Rather, the dimensionless mean flow velocity and τ^*_c changes with slope appear to be largely defined by when the boulders are submerged or emergent (Figure 2.3). Measured dimensionless mean flow velocities and τ^*_c only vary slightly even when slope and relative roughness increase, as long as boulders do not switch between emergent and submerged conditions (Figures 3, 5a). We also tested alternative velocity profile equations for use in equation (3) such as the logarithmic profile equation and a modified version of equation 3 with a variable α_1 (Monsalve et al., 2017). The logarithmic profile did not systematically improve the mean velocity or critical Shields stress predictions over the use of equation 3. The variable α_1 caused multiple critical Shield stress solutions for a given slope and were therefore omitted from our analysis.

We could not obtain reasonable critical Shields stress predictions using a single roughness length definition for experiments with and without boulders. If the velocity profile equations are accurate, a single k_{sm} definition should apply for all bed configurations and relative submergence conditions for use in the field to make critical Shield stress predictions. This implies that something is missing in the velocity profile equation and associated hypothesis (decreasing dimensionless mean velocity with higher relative roughness) that does not explicitly account for boulder effects on the flow and on the onset of motion of finer sediment. Finally, the increase in τ^*_c between Groups 1 and 2 with the same PRR implies that relative roughness associated changes in dimensionless mean velocities and turbulence intensities cannot explain many of our observed variations in τ^*_c. Furthermore, the fact that τ^*_c remains constant with increasing PRR within each of Groups 1, 2 and 4 further implies that relative roughness associated changes are not the dominant controls on τ^*_c in our experiments.

Drag caused by boulders

Higher drag forces born by immobile boulders and morphologic roughness elements are also a hypothesized cause of increases in critical Shields stresses with steeper slopes. For the same PRR values, we observed greater critical Shields stresses for beds with boulders (Group 2) than for beds without boulders (Group 1) (Figure 2.2c). The critical Shield stress did not vary between the two test grain positions for the boulder runs, therefore the magnitude of this increase between Groups 1 and 2 appears to be independent of the test grain location with respect to the boulders. It could be hypothesized that with boulder addition in Group 2, more of the total shear stress is borne by these immobile grains and less is available for movement of our test grain, thereby increasing τ^*_c. In addition, the roughly constant values of τ^*_c with increasing PRR for each of Groups 1, 2 and 4 could be explained by the fraction of the total stress that is borne by the boulders remaining roughly constant within each of these groups. The increase in τ^*_c within Group 3 could be caused by greater stress borne by the boulders as they switch from submerged (e.g. C_d=0.4, sphere) to emergent conditions (e.g. C_d=1.2, cylinder).

To test this theory and to account for boulder shear stress partitioning, we used the roughness definition of k_{sm}= E_{90}-E_{50} for the cobble-only bed inequations 4 and 5, and used equation 7 to calculate the shear stress borne by boulders (τ_m). We used the cobble bed k_{sm} because this roughness length allowed the critical Shields stresses to be predicted fairly accurately for the no boulder runs (see above). Furthermore, use of cobble-boulder bed roughness length combined with stress-partitioning could incorrectly account for the effects of the boulders twice in τ^*_c calculations (i.e. over compensation for effects of boulders) by both altering the roughness length and reducing the stress on the test grain. Use of stress-partitioning calculations in equation 3 provided predicted critical Shields stresses that more closely followed the patterns of the measured values. This shows that using measured reach-averaged velocities in equation 7 combined with a low k_{sm} in equation 3 could result in reasonable critical Shields stresses. However, if the measured velocity is not known, the variation of the drag coefficient of the immobile grains (see Yager et al., 2007) with relative submergence would need to be known or assumed. Although these calculations imply that our observed changes in τ^*_c could be partly explained by the effects of boulder drag, the actual mechanistic effects of boulders on the near-bed flow near our test grain are still not part of stress-partitioning equations.

Flow around boulders

None of the above reasons fully explain why we observed an increase in τ^*_c when boulders were added (Group 1 vs Group 2) and when boulders began to emerge from the water surface (Group 3). They also do not entirely explain why τ^*_c remained approximately constant with increases in PRR

within Groups 1, 2 and 4. Our results suggests that changes in relative grain roughness may not be the major driver of τ^*_c variations. Instead, τ^*_c is controlled by variations in near-bed velocities and pressure distributions that act on individual grains and that are caused by three different possible bed configurations: a lack of boulders, submerged boulders, and emergent boulders. Further investigations into the flow characteristics around submerged and emergent boulders would need to be completed to determine the mechanistic change in flow that is driven by boulder presence. However, for τ^*_c increases when boulders emerge from the flow, a possible explanation could be greater flow resistance from an increase in velocities in the cross-stream direction from flow circulating around boulders.

We hypothesize that for channels with steep slopes, the onset of motion occurs when boulders emerge from the flow, whereas in lower gradient channels, entrainment occurs when boulders are submerged, or no boulders exist. The flow structure around boulders would be quite different in these conditions, as well as the pattern of erosion and deposition around the boulders. The change in bed surface locations relative to boulders where finer, more mobile sediment is found with different boulder submergence could also be related to the increase in observed critical Shields stress with slope. Boulders cause large spatial variations in near-bed flow velocities (Monsalve et al., 2016), which impact locations of finer sediment deposition and are partly controlled by the boulder relative submergence (Shamloo et al., 2001, Papanicoluaou et al., 2011). For example, Shamloo et al. (2001) observed that when flow depth was greater than boulder height, sediment deposition occurred directly downstream of boulders and scour occurred on boulder sides. When the boulder tops emerged from the flow, deposition was repositioned to the sides of the boulders. Thus, an overall increase in near-bed velocities may result requiring a higher flow stage for grain motion to occur, and therefore an increase in critical Shields stress.

Implications for natural rivers

In natural streams, as channel slope increases the flow depth typically declines and the concentration and size of boulders often increases. Our experiments measured conditions without boulders and with a constant boulder concentration through a range of channel slopes, however in natural settings a continuum of boulder size and concentration exists. As the number of boulders increase with steeper slopes we might expect an increase in τ^*_c similar to what we saw between Groups 1 and 2. In addition, as the boulders become less submerged (bigger diameters, lower flow depths) at greater bed slopes, we would also expect an increase in τ^*_c similar to what we see in Group 3 (or between Group 2 and 4). The combination of these factors could result in the observed gradual

increase in τ^*_c in the field. We have isolated these two reasons (boulder submergence, boulder concentration) for the increase in critical Shields stress, however changes in bed configurations such as the formation of step-pools and cascade morphologies that are not present in our experiments might also be a factor in the field. Such variations in channel morphology as well as possible irregular changes in boulder size and concentration, likely contribute to the scatter in the relation between τ^*_c and channel bed slope.

Conclusions

We conducted a set of laboratory experiments in which we found step-wise increases in critical Shields stresses with greater relative roughness. These step increases in τ^*_c occur when large immobile grains (boulders) are added to the flow, and when the boulder tops emerged from the flow. Otherwise, τ^*_c, remained approximately constant with increasing relative roughness. The observed increase of critical Shield stress with steeper channel slopes in natural rivers may therefore be related to the gradual increases in the concentration of boulders and the decrease of boulder submergence with greater stream gradients. We tested a wide range of other possible causes for our observed changes in τ^*_c. For example, we found that although turbulence intensities decrease with greater relative roughness, these changes were not always needed for accurate τ^*_c predictions. Decreasing near-bed average velocities with greater relative roughness did not systematically occur in our experiments and were not always predicted accurately with the use of quadratic or logarithmic profile equations. Thus, such velocities were unlikely to explain our observed τ^*_c variations with relative submergence. Although incorporating the effects of boulder stress partitioning improved τ^*_c predictions and could explain some of the observed changes in τ^*_c, stress-partitioning does not necessarily provide a mechanistic explanation for the actual near-bed forces on mobile sediment that likely change with boulder addition and emergence from the flow. Further investigations are needed to explore the changes in velocities around boulders with a range of submergences to fully explain increases in critical Shields stresses with channel slope.

Literature Cited

Ashworth, P. J., R. I. Ferguson, P. E. Ashmore, C. Paola, D. M. Powell, and K. L. Prestegaard (1992). Measurements in a braided river chute and lobe, 2, Sorting of bed load during entrainment, transport, and deposition. *Water Resour. Res*., *28*, 1887–1896.

Bathurst, J. C. (1985). Flow resistance estimation in mountain rivers. *Journal of Hydraulic Engineering*, *111*(4), 625-643.

Bayazit, M. (1975). Free surface flow in a channel of large relative roughness, *J. Hydraul. Res.*, 14(2), 115-126.

Budwig, R. and Goodwin, P. (2012). The Center for Ecohydraulics Research Mountain StreamLab – a facility for collaborative research and education. In W. Aung, V. Ilic, O. Mertanen, J. Moscinski, & J. Uhomoibhi (Eds.), Innovations 2012: world innovations in engineering education and research (pp. 17 – 28). Potomac, Maryland, USA: iNEER.

Buffington, J. M., Dietrich, W. E., and J. W. Kirchner (1992). Friction angle measurements on a naturally formed gravel streambed: Implications for critical boundary shear stress. Water Resour. Res. 28, 411–425.

Buffington, J. M., & Montgomery, D. R. (1997). A systematic analysis of eight decades of incipient motion studies, with special reference to gravel-bedded rivers. *Water Resources Research*, *33*(8), 1993-2029.

Buffington, J. M., & Montgomery, D. R. (1999). A procedure for classifying textural facies in gravel-bed rivers. *Water Resources Research*, *35*(6), 1903-1914.

Celik, A. O., Diplas, P., Dancey, C. L., & Valyrakis, M. (2010). Impulse and particle dislodgement under turbulent flow conditions. Physics of Fluids (1994-present), 22(4), 046601.

Diplas, P., Dancey C. L., Celik A. O., Valyrakis M., Greer K., & Akar T. (2008). The role of impulse on the initiation of particle movement under turbulent flow conditions. Science. 322, 717-720.

Ferguson, R. (2007). Flow resistance equations for gravel-and boulder-bed streams. *Water resources research*, *43*(5).

Ferguson, R. I. (2012). River channel slope, flow resistance, and gravel entrainment thresholds. *Water Resources Research*, *48*(5).

Graf, W. H., & Pazis, G. C. (1977). *Les phénomènes de déposition et d'érosion dans un canal alluvionnaire; érosion et déposition; un concept probabiliste; Weak sediment transport* (No. BOOK). EPFL.

Johnson, J. P. (2017). Clustering statistics, roughness feedbacks, and randomness in experimental step-pool morphodynamics. *Geophysical Research Letters*, *44*(8), 3653-3662.

Kirchner, J. W., Dietrich W.E., Iseya F., & Ikeda H. (1990). The variability of critical shear stress, friction angle, and grain proftrusion in water worked sediments, Sedimentology, 37, 647-672, doi:10.1111/j.1365-3091.1990.tb00627.x.

Kramer, H. (1935). Sand mixtures and sand movement in fluvial levels. Trans. Am. Soc. Civ. Eng., Vol. 100, pp. 798-838.

Lamb, M. P., Brun, F., & Fuller, B. M. (2017). Direct measurements of lift and drag on shallowly submerged cobbles in steep streams: Implications for flow resistance and sediment transport. *Water Resources Research*, *53*(9), 7607-7629.

Lamb, M. P., Dietrich, W. E., & Venditti, J. G. (2008). Is the critical Shields stress for incipient sediment motion dependent on channel-bed slope?. *Journal of Geophysical Research: Earth Surface*, *113*(F2).

Mao, L., Uyttendaele, G. P., Iroumé, A., & Lenzi, M. A. (2008). Field based analysis of sediment entrainment in two high gradient streams located in Alpine and Andine environments. *Geomorphology, 93(3-4), 658-383*.

Mao, L., Uyttendaele, G. P., Iroumé, A., & Lenzi, M. A. (2008). Field based analysis of sediment entrainment in two high gradient streams located in Alpine and Andine environments. *Geomorphology*, *93*(3-4), 368-383.

Monsalve, A., Yager, E. M., & Schmeeckle, M. W. (2017). Effects of Bed Forms and Large Protruding Grains on Near-Bed Flow Hydraulics in Low Relative Submergence Conditions. *Journal of Geophysical Research: Earth Surface*, *122*(10), 1845-1866.

Neill, C. (1967). "Laboratory study of scour of coarse uniform bed material." Technical Rep., Research Council of Alberta, Alberta, Canada.

Neill, C. R., & Yalin, M. S. (1969). Quantitative definition of beginning of bed movement. *Journal of the Hydraulics Division*, *95*(1), 585-588.

Nelson, J. M., Shreve R. L., McLean S. R., & Drake T. G. (1995). Role of near-bed turbulence structure in bed-load transport and bed form mechanics. Water Resources Res. 31(8), 2071- 2086.

Nikora, V., & Goring, D. (2000). Flow turbulence over fixed and weakly mobile gravel beds. *Journal of Hydraulic Engineering*, *126*(9), 679-690.

Nitsche, M., Rickenmann, D., Turowski, J. M., Badoux, A., & Kirchner, J. W. (2011). Evaluation of bedload transport predictions using flow resistance equations to account for macro-roughness in steep mountain streams. *Water Resources Research*, *47*(8).

Parker, G., P. C. Klingeman, & D. G. McLean (1982). Bedload and size distribution in paved gravel-bed streams. *J. Hydraul. Div. Am. Soc.Civ. Eng*., *108*, 544–571.

Prancevic, J. P., & Lamb, M. P. (2015). Particle friction angles in steep mountain channels. *Journal of Geophysical Research: Earth Surface*, *120*(2), 242-259.

Rickenmann, D. (2001). Comparison of bed load transport in torrents and gravel bed streams. *Water resources research*, *37*(12), 3295-3305.

Schneider, J. M., Rickenmann, D., Turowski, J. M., Bunte, K., & Kirchner, J. W. (2015). Applicability of bed load transport models for mixed-size sediments in steep streams considering macro-roughness. *Water Resources Research*, *51*(7), 5260-5283.

Shields, A. (1936). Application of similarity principles and turbulence research to bed-load movement.

Shvidchenko, A. B., Pender, G., & Hoey, T. B. (2001). Critical shear stress for incipient motion of sand/gravel streambeds. *Water Resources Research*, *37*(8), 2273-2283.

Smart, G. M., Duncan, M. J., & Walsh, J. M. (2002). Relatively rough flow resistance equations. *Journal of Hydraulic Engineering*, *128*(6), 568-578.

Smith, H. J., Yager, E. M [in progress]. Inspecting impulse as the parameter responsible for grain motion.

Wang, J. J., & Dong, Z. N. (1996). Open-channel turbulent flow over non-uniform gravel beds. *Applied scientific research*, *56*(4), 243-254.

Wilcock, P. R., & Southard, J. B. (1988). Experimental study of incipient motion in mixed-size sediment. *Water Resources Research*, *24*(7), 1137-1151.

Wilcox, A. C., Nelson, J. M., & Wohl, E. E. (2006). Flow resistance dynamics in step-pool channels: 2. Partitioning between grain, spill, and woody debris resistance. *Water Resources Research*, *42*(5).

Wohl, E. E., & Thompson, D. M. (2000). Velocity characteristics along a small step–pool channel. *Earth Surface Processes and Landforms: The Journal of the British Geomorphological Research Group*, *25*(4), 353-367.

Wolman, M. G. (1954). A method of sampling coarse river-bed material. *EOS, Transactions American Geophysical Union*, *35*(6), 951-956.Yager et al., 2007.

Yager, E. M., Kirchner, J. W., & Dietrich, W. E. (2007). Calculating bed load transport in steep boulder bed channels. *Water Resources Research*, *43*(7).

Zimmermann, A., & Church, M. (2001). Channel morphology, gradient profiles and bed stresses during flood in a step–pool channel. *Geomorphology*, *40*(3-4), 311-327.
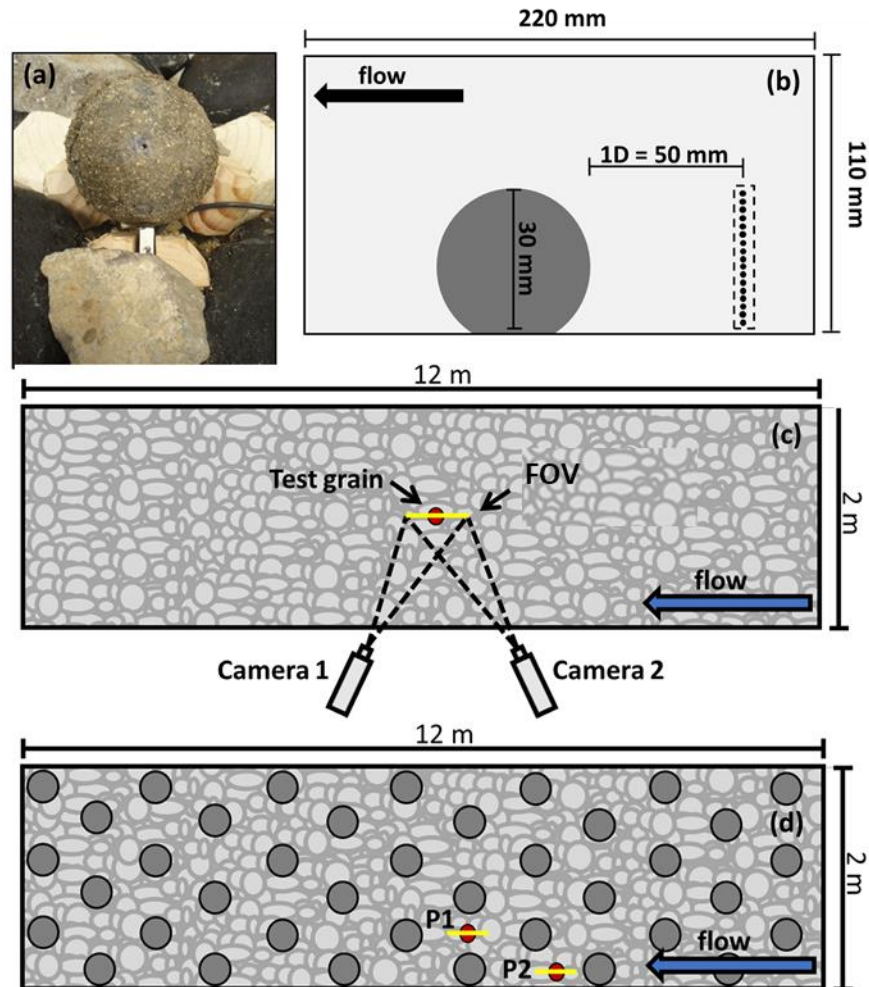
Figure 2.1 The mobile test grain, SPIV measurements, and bed configurations. (a) The mobile test grain is shown on its stand and photographed such that the flow direction goes into the image. (b)SPIV was collected in a streamwise oriented field of view (FOV), and a velocity profile was extracted from the bed surface to the height of the test grain. Bed configurations are shown for (c) the fixed cobble bed where the test grain was placed in the center of the test section longitudinally and cross sectionally, and (d) the cobble bed with boulders added in a staggered configuration where the test grain was placed in two positions within the bed: P1 was equidistant from all neighboring boulders and P2 was immediately downstream of a boulder. To collect SPIV for P1, the cameras were placed so that the boulders were not obstructing the camera view, while for P2, we used only a single camera focused on the test grain from upstream of the test grain to obtain 2D velocities in the streamwise and vertical directions.

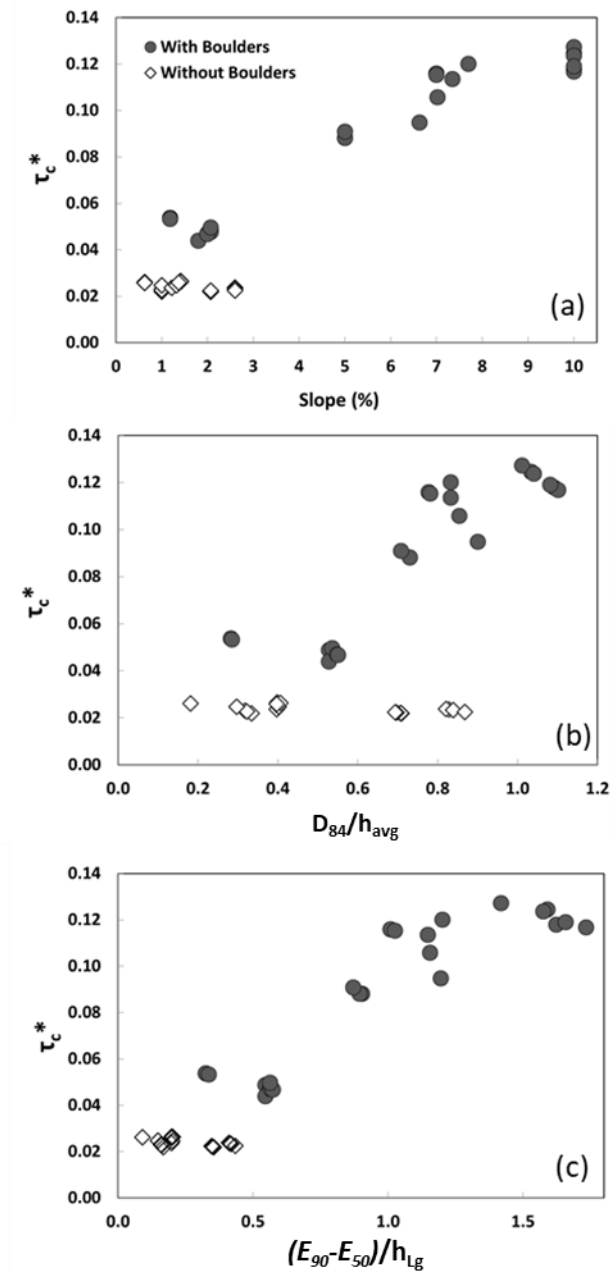*Figure 2.2 Critical Shields stress as a function of (a) percent slope, (b) relative roughness, and (c) protrusion relative roughness.*
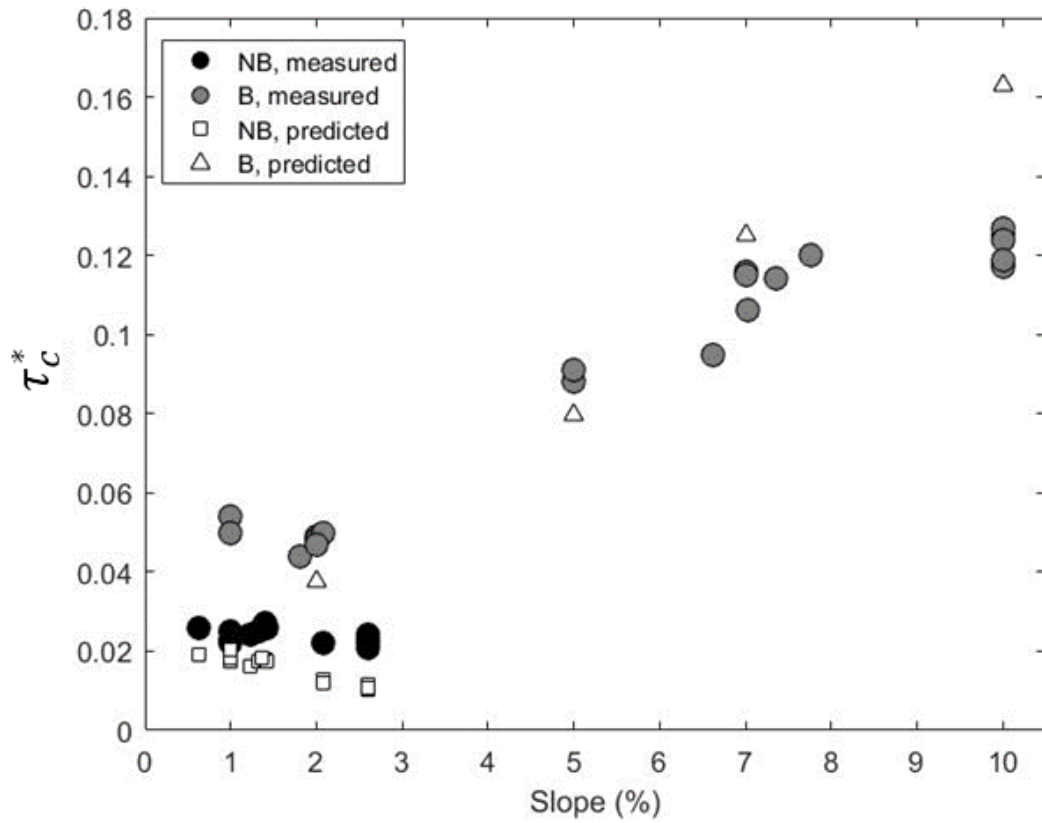
Figure 2.3 Critical Shield stress calculations for boulders (B) and no boulder runs (NB), using measured dimensionless mean velocities and turbulence intensities in equation 3 (white symbols). Measured critical Shields stresses (black and grey symbols) are shown for comparison.

Figure 2.4 Predicted (grey symbols) and measured (black symbols) critical Shields stresses are shown as functions of bed slope. Predictions use the measured dimensionless mean velocities but exclude any turbulence intensities for both runs without boulders (NB) and boulder (B) runs.

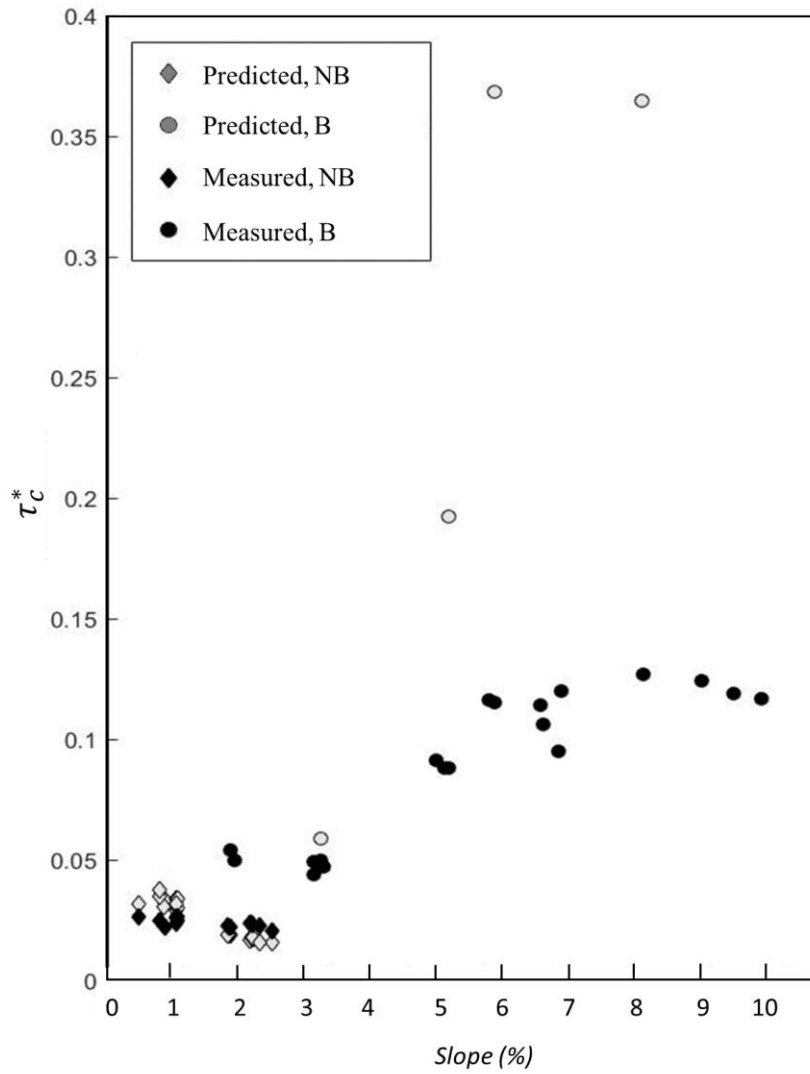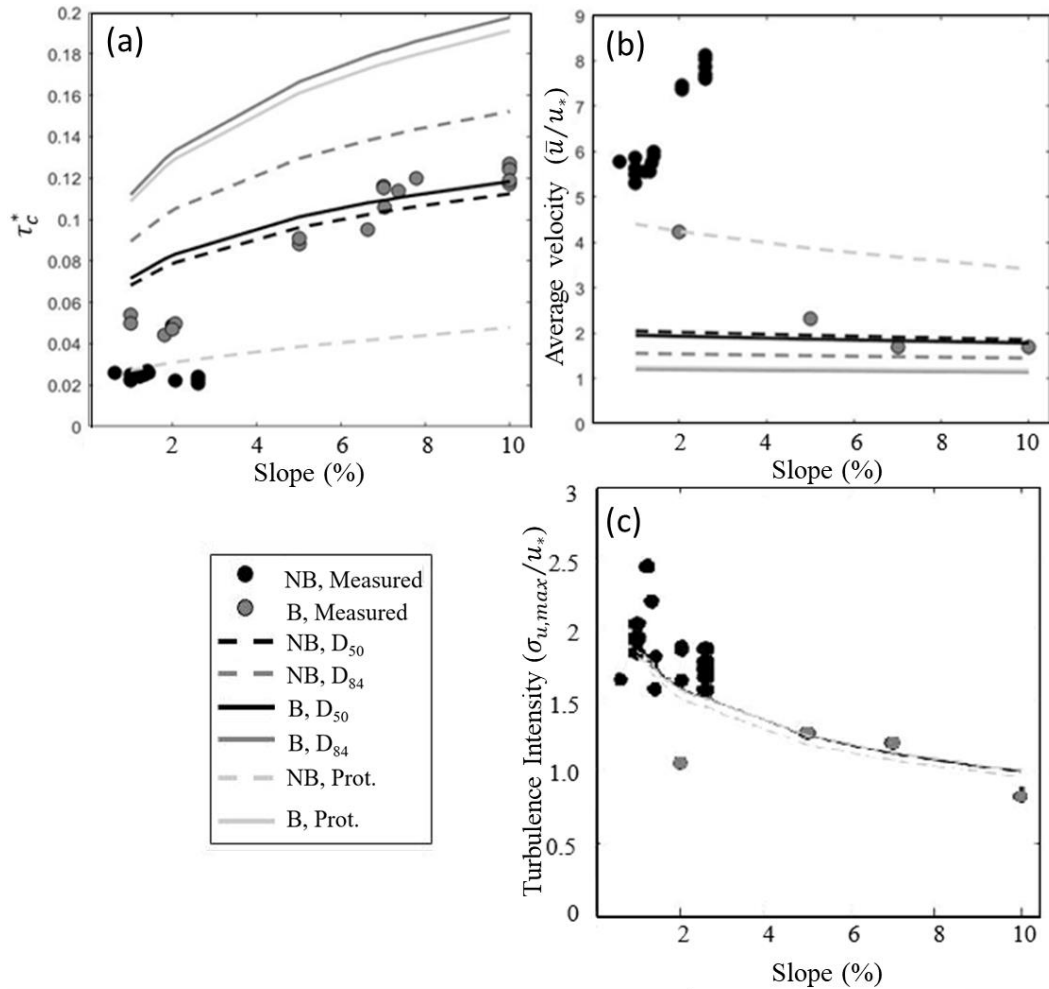*Figure 2.5 Measured (black and grey) and predicted(lines) (a) critical Shield stress and near-bed dimensionless (b) average velocity, and (c) turbulence intensities as functions of bed slope. We used three different roughness definitions k_{sm} to calculate dimensionless average velocities and turbulence intensities, one each based on the bed D_{50}, D_{84}, and protrusion of large grains (labeled Prot, using E_{90}-E_{50}). For each roughness definition, there were two definitions of k_{sm} depending on the underlying bed material: boulder and cobbles (B), and with no boulders (NB). Each prediction has a different line named with the bed material followed by the k_{sm} definition used (see Table 1).*
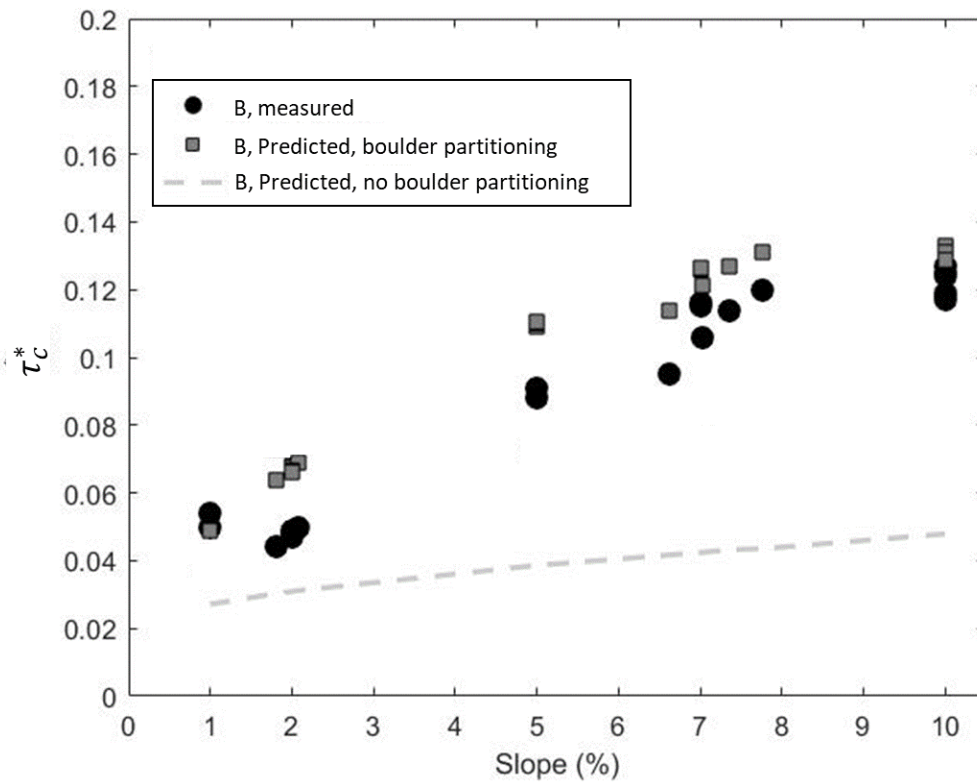
Figure 2.6 Measured (black circles) and predicted critical Shield stresses as functions of slope for the boulder runs. Predictions used $k_{sm} = E_{90}\text{-}E_{50}(NB)$ (see Table 1) with (NB, grey squares) and without (dashed line) stress-partitioning calculations in equation (3).

Table 2.1 Roughness lengths (k_{sm}) used for critical Shield stress predictions. Two bed configurations representative of the experiments with no boulders (NB) and with boulders (B) were used. See text for symbol definition.

	Bed configuration	Percentile used	Length distribution	Roughness Length, k_{sm} (cm)
1	B	D_{50}	Grain size	6.5
2	NB	D_{50}	Grain size	6.2
3	B	D_{84}	Grain size	10.6
4	NB	D_{84}	Grain size	8.2
5	B	E_{90}-E_{50}	Elevation	13.1
6	NB	E_{90}-E_{50}	Elevation	2.4

Chapter 3: Local effects on grain motion in a steep, boulder bed stream

Abstract

The critical Shield stress is the dimensionless critical shear stress, which is the shear stress needed to start sediment motion in rivers. The critical Shields stress variation with grain size can be predicted using hiding functions, which describe how the mobility of a given grain size (D_i) is affected by the underlying grain size distribution (e.g. median grain size, D_{50}). The effects of sediment patches (bed areas with distinct grain size distribution) on grain relative mobility are largely unknown but could be important because patches may affect hiding effects by altering grain-scale parameters such as protrusion (distance a grain extends above the bed) and friction angle (angle through which a grain rotates). We explore the effects of patches on critical Shields stresses by developing hiding functions for different patch types within the Erlenbach torrent (Switzerland). To determine hiding functions for each patch type, we used: (i) mobile tracer grain sizes from each patch type for 10 storm events, and (ii) the median local shear stress on each patch type for each storm peak discharge, which were modeled using the quasi-3D FaSTMECH model. Hiding functions for all patch types overlapped, which indicated that each relative grain size (D_i/D_{50}) between patch type has similar associated critical Shields stresses. However, the critical Shields stress for a grain size (D_i) between patch types will vary, suggesting the mobility for a grain size (D_i) varies depending on the patch type it is located. We also measured in-situ protrusions and calculated friction angles for all grain sizes present on each patch type. Protrusion increased with grain size, and for a given grain size was higher on finer patches. However, all patches had about the same relation between relative grain size (D_i/D_{50}) and dimensionless values of protrusion (protrusion/grain c axis) and friction angle. Thus, the same relative grain size between patches will have roughly the same critical Shields stress based on having roughly the same protrusion and friction angle. This result indicates separately that the collapse of patch-level hiding functions onto the same relation should occur. Also, the mobility of each grain size (D_i) in different patch types vary due to underlying grain size (D_{50}).

Introduction

Projects such as river restoration and design of bridges and channel bank reinforcements rely on accurate estimates of the flows that move sediment (Skidmore et al. 2001; Malakoff et al., 2004; Palmer et al., 2005). Despite nearly a century of studies on the onset of grain motion, at least an order of magnitude error exist when predicting the onset of motion (Bathurst et al., 1987; Rickenmann,

1997; D'Agostino and Lenzi, 1999). A persistent issue in sediment motion predictions is the difficulty in accurately modeling the local grain scale effects that determine when a particle will actually move.

At the grain scale, the onset of motion occurs when the stabilizing force that is a function of grain weight and friction angle (the angle through which a grain must pivot) is exceeded by the driving forces of drag and lift (Wiberg and Smith, 1987). In natural stream beds, the heterogeneous arrangement of sediment creates a distribution of possible surface positions for each grain size, which influence friction angle and protrusion (vertical distance a grain extends above surrounding bed sediment). Friction angles have been measured by tilting a glued bed surface until a test grain, placed on the surface, rotates from its pocket (Kirchner et al., 1990; Buffington et al., 1992) or by pushing on a grain with a load cell to measure resisting forces and then back calculating the angle (Johnston et al., 1998; Buxton et al., 2015; Prancevic and Lamb 2015; Yager et al., 2018). Larger friction angles are associated with greater resisting forces that impede grain motion. The distribution of friction angles for a given grain size (D_i) can be predicted as a function of the ratio of D_i to the median grain size (D_{50}) and grain size distribution sorting (Kirchner et al., 1990; Buffington et al., 1991). Both driving and resisting forces acting on particles are also functions of grain protrusion (Wiberg and Smith, 1987; Yager et al., 2018). Grains with high protrusion experience large drag forces whereas those with low protrusion may have high lift forces (Schmeeckle et al., 2007). Protrusions of spheres (Kirchner et al., 1990) and naturally shaped grains have been previously measured on water-worked bed surfaces in experiments and in the field (Yager et al. 2018; Voepel et al., 2019). Larger protrusions may correspond with larger grain sizes (Kirchner et al., 1990), but generally no applicable predictive relation exists for protrusion as a function of grain size. However, it is not known what measure of protrusion is the most relevant to model local forces used in predicting the onset of motion. For example, protrusion could be defined as the grain height relative to the elevation of the immediate upstream grain, or to an upstream elevation farther from the particle of interest (Kirchner et al., 1990).

Grain positioning on channel beds (e.g. friction angles and protrusions) are most often ignored and instead the average shear stress that mobilizes a certain grain size are related. The dimensionless reach averaged shear stress responsible for grain motion is calculated with the critical Shields stress ($\tau_{c_i}^*$), which is

$$\tau_{c_i}^* = \frac{\tau_{ci}}{(\rho_s - \rho_w)gD_i},$$

(1)

where τ_{ci} is the critical shear stress required to move D_i, g is acceleration due to gravity, and ρ_s and ρ_w are the densities of sediment and water, respectively. The critical Shields stress for the bed median grain size (D_{50}) is approximately constant for gravel-bedded rivers, such that greater critical shear stresses are required to move larger median grain sizes (Shields, 1936). For heterogeneous mixtures of sediment, the critical Shields stress often varies with D_i. The relative mobility of each grain size can be calculated with hiding functions, which have the form:

$$\tau_{c_i}^* = a \left(\frac{D_i}{D_{50}}\right)^{-\gamma},$$ (2)

where γ and a are empirically fit values, and $a = \tau_{c_{50}}^*$, which is the critical Shields stress for the D_{50}. Hiding functions represent the fact that small grains are often hidden (low protrusion, higher friction angle) within the matrix of the bed material and experience low velocities whereas larger grains extend higher in the flow. Thus, small grains within a wide mix of grain sizes have higher critical Shields stresses than estimated with their weight alone, whereas coarser grains become more mobile relative to their weight. The exponent of the hiding function could range in theory between -1 (all grains sizes are equally mobile; hiding effects counteract weight effects) and 0 (only weight effects). Hiding functions suggest that the mobility of a given grain size and depends on the grain size of underlying bed.

Hiding effects for each grain size (D_i) are determined by grain size distribution, which varies spatially in natural channels. Grains are organized into patches, where the borders of each patch can be visually defined by a distinct change in grain size distribution compared to adjacent patches (Buffington and Montgomery, 1999; Dietrich et al., 2007; Yager et al., 2012; Monsalve et al., 2016). Some research has shown that the relative mobility of a given grain size changes between patch type. For example, researchers have observed that small grains may preferentially move from fine patches at lower flows, based on measured grain size distributions of bedload (Lisle et al., 1995; Vericat et al., 2008). Also, the relative mobility of grains has been predicted using varied bed arrangements that have different median grain sizes (Kirchner et al., 1990). This change in the mobility of a given grain size by patch type could be driven by the local grain arrangement as well as flow conditions that are dictated by each patch. For example, small grains on fine patches could have high protrusions and low friction angles, whereas on coarse patches, small grains would have low protrusion and high friction angles. In addition, a wide range of near bed shear stresses can exist between patches (Ferguson, 2003), but only one study has demonstrated a potential correlation between patch grain size and shear stress (Monsalve et al., 2016), which could also affect the relative mobility of a given grain size. For example, for a given flow stage, coarser patches could systematically be subjected to

higher near bed stresses increasing local grain mobility. However, the same tracer size on different patch types has been observed to move at the same flow magnitude (Dietrich et al., 2005; Yager et al., 2012), suggesting that the variation in protrusion and friction angle for D_i between patches are insignificant to affect sediment motion. Therefore although variations in grain size distributions between patch types may affect the protrusion, friction angle, and critical Shields stress for a given grain size, little research has been completed that quantifies the (i) variations of protrusion and friction angle between patch types, (ii) local shear stresses on patches, and (iii) relative mobility of each grain size within each patch type. It is therefore unknown if different hiding functions would also be needed for each patch type.

Here, by monitoring the motion of tracer grains from three patch types for a range of flow discharges in a steep, step-pool channel, we seek to understand how the relative mobility of a given grain size varies between patch types. It is well documented that grain mobility is affected by local protrusion, but it is unknown how protrusion variability between patch types affects sediment motion in natural rivers. We also measured in-situ measurements of protrusions and calculated median friction angles for installed tracer grains on each patch type. To explore patch effects, we developed hiding functions for each patch type, by using patch-scale shear stresses that occurred at peak discharges per tracer-mobilizing storm event, which were estimated with a quasi-3D model (Monsalve et al., 2016). Finally, the most relevant measurement of local grain protrusion for the onset of motion is not known. Thus, we also measured protrusions at multiple scales to explore how protrusion estimates change with distance away from the particle of interest.

Methods

Study site

We conducted our field work at the Erlenbach torrent (Brunni, Switzerland), which is managed by the Swiss Federal Research Institute WSL. This site was selected because it is characterized by wide-ranging and frequent sediment-transport events. Additionally, the WSL measures discharge at the downstream boundary of the experimental reach every 10 minutes during flow events using a well-established stage-discharge relationship combined with stage measurements in a fixed cement cross-section. The study reach is 50 meters long, 4.7 m wide, steep (10% reach-averaged slope) and is characterized by boulders steps that remain emergent at lower flow events, become submerged at higher flows, and are rearranged very infrequently. The channel walls were previously reinforced with boulders and cement to maintain a general channel direction, however the thalweg freely changes paths.

Defining patches

To characterize the spatial variability of grain size distributions within our reach, we created a map of the bed where each patch was defined visually, and followed methods outlined by Yager et al. (2012) and Monsalve et al. (2016). Individual patches were identified by finding an area with a spatially constant grain size distribution, and patch boundaries were characterized by a clear change in grain distribution (Buffington and Montgomery 1999a). The patch type was selected by visually estimating the most prevalent grain size class that occupied the patch and then noting all other grain size classes that composed at least 5% of the patch following Buffington and Montgomery (1999) (e.g. cG patch was predominately gravel, with some cobble). The patch type was amended based on pebble counts if the patch was actually occupied by different grain size classes (see grain size distribution section below). The patch map and detailed grain size distribution for each patch type can be found in Monsalve et al. (2016).

Grain size distributions

To characterize the grain size distribution for each patch type, we conducted pebble counts on multiple patches within each patch type until a representative sample (>100 grains) was collected (Wolman et al., 1954). We used a grid to sample particles with the spacing being greater than the largest grain size on the patch, to avoid resampling the largest grain. We blindly selected the grain at each grid cell to ensure an objective grain selection. Grain sizes were measured in half-phi intervals using a gravelometer. Further details on the pebble counts can be found in Monsalve et al. (2016).

Tracer particles

We collected the potential tracer stones immediately upstream of our study reach to avoid disturbing our site, and we sorted the stones into half phi size classes (11mm to 128 mm) using a gravelometer. Grains 32 mm and larger were implanted with a radio-frequency identification (RFID) tag, which was placed into a cavity made with a drill press and fixed in place using epoxy (Lamarre et al., 2005; Schneider et al., 2014). Then, each grain size class was painted a unique color, and each grain was uniquely identified by a written number on the grain surface. Also, the primary three axes and weights were measured for each tracer. Grains smaller than 32 mm were also painted based on their phi size class, and then identified uniquely with a written number on the grain surface.

To optimally characterize the most common patch types of the potentially mobile portion of the bed (Yager et al., 2007; Monsalve et al, 2016), we populated Gravel, cobble-Gravel and gravel-Cobble patches with tracer particles (hereafter referred to as fully-populated patches). We matched

the installed tracer grain size distribution to that of each underlying patch. By placing a consistent density of tracer grains (20 grains/m^2 of bed surface), we avoided overpopulating a certain patch. With the dual purpose of placing tracer stones in natural positions and avoiding changing the patch grain size distribution, we removed in-situ grains in random locations and replaced them with tracers in the same approximate position and orientation. We also only placed larger tracer grain sizes (90 and 128 mm) in some patches that were always submerged to ensure that we observed entrainment of large grains, thus these patches were not populated with a full distribution of grain sizes. Also, when tracers moved out of the fully populated patches, they often deposited on continually submerged patches (hereafter defined as Submerged Patches). The placed tracers were likely less stable than fluvially deposited grains, which would cause tracer grains to move at lower peak discharges than naturally deposited grains. We did not eliminate the first movement of tracer grains because our sample size of mobile grains would be too low.

After each storm event, we located tracers (recovery rate for all grain size classes ranged from 20%-94%) using one of three methods to identify location coordinates of the tracers depending on the availability of equipment and the time between storms. These methods were: 1) a total station survey, 2) the horizontal distances of the tracers from three surveyed and spray-painted fixed points, and 3) photographs taken parallel to the bed (plan view) to visualize tracer grains and surveyed fixed points. Coordinates for tracers using Method 2 were identified by making a circle centered on each surveyed fixed point, with the radius set by the measured distance to the tracer. Then, we found the area of overlap for the three circles and the tracer was at the centroid of this overlapping area. Tracer coordinates were found using Method 3 by overlapping: i) two or more surveyed fixed points visually represented using their coordinates and ii) the fixed points in photographs where tracers were present. This process scaled and oriented the photographs with the fixed-point coordinate systems, such that the coordinates of each tracer could be identified.

Using these known tracer coordinates (methods 1-3) before and after each event, we determined that a tracer grain moved in an event if its calculated transport distance was greater than the largest error associated with all three methods. The total station method was assumed to have a relatively low error. We therefore measured a set of tracer grain locations with the total station that we had also located using methods two and three. The errors associated with the photograph and 3-point methods were separately calculated by finding, for each tracer location, the distance between the estimated and total station coordinates. For each method, using the distribution of error distances, we calculated the root mean squared error (RMSE, method 2 and 3 = 0.16m). Based on Yager et al. (2012), two times the RMSE resulted in a 95% confidence interval for tracer particle locations, which

would equal 0.32 m. However, within the photographs, we observed particular tracer grains to be stable between events, but this error distance incorrectly indicated that these tracer particles had moved. Thus, we increased the error distance to 0.5 m, such that the tracer grains that were estimated to move corresponded with the tracer grains that were observed to move. When a tracer grain had moved greater than 0.5 m, the peak discharge that occurred prior to relocating the grain was assumed to be the discharge responsible for motion.

Oftentimes, the smallest grains (less than 22.6 cm) were permanently lost in the flow event that occurred immediately after their placement. In this circumstance, we assumed that the tracer grain moved during the peak discharge in the event that occurred between the dates when it was placed and subsequently lost. If a tracer grain larger than 32 mm in diameter was permanently lost, it was assumed to have moved if the repeat photographs provided evidence that the grain was not buried in its original location (e.g. buried and then uncovered in the same location), and the event just prior to losing the grain was considered to have caused its motion.

Protrusion measurements

We measured protrusions for each grain size class (including tracer and in place grains) present in gravel, cobble-Gravel, and gravel-Cobble patches. We used a portable device that unobtrusively measured elevations from a set horizontal datum for the grain of interest and for upstream locations at a spacing of 1 cm, up to a total distance of 48 cm. Transects taken at horizontal angles of 45° from the upstream direction and transects taken in a direction immediately upstream from the grain of interest were similar, thus we collected upstream protrusion transects only parallel to the overall channel direction. For each grain size class and patch type combination, we collected transects for multiple grains to include a range of grain placements within each patch type (transect number per grain size in each patch in Table 1). We collected a variable number of protrusion samples with patch coarseness, however the larger sample size for coarser patches was to capture the greater variability of elevations present. For each transect, we then calculated: (a) an immediate upstream grain protrusion by using the difference in elevation between each grain of interest and the immediate upstream bed elevation, and (b) a near-proximity upstream grain protrusion that used the difference between the grain of interest elevation and the median of the elevations measured up to 48 cm upstream. For both of these methods to calculate protrusions, and for each grain size (D_i) and patch type combination, we calculated the median protrusion. Thus, hereafter, the median protrusion refers to the median of each grain size and patch type combination rather than the protrusion calculated for a given transect using the median of upstream elevations. Additionally, we tested the influence of incrementally adding more upstream elevation measurements in the calculation of the

median protrusion for each transect. Negative protrusions represent grains that were below the elevation of the surrounding upstream bed, and positive protrusions were grains that were higher in elevation than the surrounding bed.

Modeling shear stresses during peak flow events

Local shear stress distributions vary with patch type (Monsalve et al., 2016). Thus, we used local shear stresses for each patch type, rather than assuming a reach-averaged shear stress that is often used in hiding functions. We used the quasi-3D hydrodynamic model, FaSTMECH (Flow and Sediment Transport and Morphological Evolution of Channels, McDonald et al., 2001, 2005) to obtain the spatial distribution of shear stresses within our study reach. The model, developed by the USGS and distributed by the International River Interface Cooperative (iRIC, www.i-ric.org), solves the vertically averaged conservation of mass and Reynolds-averaged momentum equations in an orthogonal curvilinear coordinate system (Nelson and Smith, 1989). The depth-averaged solutions are based on an assumption of steady and hydrostatic flow. Turbulence effects are simplified assuming homogeneous and isotropic characteristics and modeled using a zero-equation model for the lateral eddy viscosity (Miller and Cluer, 1998; Nelson et al., 2003; Barton et al., 2005). Approximated vertical velocity profiles are based on the two-dimensional (2D) solutions and the turbulence closure model (Rattray and Mitsuda, 1974). FaSTMECH has been widely used in field studies (e.g. Clayton and Pitlick, 2007; Nelson et al., 2010; Conner and Tonina, 2014; Maturana et al., 2014; Mueller and Pitlick, 2014; Segura and Pitlick, 2015; Monsalve et al., 2016) and specific details of the model can be found in Nelson and McDonald (1995).

We simulated the entire range of flows (0.20 to 2.1 m^3/s, increments of 0.05 m^3) that occurred while our tracer particles were installed. Individual flow scenarios were calibrated using depth-discharge rating curves that were developed from field measurements taken at five cross-sections (average coefficient of determination (R^2) was 0.84). Additional details on flow measurements and model calibration can be found in Monsalve et al. (2016). The model used two parameters for calibration, the lateral eddy viscosity and the bed surface roughness. We set the lateral eddy viscosity to 0.005 m^2/s for all our simulated discharges and varied the bed surface roughness using a drag coefficient (C_d) to obtain a good agreement between observed and predicted flow depths. We analyzed two approaches to specify C_d in our simulations, a spatially variable or constant drag coefficient. A drag coefficient that varies spatially represent the conditions in which the flow rapidly responds to variations in grain size, therefore C_d, flow depth, and velocity adjust locally to account for this change in roughness. On the other hand, a spatially constant drag coefficient characterizes the

case in which the flow responds extremely slowly to changes in roughness (Lisle et al., 2000), consequently, the effects of roughness are averaged by the flow over spatial scales larger than that the roughness source. In our case, the best results were obtained using a spatially constant drag coefficient that inversely varied with discharge (C_d range of 0.12–0.26) (See Monsalve et al., 2016).

We computed the local shear stress (τ_n) directly in FaSTMECH at every node of our mesh (10 x 10 cm cell size). Estimates are based on the 2D velocity solutions according to:

$$\tau_n = \rho C_d \left(u_n^2 + v_n^2 \right)$$

(3)

where the subscript n indicates a given node, and u_n and v_n are the vertically averaged streamwise and cross-stream velocities, respectively. We analyzed the sensitivity of our τ_n estimates to the choice of C_d. Similar to what previous studies have shown (e.g. Lisle et al. 2000; Nelson et al. 2010; Segura and Pitlick 2015; Monsalve et al. 2016) the use of a constant drag coefficient resulted in similar τ_n predictions compared to those determined using a spatially variable drag coefficient. This occurs because a trade-off exists between the local drag coefficient and velocity values (low or high local C_d resulting in high or low local velocity, respectively).

Hiding functions

We developed a hiding function for each patch type (G, cG, and gC) and for all three of these patch types combined. Hiding functions require a critical Shields stress that is associated with the motion of a given grain size. We used shear stresses from the quasi 3D FaSTMECH model to obtain a distribution of shear stress on each patch type and then used the median shear stress for each event peak discharge in the hiding functions. Normally, the critical Shields stress using tracer studies is defined using the maximum mobile tracer size for the peak shear stress in a flow hydrograph. Given uncertainties in the maximum mobile tracer size, we instead used the D_{84} of the mobile tracer grain size distribution (Table 2). A considerable error in the mobile D_{84} may exist for some flow events and patch types because of a small number of observed mobile tracer grains. Tracers moved from patches with a full grain size distribution of installed tracers, as well as from patches that had as few as a single tracer that had been transported there from a previous storm event. We produced two sets of hiding functions for each patch type using i) the D_{84} of mobile tracers and median shear stresses on only fully populated patches that had mobile tracers in a given event, and ii) the D_{84} of mobile tracers and median shear stresses associated with any patches that had a mobile tracer in a given event.

Friction angles

We could not measure friction angles without disturbing the grains on the bed, and we instead chose to use (Buffington et al, 1992)

$$\emptyset_n = (25 + 0.57n)(D_i/K_{50})^{-(0.16+0.0016n)}(\sigma)^{-(0.21+0.0027n)} \qquad (4)$$

which calculates a distribution of friction angles (ϕ_n) for D_i relative to D_{50} and is also a function of grain sorting (σ). We used equation 4 by calculating the median friction angle for each D_i on each patch type using the patch median grain size.

Results

Local grain protrusion measurements

Protrusion –averaging transect length (immediate upstream vs. near-proximity) affected the median protrusion measured for each grain size and patch type combination (Figure 3.1). Similarities between immediate upstream and near-proximity protrusion were that: i) particles protruded more as the grain size of interest increased, ii) coarse grains had lower median protrusion with patch coarsening, and iii) for gravel patches, the median protrusion was positive for all grain sizes. Three major differences between these two methods of defining protrusion occurred. First, greater median protrusion differences for a given grain size generally occurred between different patch types when using the near-proximity protrusion. Second, for the smallest grains in cG and gC patches, the median immediate upstream protrusion was near zero, whereas the median near-proximity protrusion was negative. Third, a greater number of grain size classes have negative median protrusions on cG and gC patches for the near proximity than the immediate upstream protrusion.

Protrusion transect length

For all transect lengths, all grain sizes had lower median protrusions in coarser patches, and coarser grains generally had higher protrusions than finer grains regardless of patch type (Figure 3.2). For grain sizes larger than the patch D_{50} (G: 20 mm, cG: 50 mm, gC: 57 mm), the median protrusion estimates were generally independent of transect length; protrusions measured at 2 cm away from the particle of interest were roughly equal to those for the entire transect. Also, the relative magnitudes of median protrusions between different grain sizes were the same regardless of transect length. The median protrusions of grain sizes that were smaller than the patch D_{50}, however, often decreased with greater transect length, and the relative protrusion magnitudes between these grain sizes also changed with transect length. The protrusion estimates for grain sizes less than 20 mm in G patches increase

with longer transect length, and the protrusion estimates for grains finer than 50 mm and 57 mm for cG and gC patches, respectively, decrease with greater transect length.

Normalizing grain size and protrusion

We developed dimensionless grain sizes (from Figure 3.1) by normalizing each grain size (D_i) by the D_{50} of each patch type. We also calculated dimensionless protrusion by dividing the measured protrusion for each grain by its 1) grain size (i.e. b-axis) (Figure 3.3 a and b) and 2) measured c-axis, which we assumed is the grain axis that sits vertically on the bed (Figure 3.3 c and d). We then calculated the median dimensionless protrusion for a given patch type and grain size bin. The median dimensionless protrusion increased with dimensionless grain size regardless of how dimensionless protrusion is calculated. For all patch types, the relations between dimensionless median protrusion and dimensionless grain size also generally collapsed on a single logarithmic line. This suggests that protrusion is dominantly controlled by the size of a grain relative to that of the underlying bed. The highest R^2 of all possible dimensionless protrusion vs. D_i/D_{50} relations occurred for the near-proximity protrusions when the protrusion was normalized with the c-axis. Although patch specific effects (e.g. standard deviation of grain size distribution) may contribute to scatter around the single logarithmic line, these effects do not seem to dominantly control protrusion. Median protrusions may be estimated using the equations in Figure 3.3, combined with measured grain size distributions for each patch type. To estimate c axes, a grain shape would need to be assumed or the c-axis would need to be measured.

Hiding functions

The exponent of the hiding functions for each patch type was between 0.7 and 0.9 which occurred for both methods of grouping patches (fully populated patches vs. all mobile patches). The hiding function for each patch type had better R^2 values when using the fully populated patches instead of all mobile patches. Yet, when we combined all patch types together into a single hiding function, use of all mobile patches resulted in a higher R^2 value than that obtained when using only the fully populated patches. Regardless of the method used (fully populated vs all mobile patches) 1) the $\tau^*_{c_{50}}$ values were similar between cG and gC patches, 2) for a given patch type (cG or gC), $\tau^*_{c_{50}}$ were similar, 3) gravel patch hiding functions had higher $\tau^*_{c_{50}}$ values than the cG, gC, and patch-combined hiding functions. The exponents of the hiding functions did not systematically change with patch coarsening.

Discussion

How do our patch combined hiding functions compare to those in past studies?

For the all patch types combined hiding functions using tracers: i) only on fully populated patches, we obtained a $\tau_{c_{50}}^*$ of 0.17 and a γ of 0.86 and ii) on all mobile patches, we obtained a $\tau_{c_{50}}^*$ of 0.14 and a γ of 0.8. When comparing hiding functions, it is important to consider that critical Shields stresses for the median grain size ($\tau_{c_{50}}^*$) increase with greater reach-averaged bed slopes (Smith and Yager [in progress], Lamb et al., 2008, Buffington et al., 1997). Hiding function exponents (γ) have yet to be correlated with reach-averaged channel slope but show considerable variability even in lower-gradient channels. Previously developed hiding functions suggest varying degrees of grain size selectivity in beds with heterogeneous-sized grains. Hiding functions have sometimes indicated sediment entrainment to be close to equal mobility (γ = -1) (Parker et al., 1982; Andrews 1983), where exposure effects increase the mobility of large grains, and hiding effects decrease the mobility of smaller grains. Other studies have observed size-selective transport (Ashworth and Ferguson, 1989), where γ is greater than -1. Our γ are within the range of values reported for lower gradient channels and although many are close to -1, they indicate that size-selective transport is occurring on potentially mobile patches. The hiding function exponents in previous studies on steep channels were -0.85 (Schneider et al., 2015), -0.79 to -0.57 (Mao et al., 2008), -0.62 (using a total shear stress) and -0.16 (using stress on the mobile fraction) (Yager et al., 2012). Our γ values were within the lower range of values in these other studies. We will now discuss how our hiding function coefficients compare to those developed in steep channels.

Hiding functions developed in steep streams have a range of $\tau_{c_{50}}^*$, and were reported as: 0.06 using a reduced energy slope to calculate reach-averaged shear stress (Schneider et al., 2015), 0.19-0.29 incorporating flow resistance (Mao et al., 2008), and 0.14 and 0.07 using the total reach-averaged shear stress and a mobile bed stress that removed boulder borne stresses, respectively (Yager et al., 2012). Our $\tau_{c_{50}}^*$ had magnitudes similar to those when the total shear stress was used, which does not account for large roughness effects of boulders and steps. We observed a higher $\tau_{c_{50}}^*$ compared to studies that account for stresses born by immobile boulders, which suggests that our applied stresses were relatively high even though we used local applied stresses by mobile patch type. We had expected that our $\tau_{c_{50}}^*$ would instead be lower because we had also indirectly accounted for the effects of large roughness elements in the bed topography used in the 2D model. Our high $\tau_{c_{50}}^*$ may suggest that our median shear stress estimates at the patch scale may still indirectly include some large shear stresses that the bed sediment on the patch does not actually experience. Another possible

explanation for these high $\tau^*_{c_{50}}$ values is that the 2D model may not always accurately depict the highly 3D flow that occurs in the Erlenbach, and therefore may over-estimate the median shear stresses on the patches (see below for discussion on this topic). The difference in our $\tau^*_{c_{50}}$ values compared to other studies could also be caused by the methodology used in the determining the mobile D_i for each peak flow discharge.

Variability of hiding functions between patch types

We investigated whether the effects of the underlying grain distributions within each patch type impacts the degree of size-selective entrainment and overall sediment mobility ($\tau^*_{c_{50}}$). Aside from G patches, differences in hiding functions between patch types are likely within methodological errors. For example, for a given patch type, the differences in γ between our two grouping methods (all mobile patches vs. only populated patches) were larger than the variability in γ between patch types for a given method (Figure 3.4). This implies that the different hiding functions developed for cG, gC, and all patches combined are likely all within methodological uncertainties and are therefore not different.

The G patches had similar γ but much higher $\tau^*_{c_{50}}$ (Figure 3.4 a and b) than did the gC and cG patches and this caused the hiding function for the G patches to not collapse onto the same general relation as the other patches. To investigate this result, we tested two possible explanations. First, we considered that the shear stresses on G patches could have been very high such that the maximum grain size on the patch moved even at relatively low flows; any increases in shear stresses at higher flow discharges would not increase the mobile D_{84}. Thus, the shear stresses that we used at higher discharges were not technically critical shear stresses for the recorded mobile D_{84} but were critical shear stresses for larger grains, which were not present on the patch. This would cause the critical Shields stress to be artificially high on G patches. However, for most events many tracer grains were not moving on G patches (Table 2), which suggests that G patches were not very mobile. Conversely, the D84 of the mobile tracer sizes for all events combined was larger than the patch D_{84} (41 mm) (Figure 3.5). This could imply that the maximum patch grain size did move, and likely did so at larger discharge events. Thus, the critical shear stresses used in the hiding function may have been for a larger grain size than the mobile D_{84}. However, shear stresses during lower magnitude flows likely did not exceed those necessary to move most grain sizes on the patch and this first hypothesis is likely largely incorrect. The very low number of mobile tracers on G patches also gave considerable uncertainty in the mobile D_{84} for most events. We further eliminated the possibility that the mobile D_{84} used in the hiding function calculations was too small by artificially increasing the mobile grain

size for all events to the maximum grain size present in the G patches. This resulted multiple $\tau^*_{c_i}$ for a single relative grain size ($D_i/D_{50} = 4.5$), and therefore a hiding function could not be created. However, these $\tau^*_{c_i}$ values were still higher (0.09) than those in the other patches for a D_i/D_{50} of 4.5

Another explanation for the high $\tau^*_{c_{50}}$ in G patches is that the 2D model incorrectly calculated high velocities and shear stresses on many of the gravel patches. The gravel patches with mobile tracers were often immediately downstream of boulders, where the modeled 2D estimates of flow will likely have large errors because of plunging flow over boulders and flow recirculation downstream of the boulders (Monsalve et al., 2016). To explore if the modeled shear stresses in these specified G patches could be incorrect, we calculated the median shear stresses for each patch type for three groups of patches: 1) all patches with mobile tracers, 2) all fully populate patches with mobile tracers, and 3) all submerged patches regardless of whether they had installed or mobile tracers (Figure 6). For a given flow discharge, the median shear stresses for all mobile and fully populated G patches were much higher than the median shear stresses of all submerged G patches (Figure 3.6). This implies that the G patches with mobile tracers may not be representative of all submerged G patches and could have artificially high shear stresses because the 2D model did not account for the highly 3D flow in these locations. For each of the cG and gC patches, these three different median shear stress estimates were largely in the same range of values for a given discharge (Figure 3.6), implying that the cG and gC patches with mobile tracers were representative of all submerged patches of these types. We used the median shear stresses for all submerged G patches in the G hiding function calculation to test whether incorrect shear stresses on mobile G patches could explain the high $\tau^*_{c_{50}}$ of G patches. Now the G patch hiding function overlapped with the cG an gC patch hiding functions (Figure 3.7), which implies that the G patches could have similar hiding functions as the other patches if shear stresses on the G patches with mobile tracers were accurate.

Protrusion measurements and patch effects

Protrusion measurements suggest that coarser grains emerge more from the bed surface than finer grains, and that all grain sizes protrude higher in finer patches (Figure 3.1). We also found that for a given grain size as patches coarsen, the calculated friction angle increases, and the friction angle is also greater with smaller grain sizes on a given patch type (Figure 3.8). Our protrusion and friction angle results imply that hiding effects vary between patch types. Interestingly, dimensionless protrusion (Figure 3.3) and friction angle (Figure 3.8) each largely collapse onto a single relation with D_i/D_{50} for all patch types. This suggests that patch-scale effects on protrusion and friction angle are largely through the scaling of the grain size of interest (D_i) to the underlying grain size of the patch

(D_{50}). Grains that have the same D_i/D_{50}, but that are located on different patches, will generally have the same protrusion and possibly similar friction angles. However, a given grain size (D_i) will have a lower protrusion and a higher friction angle on a coarser patch than a finer patch. Complete overlap of the calculated frictions angles between patch types did not occur because Buffington et al.'s (1991) equation also incorporates the effects of bed grain size sorting. Sorting effects could also possibly explain the scatter around the fit logarithmic line (Figure 3.3).

Implications for hiding functions

Protrusion and friction angle are two grain-scale characteristics that can mechanistically explain variations in critical Shields stresses and hiding effects. The collapse of dimensionless protrusion and friction angle each onto a single relation with D_i/D_{50}, implies that one dimensionless protrusion and friction angle combination will result for a certain value of D_i/D_{50}. Therefore, the same critical Shields stress will likely occur on different patch types for the same D_i/D_{50}. This result separately implies that the collapse of the patch-type hiding functions onto a single line should occur. Our results also suggest that variations in patch-scale grain size distributions are important for hiding effects because each grain size will be surrounded by a different patch D_{50}, which will result in unique protrusion, friction angles, and critical Shields stress estimates for that grain size. Therefore, different patch-scale hiding functions are not needed, but rather one hiding function can be used as long as it is combined with the D_{50} of each patch type.

Which scale(s) of protrusion/hiding determine grain mobility?

Most streams are characterized by multiple distance scales from a particle that affect its protrusion: (i) the immediate upstream topography (smallest distance scale), (ii) near-proximity topography within a patch (intermediate distance scale), (iii) larger patch shape (flat, convex or concave), and (iv) for steep streams, the general elevation of an entire patch with respect to the nearest upstream boulder. We investigated the influence of scales i and ii on protrusion but it is still unclear which of these two scales should be used when calculating critical Shields stresses (e.g. in a force balance model).

When considering the forces that are applied to a grain, it seems prudent to consider upstream bed elevations beyond those immediately upstream of the grain. These elevations are likely to determine the velocities felt by the grain. However, protrusion estimates were mostly independent of transect length for grains larger than the patch median ($D_i>D_{50}$), which implies elevations immediate upstream of a grain may appropriately represent the upstream bed topography. The most relevant protrusion measurement for grains much smaller than the patch median size ($D_i<D_{50}$) is unknown

because the median measured protrusion decreased as more upstream elevations were incrementally included in the protrusion calculation (Figure 3.2).

Conclusion

Our results imply that different grain size distributions in patches affects the relative mobility of a given grain size but not the size-selective transport of different grain sizes. Hiding effects and critical Shields stresses are mechanistically controlled by grain protrusion and friction angle. Hiding functions between patch types roughly collapsed onto a single line, suggesting that the relative grain size determines the mobility of a grain. Each grain size, between patch types, will have a different associated underlying median grain size (D_{50}) thus, will have varied mobility. Also, between patch types, each grain size (D_i) will have variable relative grain size ratios (D_i/D_{50}), and thus unequal protrusion and friction angles, which implies that critical Shields stresses for that grain size will vary with patch type. We also concluded that for all patch types, the relations between relative grain size (D_i/D_{50}) and dimensionless values of protrusion and friction angle are approximately equal. To understand the grain scale mechanisms involved in the onset of sediment motion, further research needs to be completed that focuses on near-bed flow velocities that interact with grains with variable protrusions and friction angles on various patch types.

Literature Cited

Ashworth, P. J., & Ferguson, R. I. (1989). Size-selective entrainment of bed load in gravel bed streams. *Water Resources Research*, *25*(4), 627-634.

Barton, G. J., McDonald, R. R., Nelson, J. M., & Dinehart, R. L. (2005). *Simulation of flow and sediment mobility using a multidimensional flow model for the white sturgeon critical-habitat reach, Kootenai River near Bonners Ferry, Idaho* (No. 2005-5230).

Bathurst, J. C. (1987). Critical conditions for bed material movement in steep, boulder-bed streams. *International Association of Hydrological Sciences Publication*, *165*, 309-318.

Buffington, J. M., Dietrich, W. E., & Kirchner, J. W. (1992). Friction angle measurements on a naturally formed gravel streambed: Implications for critical boundary shear stress. *Water Resources Research*, *28*(2), 411-425.

Buffington, J. M., and D. R. Montgomery (1997), A systematic study of eight decades of incipient motion studies, with special reference to gravel- bedded rivers, Water Resour. Res., 33(8), 1993–2029.

Buffington, J. M., & Montgomery, D. R. (1999). A procedure for classifying textural facies in gravel-bed rivers. *Water Resources Research*, *35*(6), 1903-1914.

Buxton, T. H., Buffington, J. M., Yager, E. M., Hassan, M. A., & Fremier, A. K. (2015). The relative stability of salmon redds and unspawned streambeds. *Water Resources Research*, *51*(8), 6074-6092.

Clayton, J. A., & Pitlick, J. (2007). Spatial and temporal variations in bed load transport intensity in a gravel bed river bend. *Water Resources Research*, *43*(2).

Conner, J. T., & Tonina, D. (2014). Effect of cross-section interpolated bathymetry on 2D hydrodynamic model results in a large river. *Earth Surface Processes and Landforms*, *39*(4), 463-475.

Dietrich, W. E., Nelson, P. A., Yager, E., Venditti, J. G., Lamb, M. P., & Collins, L. (2005). Sediment patches, sediment supply, and channel morphology. *River Coastal and Estuarine Morphodynamics*, 79-90.

D'Agostino, V., & Lenzi, M. A. (1999). Bedload transport in the instrumented catchment of the Rio Cordon: Part II: Analysis of the bedload rate. *Catena*, *36*(3), 191-204.

Ferguson, R. I. (2003). The missing dimension: effects of lateral variation on 1-D calculations of fluvial bedload transport. *Geomorphology*, *56*(1-2), 1-14.

Johnston, C. E., Andrews, E. D., & Pitlick, J. (1998). In situ determination of particle friction angles of fluvial gravels. *Water Resources Research*, *34*(8), 2017-2030.

Kirchner, J. W., Dietrich, W. E., Iseya, F., & Ikeda, H. (1990). The variability of critical shear stress, friction angle, and grain protrusion in water-worked sediments. *Sedimentology*, *37*(4), 647-672.

Lamarre, H., MacVicar, B., & Roy, A. G. (2005). Using passive integrated transponder (PIT) tags to investigate sediment transport in gravel-bed rivers. *Journal of Sedimentary Research*, *75*(4), 736-741.

Lamb, M. P., Dietrich, W. E., & Venditti, J. G. (2008). Is the critical Shields stress for incipient sediment motion dependent on channel-bed slope?. *Journal of Geophysical Research: Earth Surface*, *113*(F2).

Legleiter, C. J., Phelps, T. L., & Wohl, E. E. (2007). Geostatistical analysis of the effects of stage and roughness on reach-scale spatial patterns of velocity and turbulence intensity. Geomorphology, 83(3-4), 322-345.

Lamarre, H., MacVicar, B., & Roy, A. G. (2005). Using passive integrated transponder (PIT) tags to investigate sediment transport in gravel-bed rivers. *Journal of Sedimentary Research*, *75*(4), 736-741.

Lisle, T. E. (1995). Effects of coarse woody debris and its removal on a channel affected by the 1980 eruption of Mount St. Helens, Washington. *Water Resources Research*, *31*(7), 1797-1808.

Lisle, T. E., Nelson, J. M., Pitlick, J., Madej, M. A., & Barkett, B. L. (2000). Variability of bed mobility in natural, gravel-bed channels and adjustments to sediment load at local and reach scales. *Water Resources Research*, *36*(12), 3743-3755.

Malakoff, David. "The river doctor." (2004): 937-939.

Mao, L., Uyttendaele, G. P., Iroumé, A., & Lenzi, M. A. (2008). Field based analysis of sediment entrainment in two high gradient streams located in Alpine and Andine environments. *Geomorphology*, *93*(3-4), 368-383.

Maturana, O., Tonina, D., McKean, J. A., Buffington, J. M., Luce, C. H., & Caamaño, D. (2014). Modeling the effects of pulsed versus chronic sand inputs on salmonid spawning habitat in a low-gradient gravel-bed river. *Earth Surface Processes and Landforms*, *39*(7), 877-889.

McDonald, R. R., Bennett, J. P., & Nelson, J. M. (2001, March). The USGS multi-dimensional surface water modeling system. In *Proceedings, 7th US Interagency Sedimentation Conference, Reno, Nev., p. I-161-I-167.*

McDonald, R. R., Nelson, J. M., Kinzel, P. J., & Conaway, J. S. (2005). Modeling surface-water flow and sediment mobility with the multi-dimensional surface water modeling system (MD_SWMS). *US Geological Survey Fact Sheet*, *3078*(6).

Miller, A. J., & Cluer, B. L. (1998). Modeling considerations for simulation of flow in bedrock channels. *GEOPHYSICAL MONOGRAPH-AMERICAN GEOPHYSICAL UNION*, *107*, 61-104.

Monsalve, A., Yager, E. M., Turowski, J. M., & Rickenmann, D. (2016). A probabilistic formulation of bed load transport to include spatial variability of flow and surface grain size distributions. *Water Resources Research*, *52*(5), 3579-3598.

Mueller, E. R., & Pitlick, J. (2014). Sediment supply and channel morphology in mountain river systems: 2. Single thread to braided transitions. *Journal of Geophysical Research: Earth Surface*, *119*(7), 1516-1541.

Nelson, J. M., & Smith, J. D. (1989). Evolution and stability of erodible channel beds. *River meandering*, *12*, 321-377.

Nelson, J. M., & McDonald, R. R. (1996). Mechanics and modeling of flow and bed evolution in lateral separation eddies. *Glen Canyon Environmental Studies Report*, 69.

Nelson, J. M., Bennett, J. P., & Wiele, S. M. (2003). Flow and sediment-transport modeling. *Tools in fluvial geomorphology*, *18*, 539-576.

Nelson, P. A., Dietrich, W. E., & Venditti, J. G. (2010). Bed topography and the development of forced bed surface patches. *Journal of Geophysical Research: Earth Surface*, *115*(F4).

Palmer, M. A., Bernhardt, E. S., Allan, J. D., Lake, P. S., Alexander, G., Brooks, S. & Galat, D. L. (2005). Standards for ecologically successful river restoration. *Journal of applied ecology*, *42*(2), 208-217.

Parker, G., & Klingeman, P. C. (1982). On why gravel bed streams are paved. *Water Resources Research*, *18*(5), 1409-1423.

Prancevic, J. P., & Lamb, M. P. (2015). Particle friction angles in steep mountain channels. *Journal of Geophysical Research: Earth Surface*, *120*(2), 242-259.

Rattray Jr, M., & Mitsuda, E. (1974). Theoretical analysis of conditions in a salt wedge. *Estuarine and coastal marine science*, *2*(4), 375-394.

Rickenmann, D. (1997). Sediment transport in Swiss torrents. *Earth Surface Processes and Landforms: The Journal of the British Geomorphological Group*, *22*(10), 937-951.

Roy, A.G., Buffin-Belanger, T., Lamarre, H., Kirkbride, A.D. (2004). Size, shape and dynamics of large-scale turbulent flow structures in a gravel-bed river. Journal of Fluid Mechanics 500, 1–27.

Schneider, J., Hegglin, R., Meier, S., Turowski, J. M., Nitsche, M., & Rickenmann, D. (2014). Studying sediment transport in mountain rivers by mobile and stationary RFID antennas. *River flow 2010*, 1723-1730.

Schneider, J. M., Rickenmann, D., Turowski, J. M., Bunte, K., & Kirchner, J. W. (2015).Applicability of bed load transport models for mixed-size sediments in steep streams considering macro-roughness. *Water Resources Research*, *51*(7), 5260-5283.

Schmeeckle, M. W., Nelson, J. M., & Shreve, R. L. (2007). Forces on stationary particles in near-bed turbulent flows. *Journal of Geophysical Research: Earth Surface*, *112*(F2).

Segura, C., & Pitlick, J. (2015). Coupling fluvial-hydraulic models to predict gravel transport in spatially variable flows. *Journal of Geophysical Research: Earth Surface*, *120*(5), 834-855.

Shields, A., 1936, Anwendung der Ähnlichkeitsmechanik auf die Geschiebebewegung: Berlin, Preussische Versuchanstalt für Wasserbau und Schiffbau, Mitteilungen, no. 26, 25 p.

Segura, C., & Pitlick, J. (2015). Coupling fluvial-hydraulic models to predict gravel transport in spatially variable flows. *Journal of Geophysical Research: Earth Surface*, *120*(5), 834-855.

Skidmore, P. B., Shields, F. D., Doyle, M. W., & Miller, D. E. (2001). A categorization of approaches to natural channel design. In *Wetlands Engineering & River Restoration 2001*(pp. 1-12).

Vericat, D., Batalla, R. J., & Gibbins, C. N. (2008). Sediment entrainment and depletion from patches of fine material in a gravel-bed river. *Water Resources Research*, *44*(11).

Voepel, H., Leyland, J., Hodge, R., Ahmed, S., & Sear, D. (2019). Development of a vector-based 3D grain entrainment model with application to X-ray computed tomography (XCT) scanned riverbed sediment. *Earth Surface Processes and Landforms*.

Wiberg, P. L., & Smith, J. D. (1987). Calculations of the critical shear stress for motion of uniform and heterogeneous sediments. *Water resources research*, *23*(8), 1471-1480.

Wolman, M. G. (1954). A method of sampling coarse river-bed material. *EOS, Transactions American Geophysical Union*, *35*(6), 951-956.Yager et al., 2007.

Parker G. (1990) Surface-based bedload transport relation for gravel rivers, Journal of Hydraulic Research, 28:4,417-436, DOI: 10.1080/00221689009499058

Yager, E. M., Kirchner, J. W., & Dietrich, W. E. (2007). Calculating bed load transport in steep boulder bed channels. *Water Resources Research*, *43*(7).

Yager, E. M., Dietrich, W. E., Kirchner, J. W., & McArdell, B. W. (2012). Patch dynamics and stability in steep, rough streams. *Journal of Geophysical Research: Earth Surface*, *117*(F2).

Yager, E. M., Schmeeckle, M. W., & Badoux, A. (2018). Resistance Is Not Futile: Grain Resistance
    Controls on Observed Critical Shields Stress Variations. *Journal of Geophysical Research: Earth
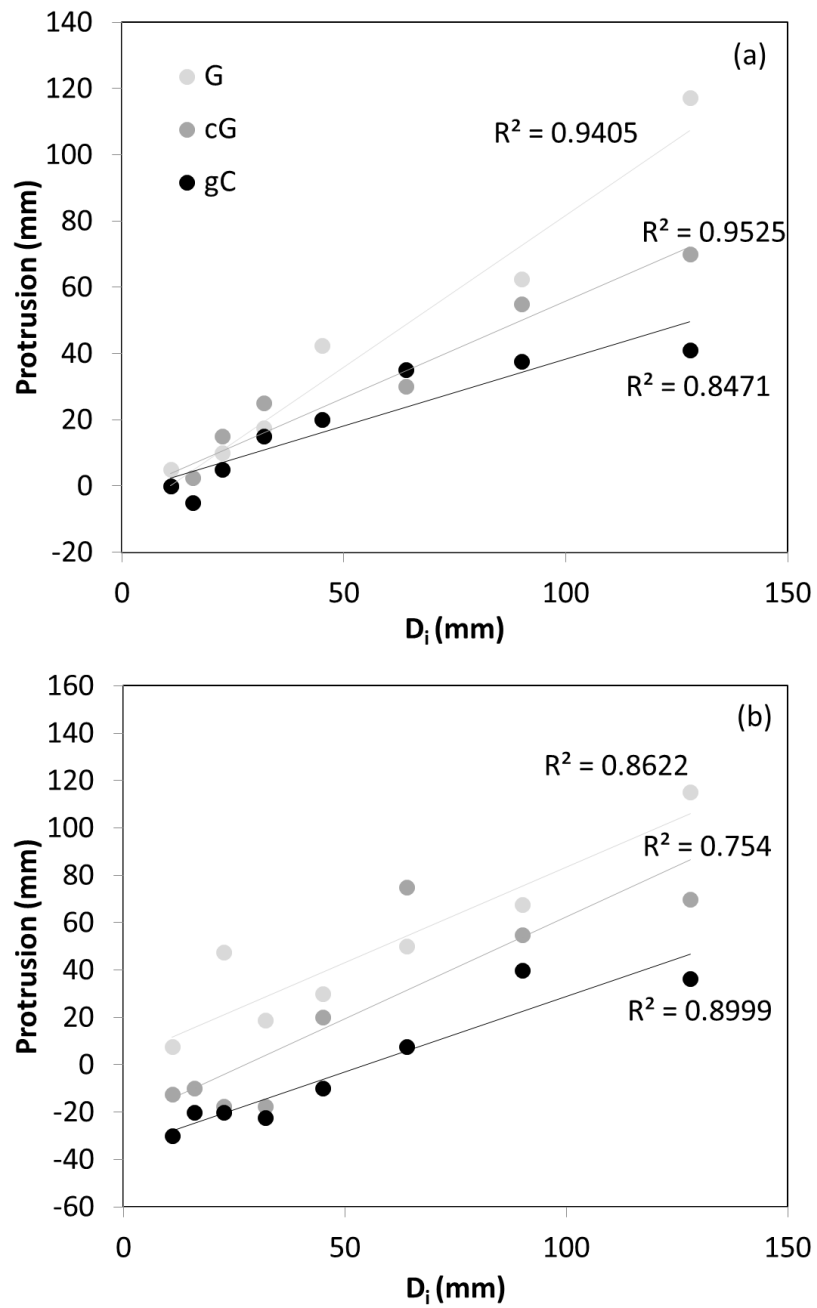   Surface*, *123*(12), 3308-3322.

Figure 3.1 Measured median protrusion for each grain size (D_i) in each patch type. For each grain, protrusions were measured (a) immediately upstream, and (b) near proximity and upstream of the grain.
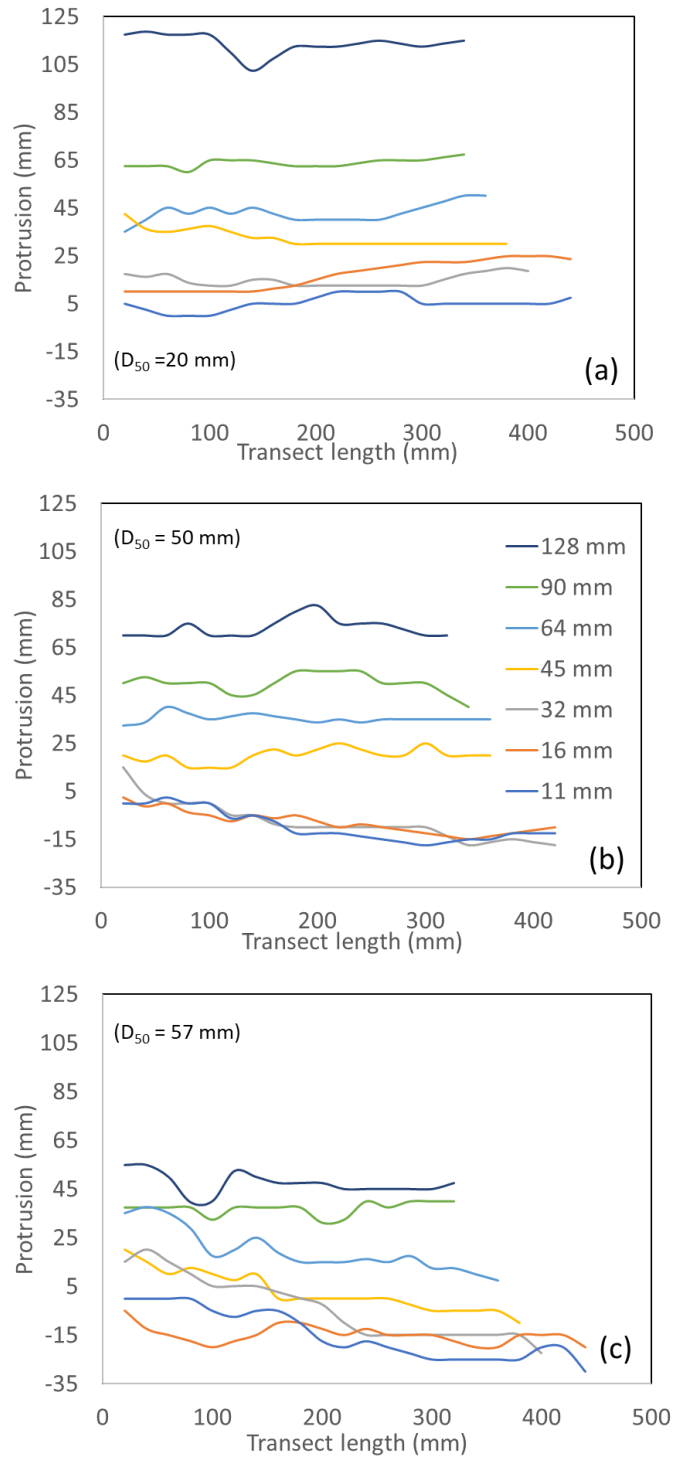
Figure 3.2 Median protrusion with increasing transect length for each grain size on (a) gravel, (b) cobble-Gravel, and (c) gravel-Cobble patches.
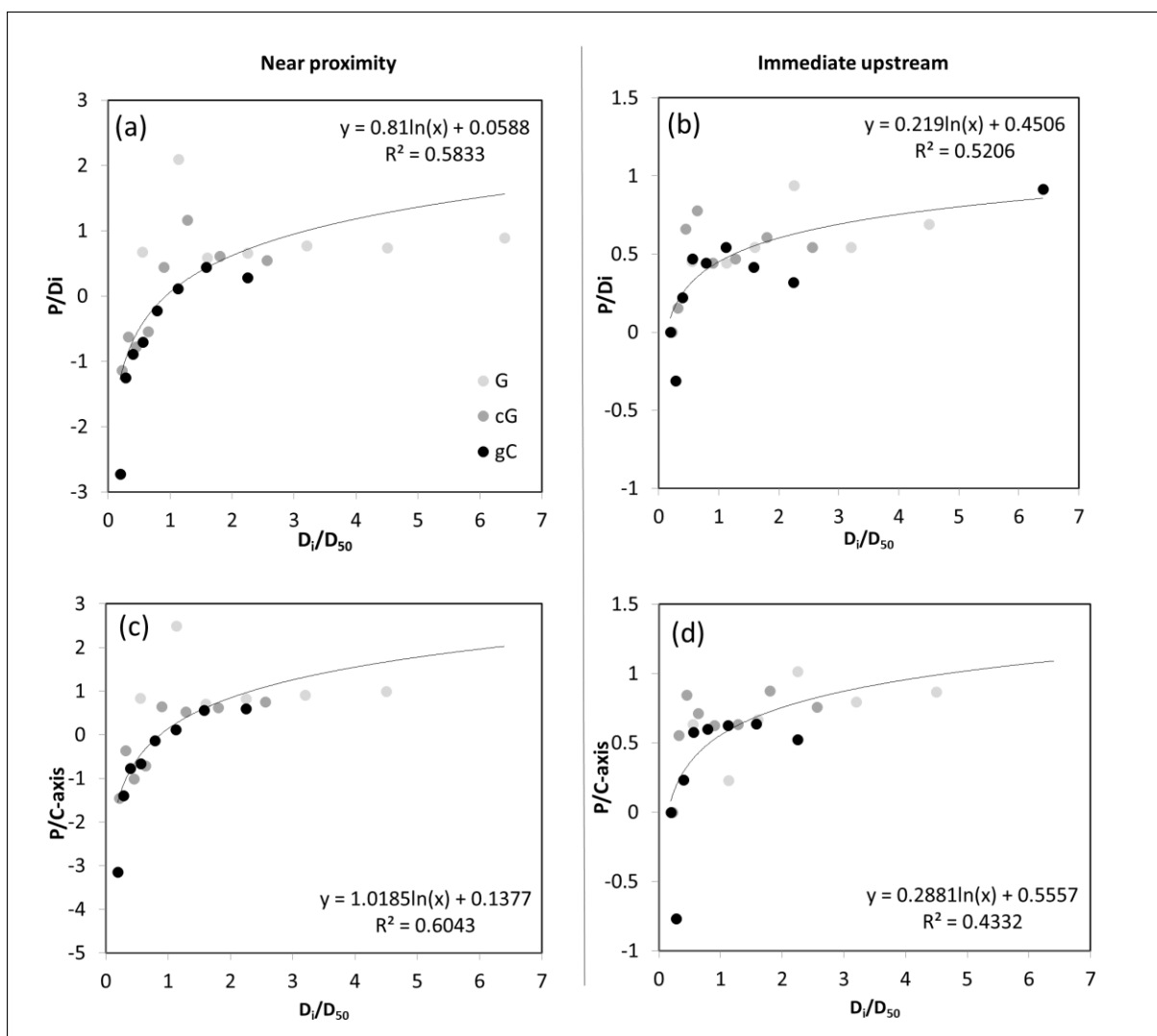
Figure 3.3 Median protrusion (P) normalized by grain size (D_i) (a and b) and grain c-axis diameters (c and d) for near-proximity (a and c) and immediate upstream (b and d) scales. Fit lines are for all patch types combined.
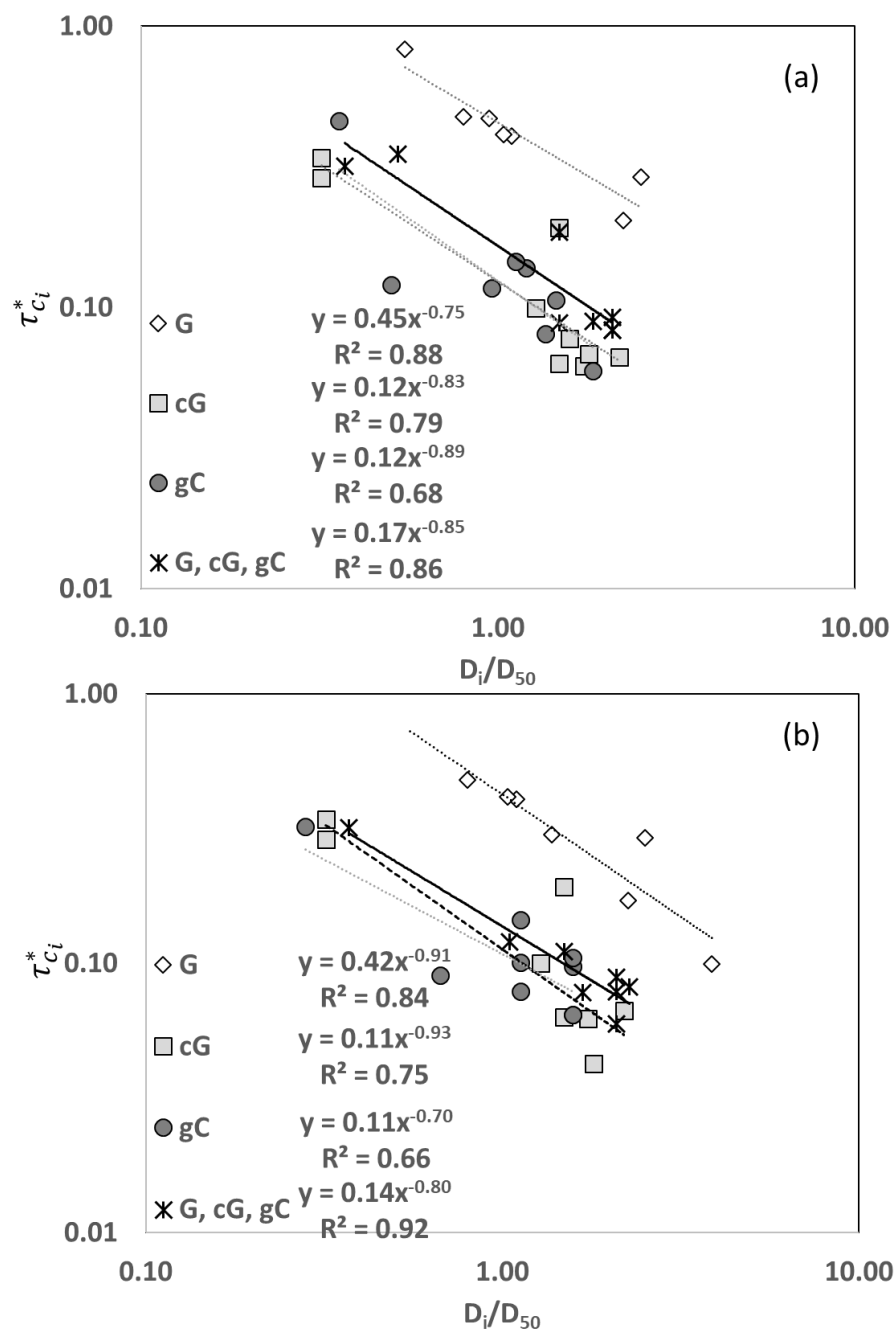
Figure 3.4 Hiding functions for each patch type and for all patch types combined. Hiding functions included mobile tracers and shear stresses (a) only on fully populated patches, and (b) for all patches with mobile tracers.
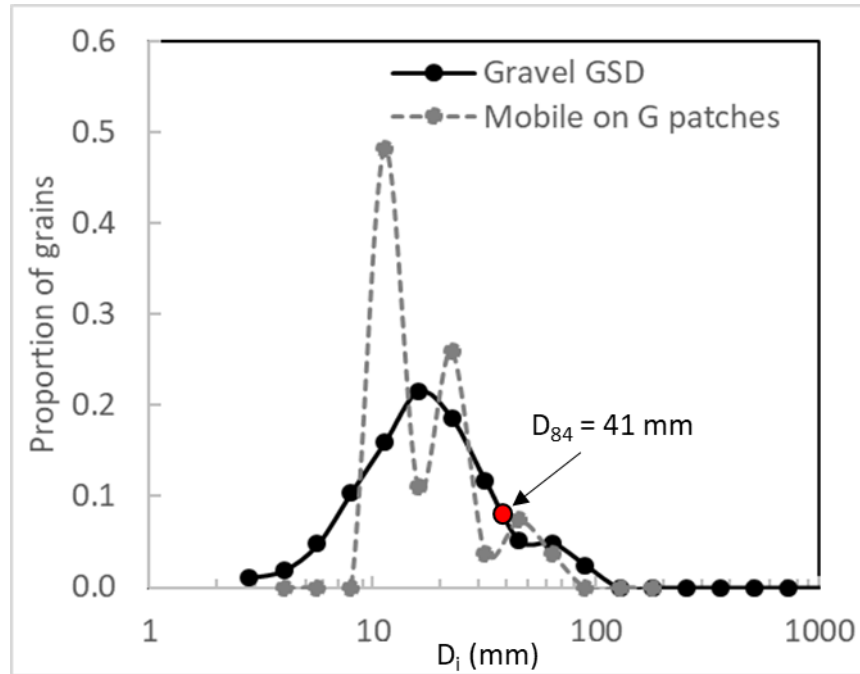
Figure 3.5 Gravel patch and mobile tracer (all events combined) grain size distributions with the D_{84} of mobile tracers on G patches denoted by the red circle.
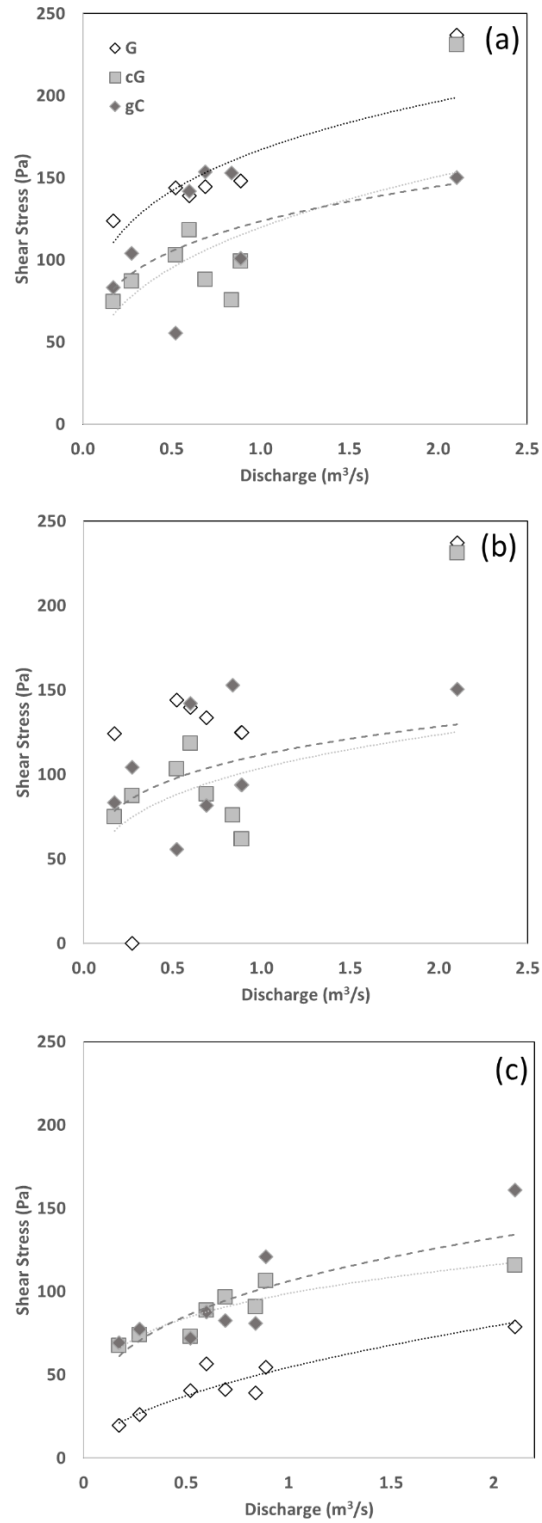
Figure 3.6 Median shear stresses for each peak discharge and each patch type on (a) only fully populated patches, (b) all patches with mobile tracers, and (c) all submerged patches.
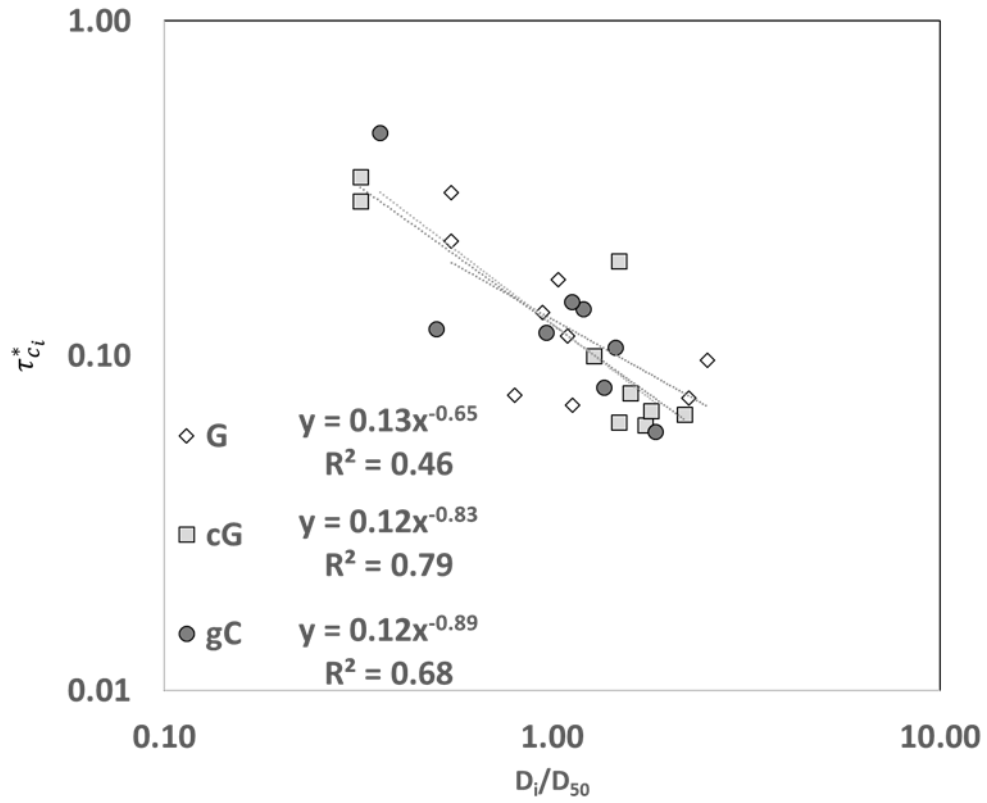
Figure 3.7 Hiding functions using median shear stresses for all submerged G patches. The hiding functions for cG and gC patch types are computed using only fully populated patches.
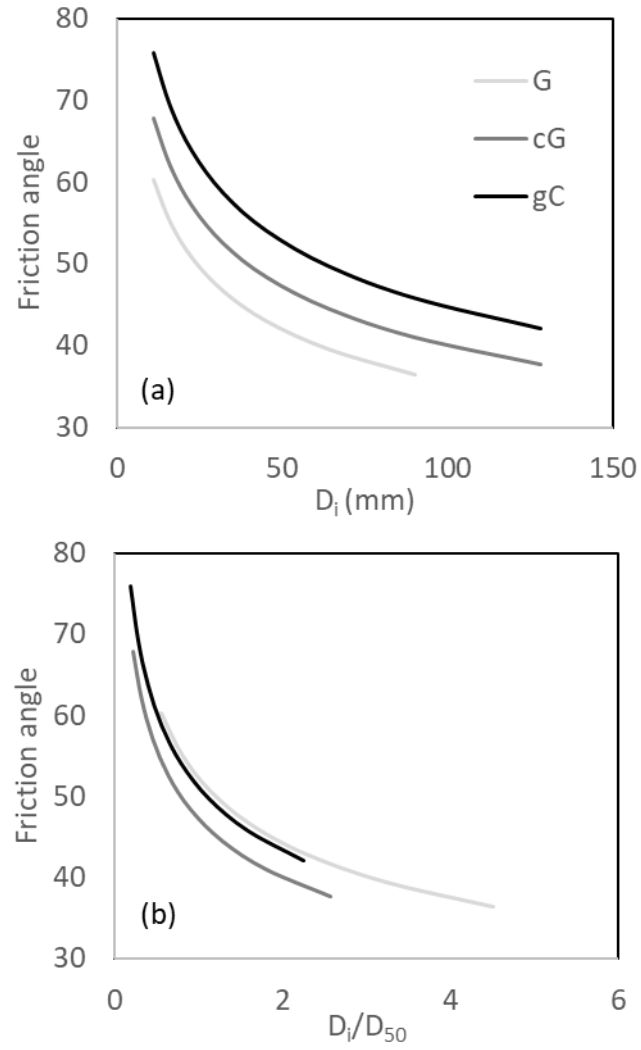
Figure 3.8 Friction angles (a) calculated with equation 4 for each grains size (D_i) and patch type combination and for (b) when grain size (D_i) is normalized by the patch D_{50}.

Table 3.1 Number of protrusion transects collected for each grain size and patch type combination.

Surface grain size (mm)	Patch type		
	G	cG	gC
11	9	11	19
16	4	17	21
22.6	5	16	28
32	4	15	27
45	4	18	37
64	11	18	44
90	11	19	50
128	4	19	31

Table 3.2 Mobile D_{84} used in hiding functions and the number of grains (n) used to calculate D_{84} for each peak discharge (Q) for each patch type.

Q (m³/s)	G		cG		gC	
	D84	n	D84	n	D84	n
0.17	16	1	16	7	16	10
0.27	23	1	87	5	64	15
0.52	22	4	64	13	38	23
0.60	21	2	110	4	90	6
0.69	27	4	16	20	64	29
0.84	11	1	74	0	90	20
0.89	78	4	90	27	90	24
0.89	45	15	90	17	90	36
2.10	50	18	74	11	64	43

Chapter 4: How grain entrainment may affect grain-dwelling organisms and stream food webs

This chapter is a discussion on potential links between grain-scale mechanics of motion and the ecological concepts pertinent to river restoration. Organisms in rivers (e.g periphyton, macroinvertebrates and crayfish) live on and in between grains. When these grains are mobilized, the organisms are removed with them resulting in community level disturbances. The scale and frequency of these disturbances vary and can have resulting impacts in local biodiversity (higher number of species). This relates specifically to this dissertation, in that chapters one through three describe grain-scale mechanics that illustrate how grain motion in rivers is determined by several factors. These factors are turbulence, the presence of boulders, and the variability of median grain size in patches and likely have corresponding effects on river ecosystems. Here were discuss: 1) the effects of disturbance on producer and macroinvertebrate communities as previously described in the literature, 2) the previously established links between bed surface entrainment and grain-dwelling organisms, and 3) how our results (from chapters one through three) of grain-scale mechanics of motion may also affect producers and macroinvertebrates.

Disturbance to grain-dwelling organisms on immobile grains has been previously studied, describing how organisms are affected by disturbances unrelated to grain motion (Paine, 1966, Ledger et al., 2008). Specifically, disturbance frequency and intensity has been shown to alter producer community structure (Paine, 1966; Death et al., 2005; Ledger et al., 2008). The intermediate disturbance hypothesis illustrates how disturbance intensity relates to biodiversity (Paine, 1966; Connell, 1978; Sousa 1979). Specifically, areas of intermediate disturbance had higher biodiversity than those with high and low disturbance regimes (Paine, 1966). Though Paine's original hypothesis was applied to the intertidal zone, the theory has since been applied to streams and rivers (e.g. Power and Stewart, 1987; Ledger et al., 2008). In the study of Ledger and others, disturbance was defined as the dewatering of a specific patch of sediment. Treatments of Ledger and others included high or low frequency disturbance regimes, in addition to a control group of an undisturbed regime with continuous flow. Patches with no disturbance and low-frequency disturbance resulted in low richness of periphyton communities. However, species richness was statistically higher under patches with high-frequency disturbance regimes (Ledger et al., 2008). Additionally, the population of the dominant algae species was lowered with the disturbance frequency. They continued to explain that disturbance was a mechanism for making niche space available for a greater number of periphyton species (Ledger et al., 2008). Diatoms out-compete algae if no disturbance exists, by

rapid reproduction and forming stable crusts over the surface of the stones. However, under disturbance, the diatom mats sloughed off and made space for algal mats to form. The high disturbance flow regimes were the most effective at minimizing diatom crusts, and nearly eliminated diatom populations in some of the treatments, where colonization occurred by opportunistic algae species. Furthermore, Ledger and others (2008) showed evidence that the layering of algal mats and diatom crusts on top of one another affected how the patches changed in the future. This suggests that the history of disturbance was an important component that defined present species community structure, an observation made previously in several other studies (Power and Stewart, 1987; Robson and Matthews, 2004; and Death and Zimmerman, 2005). In addition to these findings, disturbance of varying intensity may result in heterogeneity of periphyton structure and river environments with patchy disturbance regimes and may result in a more diverse producer community (Sousa, 1979).

The movement of grains is a form of disturbance and has been previously shown to affect macro-invertebrate communities (Robinson et al., 2004) by causing large-scale downstream drift of these species that flush macroinvertebrates from a large portion of the grains. During stable conditions, when velocities within the river are low, a minimal density of macroinvertebrates are always transported downstream (Gibbons et al., 2004), and do not constitute a disturbance. However, catastrophic drift is a disturbance of macroinvertebrates and has been loosely defined to be when 1) the rate of species transported is high, or 2) the number of species within the drift exceeds a certain high value (Brittain and Eikeland, 1988; Gibbons et al., 2007; Gomi et al., 2010). Gibbons and others found that macroinvertebrate drift coincided in a natural stream during a storm when grains For example, some species enter the flow column due to the mobilization of fine grains (Molinos and Donohie, 2009), and certain species were observed to have peaks in drift at different levels of disturbance caused by the addition of fine grains over a period of time (Gomi et al., 2010). Thus, different species may have unique thresholds of disturbance. Immediately following a disturbance of macroinvertebrates due a large portion of bed surface movement, a decline of number of species and diversity has been observed (Feeley et al., 2012). Based on our review, it appears that the long-term effects on macroinvertebrates by grain mobilization disturbances have been largely unstudied.

Mobilization of species due to turbulence

Through experiments in the flume and fields, we provide evidence that the critical Shields stress at the onset of motion due to various factors caused by near-bed velocities being fundamentally different due to turbulence without boulders, with boulders. The force fluctuations vary both temporally (e.g., during a storm event) and spatially, and are applied to grains. However, they can also apply to producers and macroinvertebrates. We observed that impulse most often corresponds to

the onset of grain motion. While grain motion can be explained by impulse, it is interesting to consider if impulses would correspond to the entrainment of macroinvertebrates and also producer species. During flow discharges that do not mobilize sediment, impulses may mobilize both producers and macroinvertebrates and could be dependent on the near-bed velocity fluctuations. Factor that could influence macroinvertebrate mobilization could be that some species may be able to adhere to sediment surfaces more effectively than others. The ability for certain species to withstand certain near-bed fluid forces may determine their habitat. For example, stone flies (whose bodies are held very near to rock surfaces) and caddisflies (that physically adhere themselves to substrate) both prefer riffle habitats, where fluctuations in near-bed velocities are heightened. Other species like black fly larvae, leeches, and worms are found in stagnant water with low near-bed velocity fluctuations. Therefore, near-bed velocities may affect species diversity by influencing which bed location to which certain producer species both adhere to and remain. Unlike the critical drag force of a grain, macroinvertebrates can change their location to areas with lower velocities to find refugia between or under grains.

Disturbance of species variation between patch types

We provided evidence in chapter 3 that patches of increasing median grain size mobilize at different critical Shields stresses, such that different shear stresses are responsible for the motion of grains within each patch type. The variability of grain movement between submerged patches during a storm event suggests that macroinvertebrates will start a heightened drift at different applied shear stresses. We also provide evidence that larger grains extend higher into the high velocity flow column and also all grains in finer patches (smaller median grain size). How might certain grains in certain patch types be more suitable for specific species based on the hiding effects present within each patch. Certain species may prefer small grains that are hidden in coarse patches, or larger grains that are more exposed to flow.

Increase in species refugia (boulders) with channel slope

Finally, our data suggests that as channel slope increases in rivers with boulders, the grains move at higher average shear stresses than at lower slopes due to a change in the flow characteristics related to the boulders. This does not mean that the mobile fraction of the bed moves less often. It does suggest that large immobile grains or wood that is larger and is present at higher densities than at lower streams. This may have an impact on the refugia, or areas that species can populate disturbed patches from, available for macroinvertebrates and producer communities. Refugia has been linked to the resiliency of communities that recover from disturbances. The implication is that perhaps

steeper streams have more areas of refugia such that disturbed areas of patches are more quickly repopulated.

Literature Cited

Brittain J. & Eikeland T.J. (1988). Invertebrate drift – a review. Hydrobiologia, 166, 77–93.

Connell, J.H. (1978). Diversity in tropical rain forests and coral reefs. Science 199:1302-1310.

Feeley, H., Davis, S., Bruen, M., Blacklocke, S., & Kelly-Quinn, M. (2012). The impact of a catastrophic storm event on benthic macroinvertebrate communities in upland headwater streams and potential implications for ecological diversity and assessement of ecological status. *Journal of Limnology*, *71*(2), 109-318.

Gibbins, C. N., Soulsby, C., Campbell, L., Scott, E., Mc-Ewan, I., & Malcolm, I. (2004). Influence of channel hydraulics and sediment mobility on stream invertebrate drift. *Hydrology: science and practice for the 21st century*, *2*, 90-98.

Gibbins, C., Vericat, D., & Batalla, R. J. (2007). When is stream invertebrate drift catastrophic? The role of hydraulics and sediment transport in initiating drift during flood events. *Freshwater Biology*, *52*(12), 2369-2384.

Gomi, T., Kobayashi, S., Negishi, J. N., & Imaizumi, F. (2010). Short-term responses of macroinvertebrate drift following experimental sediment flushing in a Japanese headwater channel. *Landscape and Ecological Engineering*, *6*(2), 257-270.

Ledger, M.E., Harris, R.M.L., Armitage, P.D. & Milner, A.M., (2008). Disturbance frequency influences patch dynamics in stream benthic algal communities. *Oecologia*, 155, 809 – 819.

Molinos, J. G., & Donohue, I. (2009). Differential contribution of concentration and exposure time to sediment dose effects on stream biota. *Journal of the North American Benthological Society*, *28*(1), 110-121.

Paine, R. T. & Levin, S. A. (1981). Intertidal landscapes: disturbance and the dynamics of pattern. *Ecological monographs, 51(2)*, 145-178.

Power, M. E., & A. J. Stewart. (1987). Disturbance and recovery of an algal assemblage following flooding in an Oklahoma stream. *American Midland Naturalist*. 333-345.

Robinson, C. T., Aebischer, S., & Uehlinger, U. (2004). Immediate and habitat-specific responses of macroinvertebrates to sequential, experimental floods. *Journal of the North American Benthological Society*, *23*(4), 853-867.

Sousa, W. P. (1979). Disturbance in marine intertidal boulder fields: the nonequilibrium maintenance of species diversity. *Ecology* 60.6: 1225-1239.